# Coulomb Excitation of Neutron-Deficient Sn Isotopes

LICENTIATE THESIS

Andreas Ekström
Department of Physics


LUND
UNIVERSITY

2008

**Coulomb Excitation of Neutron-Deficient Sn Isotopes**
Andreas Ekström

Division of Nuclear Physics
Department of Physics
Lund University
Box 118
SE-221 00 Lund
Sweden

LUNFD6(NFFR-3104)1-77(2008)

Typeset by the author using LaTeX 3.14159

# Preface

This licentiate thesis is the result of two years of work as a PhD student in the nuclear structure group at the department of Physics at Lund University. It contains the result of the analysis of three experiments carried out at the REX-ISOLDE facility at CERN. The purpose of the experiments was to extract the reduced transition probability, the so called $B(E2)$ value between the first excited $2^+$ state and $0^+$ ground state in the neutron deficient Sn isotopes, $^{106,108,110}$Sn. The experiments were only possible due to recent technological advances in the production of post-accelerated Radioactive Ion Beams with adequate intensity. The $B(E2)$ value provide information about the wave functions of the states involved in the transition, such as the collectivity of the excited state.

I have previously presented parts of the results at the following occasions:

- Svenskt Kärnfysikermöte XXV, Umeå, Sweden, November, 2005.
- IX International Conference on Nucleus Nucleus Collisions, Rio de Janeiro, Brazil, September, 2006.
- FINUSTAR 2, Aghios Nikolaos, Crete, Greece, September, 2007.
- Svenskt Kärnfysikermöte XXVII, Gothenburg, Sweden, November, 2007.

Lund, December 5, 2007
*Andreas Ekström*

# Contents

# List of Included Papers

PAPER I: **Sub-Barrier Coulomb Excitation of $^{110}$Sn and Its Implications for the $^{100}$Sn Shell Closure**
J. Cederkäll, A. Ekström *et al.*
*Phys. Rev. Lett.* **98** *172501 (2007).*

PAPER II: **Sub-Barrier Coulomb Excitation of $^{106,108,110}$Sn**
A. Ekström *et al.*
*AIP Conference Proceedings, FINUSTAR2 2007 - Frontiers in Nuclear Structure, Astrophysics and Reactions*

# List of Figures

# List of Tables

# Chapter 1

# Introduction

This work is focused on the experimental measurements of the transition probability between the first excited $2^+$ state and the $0^+$ ground state, the so-called $B(E2)$ value, in the $\beta$-unstable neutron-deficient $^{106,108,110}$Sn isotopes. The $B(E2)$ value gives information on the degree of quadrupole collectivity versus the single-particle nature of the excited state. The $B(E2)$ values for the heavier even-mass Sn isotopes and a theoretical prediction are displayed in Fig. 1.1. The experimentally observed shift at $^{114}$Sn towards a larger $B(E2)$ value

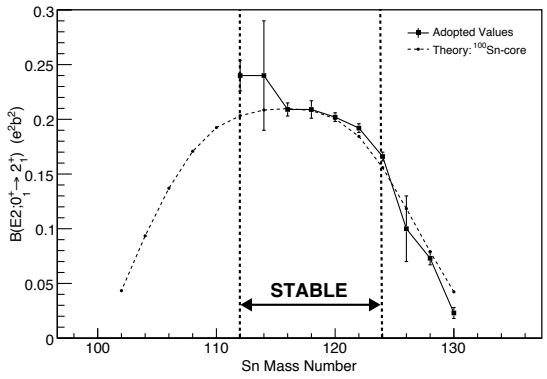


Figure 1.1: $B(E2)$ *values for the even-mass Sn isotopes with* $A > 110$*. The theoretical prediction is a shell-model calculation [1] with an effective interaction based on the CD-Bonn nucleon-nucleon interaction. For* $A < 116$ *a shift towards higher* $B(E2)$ *values is observed.*

deviates from the theoretical prediction. It is of great interest in nuclear structure physics to investigate the $B(E2)$ values in the lighter Sn isotopes. This has been made possible through the recent advent of post-accelerated radioactive ion beams.

Atomic nuclei with proton and neutron numbers 2,8,20,28,50,82 and 126 are energetically more bound than their neighbors on the nuclear chart. These so-called magic numbers are the corner stones of modern nuclear theory. They indicate that the atomic nucleus has a shell structure conceptually similar to the one seen in the electron structure of the atom. Due to this, the Sn isotopes, which have 50 protons, comprise the the longest isotopic chain in na-

ture. This makes them attractive for a systematic investigation. The structural changes of the first excited state are mapped by measuring the $B(E2)$ value towards the doubly-magic $^{100}$Sn nucleus. Furthermore, this will provide information on the strength of the shell-closure at $^{100}$Sn. Moreover, when this is compared with the theoretical predictions, it can aid in providing insights on the underlying nucleon-nucleon interaction.

The thesis is divided into 6 chapters. The next chapter (Ch. 2) gives an introduction to the theoretical concepts. Chapter 3 explains the experimental method. Chapter 4 gives the details regarding the analysis of the experimental data and the experimental results are summarized in Ch. 5. The present status of the theoretical calculations is given in Ch. 6.

# Chapter 2

# Theoretical Aspects

The main theoretical ideas on which this thesis rests are summarized in this chapter. The fundamental theoretical problems connected with present-day nucleon-nucleon interactions in finite nuclei are discussed. The last section briefly treats the well-established theory of Coulomb excitation.

## 2.1 The Nucleon-Nucleon Interaction

The atomic nucleus is a quantal many-body system consisting of $N$ neutrons and $Z$ protons which in total amounts to $A = N + Z$ nucleons. A nucleon in turn is built of three quarks that interact via the strong force mediated by gluons. Quantum chromodynamics (QCD) is the theoretical framework of how quarks and gluons interact with each other and themselves. It is with presently available techniques not possible to derive the free nucleon-nucleon interaction, $V_{\mathcal{NN}}$, from fundamental QCD principles. However, progress has been made recently within the lattice-QCD approach [2].

The interaction between two nucleons in free space is not the same as their interaction in the nuclear medium. The nuclear medium can be finite (e.g. atomic nuclei) or infinite (e.g. neutron stars). The interaction of interest here is the one within the atomic nucleus. Modern theories describing the nucleon-nucleon interaction make use of the effective field theory (EFT) concept [3]. In this framework only the low-energy degrees of freedom are taken into account. Low is defined with respect to the chiral symmetry breaking scale $\Lambda \approx 1$ GeV. The only participating particles in this model are the nucleons and the lightest meson, the pion. Steven Weinberg showed [4] that it is possible to construct a systematic expansion, a so called chiral perturbation, of $V_{\mathcal{NN}}$ in terms of $(Q/\Lambda)^{\nu}$, where $Q$ is the pion momentum transfer and $\nu = 1, 2, 3, \ldots$. The underlying nucleon-nucleon Lagrangian incorporates all known symmetries of the QCD Lagrangian, in particular spontaneously broken chiral symmetry [5], which is crucial for an accurate description of nuclei. For the chiral expansion to converge, $Q$ must be smaller than $\Lambda$. The number of terms in the expansion to order $\nu$ is finite. Presently, $\nu = 4$ is the highest order chiral EFT nucleon-nucleon Lagrangian constructed, leading to the N3LO nucleon-nucleon interaction [6, 7]. Three-body interactions are present at order $\nu \geq 4$, however, not included in the present N3LO interaction. The N3LO interaction contains $N_{par} = 29$ parameters [6]. They are fitted to reproduce experimental scattering data. At $\nu = 4$ the $\chi^2/N_{par}$ of the fit to neutron-proton scattering data is 1.1. The $\chi^2/N_{par}$ for $NNLO$

($\nu = 3$) and $NLO$ ($\nu = 2$) are 10.1 and 36.2 [8], respectively, indicating a rapid convergence with increasing $\nu$.

There exist other types of free nucleon-nucleon interactions with just as good parameter fits to the experimental data. For instance one boson exchange potentials (OBE) [9], where the latest one is called the CD-Bonn interaction [10]. Reference [11] and references therein give an exposé of various nucleon-nucleon interactions. However, there are two arguments that make chiral EFT models appealing. First of all, it stems from underlying QCD making it the most fundamental approach as of today, and secondly, many-body interactions come out systematically with increasing chiral order $\nu$.

The experimental input to the parameter fit of the EFT nucleon Lagrangian or any phenomenological Lagrangian come from phase shifts $\delta$ [1] in $np$ and $pp$ scattering experiments. The phase shifts are related to the underlying scattering interaction $V$ through the $\mathbf{R}$-matrix [12], which in the center of mass system can be expressed with the integral equation [13]

$$R(q', q, E) = V(q', q) + \mathcal{P} \int_0^\infty k^2 dk V(q', k) \frac{1}{E - k^2/M} R(k, q; E) \tag{2.1}$$

The $\mathbf{R}-$matrix also depends on the total angular momentum, spin, and isospin. The energy of the interacting nucleons of mass $M$ is denoted by $E$ and the relative momenta is given by $q, q', k$. In particular, $k$ is the intermediate momenta during the interaction process. The experimental phase shifts are related to the diagonal $\mathbf{R}-$matrix elements when $q' = q = q_0$

$$R(q_0, q_0) = -\frac{\tan \delta}{m q_0}, \quad E = \frac{q_0^2}{M} \tag{2.2}$$

The non-diagonal $\mathbf{R}-$matrix elements are not constrained by experimental data. All nucleon-nucleon potentials will produce the same diagonal $\mathbf{R}$-matrix elements. The non-diagonal part is model dependent. Currently, the world scattering data base on $np$ and $pp$ scattering data contain phase shifts up to and including the angular momentum $\ell = 6$ partial wave below $300$ Mev in the laboratory frame of reference. The typical shape of the nucleon-nucleon interaction $V_{\mathcal{NN}}$ as a function of inter-nucleon separation is plotted in fig. 2.1. Due to the repulsive core of $V_{\mathcal{NN}}$ the interaction matrix elements become very large or even infinite. This poses several mathematical problems.

## 2.2 Effective Interactions

It is impossible to solve the many-body Schrödinger equation analytically. One must resort to perturbation theory. However, due to the large interaction matrix elements, a perturbative scheme is not applicable without some mathematical treatment. A second issue to resolve is the large dimensionality of the interaction matrix of a nucleus with $100$ nucleons. The present-day computational limit is at a dimension of $\sim 10^9$ basis states. The strongly repulsive core of the nucleon-nucleon interaction can be renormalized using $\mathbf{G}$-matrix theory (see Sec. 2.2.2). The large space is truncated and the effects of the excluded space are included approximatively using many-body perturbation theory (see next section).

[1] $\delta > 0$ attractive potential, $\delta < 0$ repulsive potential

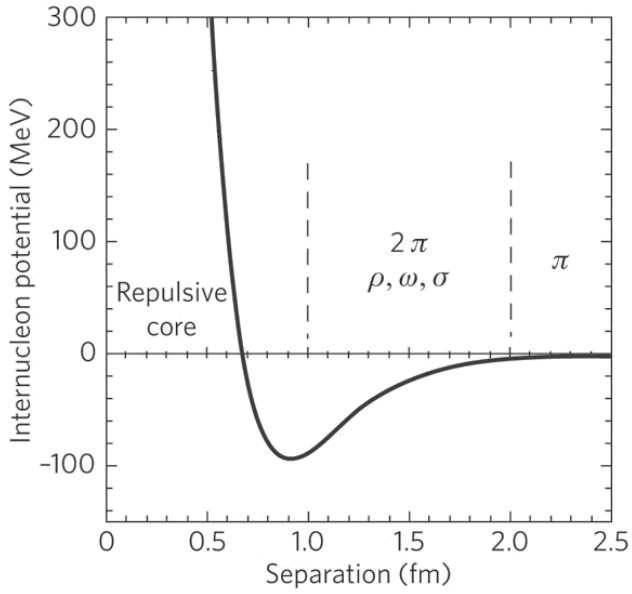


Figure 2.1: *The nucleon-nucleon interaction in the* $^1S_0$ *channel as a function of the inter-nucleon distance in fm. Below 1 fm the interaction becomes strongly repulsive. The attractive long range part of the nuclear force is mediated by the lightest meson* $\pi$*, while, in OBE models, heavier mesons are responsible for the short range and more strongly attractive parts. In EFT models only* $\pi$ *enters the equation.*

### 2.2.1 Many-Body Perturbation Theory

The full Schrödinger equation of $A$ interacting nucleons is given in Eq. 2.3. The energy $E$ is obtained by acting on the system $|\Psi\rangle$ with the Hamiltonian $H$.

$$H|\Psi\rangle = E|\Psi\rangle \tag{2.3}$$

The Hamiltonian can be divided into two parts

$$H = H_0 + V = \left\{\sum_i^A (t_i + u_i)\right\} + \left\{\sum_{i<j}^A v_{ij} - \sum_i^A u_i\right\} \tag{2.4}$$

where $t_i$ is the kinetic energy operator of nucleon $i$ and $u_i$ is a one-body potential for nucleon $i$. The interaction between nucleon $i$ and $j$ is given by $v_{ij}$, the nucleon-nucleon interaction. The second term in Eq. 2.4 is called the residual interaction and will be small if $v_{ij}$ is finite and approximately the same size as $u_i$. It will be shown in the next section how the nucleon-nucleon interaction $V_{\mathcal{NN}}$ is renormalized using **G**-matrix theory in order to make it suitable for the perturbative treatment described above. For now the residual interaction is treated as small enough to be considered as a perturbation to $H_0$.

For the harmonic oscillator potential, the one-body Schrödinger equations

$$(t_i + u_i)|\phi_\nu\rangle = e_\nu|\phi_\nu\rangle \tag{2.5}$$

are possible to solve analytically. A state of the unperturbed $A$-particle system with orbits $\alpha$ to $\eta$ filled can be written in Slater determinant form, which in the second quantization formalism reads

$$|\Phi_i\rangle = \left( \prod_{\nu=\alpha}^{\eta} a_\nu^\dagger \right) |\rangle \tag{2.6}$$

The total energy of the (non-interacting) system in state $i$ is obtained from

$$H_0|\Phi_i\rangle = \epsilon_i|\Phi_i\rangle \tag{2.7}$$

where

$$\epsilon_i = \sum_{\nu=\alpha}^{\eta} e_\nu \tag{2.8}$$

The unperturbed (or uncorrelated) states form a complete set, and the real nuclear wave function $|\Psi\rangle$ can be expressed as

$$|\Psi\rangle = \sum_i a_i|\Phi_i\rangle \tag{2.9}$$

where the expansion coefficients, $a_i$, are given by

$$a_j = \frac{\langle\Phi_j|V|\Psi\rangle}{E - \epsilon_j} \tag{2.10}$$

The expansion coefficient are obtained using the original Schrödinger equation 2.3 and the orthonormality of the unperturbed states $|\Phi_i\rangle$. The Hilbert space spanned by $|\Phi_i\rangle$ is infinite. The size of the space for which the residual interaction should be diagonalized, is now truncated and called the model space, or valence space, $P$. The excluded space, the complement of $P$, is called $Q$. The two spaces can be defined through the projection operators

$$P = \sum_{i=1}^{D} |\Phi_i\rangle\langle\Phi_i| \tag{2.11}$$

and

$$Q = \sum_{i=D+1}^{\infty} |\Phi_i\rangle\langle\Phi_i| \tag{2.12}$$

where the dimension of $P$ is $D$. In order to do realistic calculations in the model space, the interaction operating in $P$ must approximately take into account the effects of the excluded $Q$ space. The true wave function $|\Psi\rangle$ can be split up into two parts

$$|\Psi\rangle = \sum_{i=1}^{D} a_i|\Phi_i\rangle + \sum_{i=D+1}^{\infty} a_i|\Phi_i\rangle \equiv |\Psi_D\rangle + \sum_{i=D+1}^{\infty} \frac{|\Phi_i\rangle\langle\Phi_i|V|\Psi\rangle}{E - \epsilon_i} \tag{2.13}$$

where the part of $|\Psi\rangle$ in the $P-$space is defined as $|\Psi_D\rangle$. Equation 2.13 can be written on operator form

$$|\Psi\rangle = |\Psi_D\rangle + \frac{Q}{E - H_0} V|\Psi\rangle \tag{2.14}$$

where $|\Psi_D\rangle = P|\Psi\rangle$.

Introduce the wave operator (sometimes called the model operator) $\Omega$, through

$$|\Psi\rangle = \Omega|\Psi_D\rangle \tag{2.15}$$

The wave operator transforms the model space states back into the corresponding exact states, which is a non-trivial statement [14]. Write Eq. 2.14 in terms of the wave operator

$$\Omega(E) = 1 + \frac{Q}{E - H_0} V\Omega(E) \tag{2.16}$$

Assume that the wave operator has an inverse $\Omega^{-1}$ [14], and rewrite the full Schrödinger equation, Eq. 2.3 as

$$\Omega^{-1}H\Omega\Omega^{-1}|\Psi\rangle = E\Omega^{-1}|\Psi\rangle \Rightarrow \mathcal{H}|\Psi_D\rangle = E|\Psi_D\rangle \tag{2.17}$$

where $\mathcal{H} = \Omega^{-1}H\Omega$ is the transformed Hamiltonian. The transformation is a similarity transformation, which does not change the eigenvalues. The projection operator $(P + Q)$ acts as the identity operator in the full Hilbert space of Slater determinants. The transformed Hamiltonian can be written as

$$\mathcal{H} = P\mathcal{H}P + P\mathcal{H}Q + Q\mathcal{H}P + Q\mathcal{H}Q \tag{2.18}$$

Inserting this back into Eq. 2.17and using the projection operator properties of $Q$ and $P$ gives

$$\begin{aligned} [P\mathcal{H}P + P\mathcal{H}Q + Q\mathcal{H}P + Q\mathcal{H}Q]P|\Psi\rangle &= EP|\Psi\rangle \\ [P\mathcal{H}P + Q\mathcal{H}P]P|\Psi\rangle &= EP|\Psi\rangle \\ Q[P\mathcal{H}P + Q\mathcal{H}P]P|\Psi\rangle &= EQP|\Psi\rangle \\ Q[Q\mathcal{H}P]P|\Psi\rangle &= 0 \\ Q\mathcal{H}P &= 0 \end{aligned} \tag{2.19}$$

This so called decoupling relation states that the projected wave function $P|\Psi\rangle = |\Psi_D\rangle$ is a pure model space wave function. This implies that an effective model space Hamiltonian can be defined

$$H_{\text{eff}} = P\mathcal{H}P = P\Omega^{-1}H\Omega P \tag{2.20}$$

Following [15] the effective interaction can be defined as $V_{\text{eff}}(E) = V\Omega(E)$, which with Eq. 2.16 gives

$$V_{\text{eff}} = V + V\frac{Q}{E - H_0}V + V\frac{Q}{E - H_0}V\frac{Q}{E - H_0}V + \dots \tag{2.21}$$

This operator equation contains the energy $E$ of the full problem on the right hand side[2]. It can be shown [14] that Eq. 2.21 can be transformed into terms containing only the unperturbed valence energy of the nucleons, $E_v$, and an unperturbed model space Hamiltonian with the core energy removed, $H_v = H_0 - E_c$. In other words, the total energy of the system is given by

$$E = E_c + \Delta E_c + E_v + \Delta E_{cv} \tag{2.22}$$

[2]The expansion is said to be of Brillouin-Wigner type.

where $E_c$ is the energy of the unperturbed core[3], $E_c + \Delta E_c$ is the true energy of the core, $E_v$ is the unperturbed valence nucleon energy, and $\Delta E_{cv}$ is the remainder. If the energy $\Delta E_c$ and $\Delta E_{cv}$ is removed in Eq. 2.21, the denominators contain only unperturbed energies

$$V_{\text{eff}} = V + V\frac{Q}{E_v - H_v}V + V\frac{Q}{E_v - H_v}V\frac{Q}{E_v - H_v}V + \dots \tag{2.23}$$

The effective interaction series expansion is said to be given in Rayleigh-Schrödinger form. An introduction to effective operators in finite nuclei is given in Ref. [15]. Each term in Eq. 2.23 will produce a series of interaction diagrams. The type of diagram is determined by the exact form of the propagator. An introduction to such diagrams is given in Ref. [16] p. 333.

There are many technical details not mentioned here. For a full account of the theory of nuclear effective interactions, see Ref. [14] and references therein.

### 2.2.2 The G-matrix

Two-body matrix elements of the nucleon-nucleon interaction diverge if uncorrelated two-body wave functions are used. Within **G**−matrix theory, the nucleon-nucleon correlation is taken into account. In other words, the correlation effects that the interaction introduce must be incorporated into the $A$-particle wave function, see Ref. [17] Sec.III.2.

The **G**-matrix is the solution of the Bethe-Salpeter equation [14], which on operator form is given by

$$G(\omega) = V + V\frac{\mathcal{Q}_F}{\omega - H_0}G(\omega) \tag{2.24}$$

The states in a nucleus below the Fermi surface, $\varepsilon_F$, can only scatter to states above, therefore the Pauli operator $\mathcal{Q}_F$ is included. This operator is equal to zero when summing over states below $\varepsilon_F$ otherwise equal to one. A simplified and very quantitative way of seeing how the **G**-matrix handles the mathematical difficulty of the infinitely strong nucleon-nucleon repulsion at short distances is to formally solve Eq. 2.24, and let the residual interaction $V$ go to infinity.

$$G = V + V\frac{\mathcal{Q}_F}{\omega - H_0}G \Rightarrow G = \frac{V}{1 - V\mathcal{Q}_F/(\omega - H_0)} \rightarrow 1 \;\text{ as }\; V \rightarrow \infty \tag{2.25}$$

In Ref. [17] the Bethe-Salpeter equation is treated extensively. In Eq 2.25, $\omega$ is the so-called starting energy[4]. The energy $\omega$ reflects how the interacting nucleons depend on the rest of the system, and $H_0$ is the unperturbed Hamiltonian. A detailed description of how to numerically solve the **G**− matrix in finite nuclei can be found in Ref. [14].

A very intuitive approach to understand the idea behind the **G**−matrix is given in terms of the separation method of [18]. The repulsive part of the nucleon-nucleon interaction is balanced by its attractive part since the deuteron is bound. The nucleon-nucleon potential in Fig. 2.1 can be divided into two parts, a short-range part $V_S$ and the long range part $V_L$. The

[3] Energy of the core nucleon system if it was described by the unperturbed Hamiltonian $H_0$

[4] The resulting **G**-matrix is relatively independent on the starting energy [14] p. 192

distance at which $V_S$ ends and $V_L$ starts is called the separation distance (or healing distance) $d$. The distance $d$ is chosen such that the attractive part in $V_S$ balances the repulsive core. The **G**-matrix is then to a good approximation given by

$$\mathbf{G} \sim V_L(r) \tag{2.26}$$

The separation distance is typically about 1 fm [14]. The **G**-matrix is solved for a pure hard-core potential in infinite nuclear matter in Ref. [19].

The perturbation expansion given in Eq. 2.23 for an effective interaction is only convergent for small $V$. A suitable choice of effective interaction is therefore the **G**-matrix.

$$V_{\text{eff}} = G + G\frac{Q}{E_v - H_v}G + G\frac{Q}{E_v - H_v}G\frac{Q}{E_v - H_v}G + \dots \tag{2.27}$$

Effective matrix elements obtained with the program codes developed by Hjorth-Jensen [14] are presented in Appendix A.

### 2.2.3 Effective Charge

The model space wave function $|\Psi_D\rangle$ is a projection of the true wave function $|\Psi\rangle$. The expectation value $\langle\Psi_D|\mathcal{O}|\Psi_D\rangle$ of an operator $\mathcal{O}$ can not be expected to give the true physical result. This is because information is lost in the projection onto the model space. Just as an effective interaction operates in the model space, a general effective operator can be defined as

$$\langle\Psi_D^a|\mathcal{O}_{\text{eff}}|\Psi_D^b\rangle = \frac{\langle\Psi^a|\mathcal{O}|\Psi^b\rangle}{\sqrt{\langle\Psi^a|\Psi^a\rangle\langle\Psi^b|\Psi^b\rangle}} \tag{2.28}$$

The normalization of the true wave functions have not been mentioned previously. The denominator in Eq. 2.28 takes into account that the true wave functions are not normalized to unity[5].

The effective charge $e_{\text{eff}}$ is introduced in order to account for the effects of the $Q$ space on the transition excluded in the shell-model space $P$. With the electric quadrupole operator $E2$ used in the following, the effective charge can be written

$$e_{\text{eff}}^{E2} = e\left(\frac{1}{2} - t_z\right) + e_{pol}^{E2} \tag{2.29}$$

The effective charge defined in Eq. 2.29 is given in isospin formalism, where $t_z = 1/2$ gives the neutron effective charge and $t_z = -1/2$ gives the proton effective charge. The difference between the bare charge, $e$, and the effective charge $e_{\text{eff}}$ is called the polarization charge $e_{pol}$.

The same value of the effective charge can be used for similar transitions for nuclei in the same model space. The concept can be given a physical meaning. This important point should be repeated. The value of the effective charge is dependent on the size of the model space and the type of effective interaction that operates within this space. The effective

[5]The true wave functions $|\Psi\rangle$ are normalized according to $\langle\Psi|\Psi_D\rangle = \langle\Psi_D|\Psi_D\rangle = 1$. The $|\Psi^2|$ deviation from unity can be evaluated order by order if Eq. 2.13 is iterated

charge may depend weakly on the orbit considered [20], but the state independent approach is accepted in many applications [16]. A single value on the effective charge is enough to reproduce the various transition rates within one shell well enough. This is a property which has made the effective charge concept so valuable [16].

## 2.3 The Nuclear-Shell Model

The average distance between two nucleons in finite nuclei is about 1.8 fm. It is crucial that the healing distance is shorter than the average nucleon-nucleon separation. This tells us that the residual interaction is weak, or in other words that nuclear excitations rarely are due to nuclear collisions [17].

The eigenfunctions $\Phi$ of the pure shell-model Hamiltonian $H_0$ are called orbits. The orbits of the one-body Hamiltonian including the nuclear spin-orbit coupling $\ell \cdot s$ as introduced by [21, 22] has enjoyed great success in describing the experimentally observed shell-structure and so-called magic numbers. The nuclear shell-model is thoroughly reviewed in Ref. [17].

Neutrons and protons are classified in terms of the $n, \ell, j$ (shell quantum number, orbital angular momentum, and total angular momentum) using the notation $n\ell_j$ together with spectroscopic notation for $\ell$, i.e. $s, p, d, f, \ldots$. In Fig. 2.2 the effect of including the $\ell \cdot s$ term in a Woods-Saxon type potential is clearly seen.

The shell gaps at the magic numbers provide for a natural truncation of the full shell-model space. The effective interaction is tailored for each type of model space. The results from diagonalizing the effective Hamiltonian in this space is generally in good agreement with experiment. The calculations in the Sn isotopes presented in Ch. 6 was carried out in a valence space consisting of the neutron orbits $1g_{7/2}2d_{5/2}2d_{3/2}3s_{1/2}1h_{11/2}$ with $^{100}$Sn considered as an inert core.

The fact that the true nuclear Hamiltonian $H$ can be divided into two parts, $H_0$ and $V$, as defined in Eq. 2.4, is the basic foundation of the nuclear shell-model. The introduction of a central one-body field $u_i$ in $H$ is not without problems. By placing the $A$ nucleons in a central potential fixed in space, a set of eigenvalues purely related to center of mass motion is introduced. The eigenvalues of interest originate from the relative motion between nucleons. There are methods of dealing with these so-called spurious states [17].

## 2.4 Coulomb Excitation

Coulomb excitation is the physical process in which a target/projectile nucleus is excited by the electromagnetic field of a projectile/target nucleus. The theoretical framework [23, 24] is well established [24]. In our case we have projectile energies below the Coulomb barrier. The case of higher projectile energies is described in Ref. [25]. The primary advantage in using sub-barrier Coulomb excitation is the inherent exclusion of any strong force component in the excitation process. The maximum projectile energy which does not penetrate the

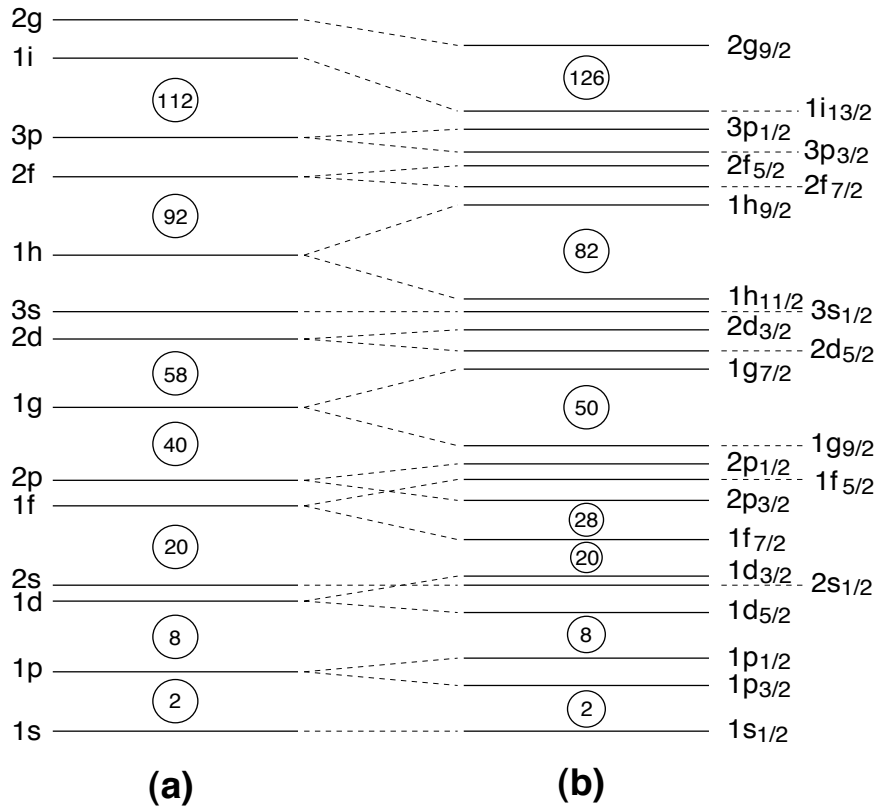


Figure 2.2: *The nuclear shell-model orbits based on a Woods-Saxon type potential. In (a) the resulting energy levels without $\ell \cdot s$ coupling. In (b) the resulting energy levels including the $\ell \cdot s$ coupling. Note that the experimentally known magic numbers are reproduced nicely.*

Coulomb barrier is given by [26]

$$E_{max} = 1.44 \frac{A_p + A_t}{A_t} \cdot \frac{Z_p \cdot Z_t}{1.25(A_p^{1/3} + A_t^{1/3}) + 5} \text{ MeV} \tag{2.30}$$

In Equation 2.30 $t$ denotes target and $p$ denotes projectile. Staying below $E_{max}$ corresponds to a minimum separation between the nuclear surfaces of about $5$ fm. In the following, projectile excitation is assumed, and the formulas are given in the center of mass frame of reference. Furthermore, it is intuitively easier to describe Coulomb excitation using a semi-classical approach. This approach is valid for many cases, which will be shown below, and more importantly for the experiments discussed in this licentiate thesis.

### 2.4.1 Semi-Classical Theory

The difference between a full quantum mechanical treatment and a semi-classical one, lies primarily in how the impinging particle trajectory is described. In the semi-classical treatment, the relative motion is described classically, while the electromagnetic interaction leading to excitation of a nuclear state is described in first-order perturbation theory. The dimen-

sionless Sommerfeld parameter[6], $\eta$, gives a measure on the applicability of classical trajectories.

$$\eta = \frac{Z_1 Z_2 e^2}{\hbar v} \tag{2.31}$$

where $Z_1$ and $Z_2$ are the charge numbers of the projectile and target, respectively, and $v$ is their relative velocity. For the particle to follow a classical trajectory, $\eta >> 1$ must hold, which is the case for the three experiments discussed in this thesis. The differential cross section for nuclear excitation from state $|i\rangle$ to state $|f\rangle$ is given by

$$\left(\frac{d\sigma}{d\Omega}\right)_{i\to f} = \frac{d\sigma}{d\Omega}_R \cdot P_{i\to f} \tag{2.32}$$

where $(d\sigma/d\Omega)_R$ is the Rutherford differential cross section[7] for scattering into the solid angle $d\Omega$ , and $P_{i\to f}$ is the probability for nuclear excitation. For the classical picture to still hold, the energy transfer $\Delta E$ must be smaller than the center of mass energy $E = \frac{1}{2} m_o v^2$. The energy difference $\Delta E$, is equal to the excitation energy of the state $|f\rangle$.

A quantity that characterizes the excitation probability is the adiabaticity parameter $\xi$

$$\xi_{i\to f} = \frac{\Delta E \tau}{\hbar} \tag{2.33}$$

where $\tau$ is the collision time. The collision time can be estimated using half the distance of closest approach together with the known relative velocity.

$$\tau = \frac{a}{v} \tag{2.34}$$

$\Delta E/E$, can now be written

$$\frac{\Delta E}{E} = \frac{2\xi_{i\to f}}{\eta} \tag{2.35}$$

For the cases presented here, sub-barrier Coulomb excitation can be treated within the semi-classical picture. The semi-classical expressions of the excitation process does not include how the motion of the particles is altered due to the excitation. This can be approximately included by a symmetrized expression for $a$ and $\xi$ in the following way [23]

$$\tilde{\xi} = \frac{Z_1 Z_2 e^2}{\hbar} \left(\frac{1}{v_f} - \frac{1}{v_i}\right) \tag{2.36}$$

$$\tilde{a} = \frac{Z_1 Z_2 e^2}{m_0 v_i v_f} \tag{2.37}$$

The excitation probability is given by

$$P_{i\to f} = |a_{if}|^2 \tag{2.38}$$

[6] An equivalent form of $\eta$ is $\frac{Z_1 Z_2 e^2}{\hbar v} = \frac{b}{2\lambda}$ where $b = 2Z_1 Z_2 e^2/m_0 v^2$ is the distance of closest approach, and $\lambda$ is the wavelength of the projectile

[7] $\frac{d\sigma}{d\Omega}_R = \frac{1}{4} a^2 \sin^{-4}(\vartheta/2)$, where $a$ is half the distance of closest approach $a = \frac{1}{2} b = \frac{Z_1 Z_2 e^2}{m_0 v^2}$

where the excitation amplitude $a_{if}$ can be calculated in first order perturbation theory if the strength of the interaction $V(\vec{r}(t))$ is weak,

$$a_{if} = \frac{1}{i\hbar}\int_{-\infty}^{+\infty}\langle f|V(\vec{r}(t))|f\rangle e^{i\Delta Et/\hbar}dt \tag{2.39}$$

See [23, 24] for details.

Once the electromagnetic interaction has been decomposed into its multipole components [23, 24], the differential cross section for electric excitation of the projectile of multipole order $\lambda$ is given by

$$d\sigma_{E\lambda} = \left(\frac{Z_t e}{\hbar\upsilon}\right)^2 a^{-2\lambda+2}B(E\lambda)df_{E\lambda}(\vartheta,\xi) \tag{2.40}$$

Expressions for the $df$ functions can be found in [23]. They are plotted in Fig. 2.3. The reduced transition probability, $B(E\lambda)$, is defined as

$$B(E\lambda; i\to f) = \frac{1}{2I_i+1}|\langle i||\mathcal{M}(E\lambda)||f\rangle|^2 \tag{2.41}$$

where $I_i$ is the total angular momentum of state $|i\rangle$, and $\mathcal{M}(E\lambda)$ is the electric multipole moment operator

$$\mathcal{M}(E\lambda) = \sum_k e_k r_k^\lambda Y_{\lambda\mu} \tag{2.42}$$

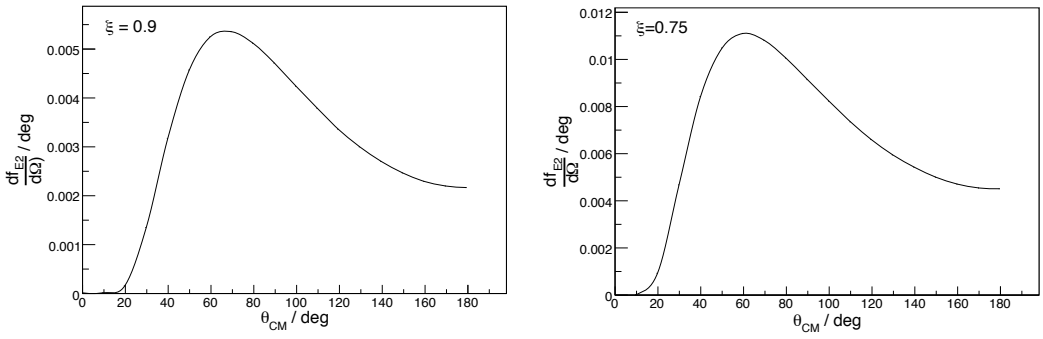


Figure 2.3: *The classical $df\,d\Omega$ functions. Values taken from Ref. [23]. The df functions calculated for $\xi$ values typical for the experiments discussed here, Tab 3.2*

# Chapter 3

# Experimental Method

The three nuclei, $^{106}$Sn, $^{108}$Sn, and $^{110}$Sn investigated in the present thesis require the use of Radioactive Ion Beams (RIBs). This chapter gives a brief description of the method of producing a RIB using the Isotope Separator On-line (ISOL) technique and the subsequent post-acceleration. The MINIBALL detector setup and acquisition system will also be outlined. The nomenclature of the three experiments is given in Tab. 3.1.

| Abbreviation | Experiment |
|---|---|
| X10 | $\sim 10^6$ pps $^{110}$Sn@2.82 MeV/u on a 2.0 mg/cm$^2$ thick $^{58}$Ni secondary target |
| X08 | $\sim 10^6$ pps $^{108}$Sn@2.82 MeV/u on a 2.0 mg/cm$^2$ thick $^{58}$Ni secondary target |
| X06 | $\sim 10^5$ pps $^{106}$Sn@2.83 MeV/u on a 2.0 mg/cm$^2$ thick $^{58}$Ni secondary target |

Table 3.1: *Reference abbreviations used in the text. E.g. X08 refers to the experiment where* $10^6$ $^{108}$*Sn particles per second at an energy of* 2.82 *MeV/u impinged on a* 2.0 *mg/cm*$^2$ *thick* $^{58}$*Ni target.*

**Coulomb Excitation Parameters**

The experimental conditions for the three experiments summarized in Tab. 3.1 lead to the Coulomb excitation parameters summarized in Tab. 3.2.

## 3.1 Production of Radioactive Isotopes at ISOLDE

Radioactive isotopes are produced at ISOLDE [27] by bombarding a thick primary target by $3 \cdot 10^{13}$ 1.4 GeV protons delivered by the CERN PS Booster (PSB) in a 2 $\mu s$ long pulse every 1.2 seconds, Fig. 3.1. Upon impact a wide range of exotic nuclei are formed by three different processes: spallation, fission, and fragmentation. Spallation is the process where high energy protons that impact upon the heavy target nucleus cause some $20 - 40$ nucleons to be knocked out and/or 'boiled off' by the heat produced in the collision. The target nuclei are shattered and the result is a few larger residues and a large number of free nucleons. Spallation requires high energy, $\geq 500$ MeV/u.

The isotopes produced in the primary target diffuse through the target material and effuse

| Parameter | X10 | X08 | X06 |
|---|---|---|---|
| $a_t^{sym}$ (fm) | 9.48 | 9.54 | 9.57 |
| $a_p^{sym}$ (fm) | 9.46 | 9.53 | 9.56 |
| $\eta_i$ | 131.8 | 131.8 | 131.5 |
| $\eta_{f,t}$ | 132.7 | 132.7 | 132.4 |
| $\eta_{f,p}$ | 132.5 | 132.5 | 132.3 |
| $\xi_t$ | 0.90 | 0.91 | 0.91 |
| $\xi_p$ | 0.75 | 0.75 | 0.75 |

Table 3.2: *Coulomb excitation parameters for the three experiments discussed in this licentiate thesis. The index $p/t$ appended to some parameters indicate projectile/target excitation. See Sec. 2.4*

into a cavity. It is crucial to shorten the release process in order not to lose beam intensity through radioactive decay. This is accomplished by heating the target to $\sim 1200$°C. The present experiments used a $LaC_X$ (Lanthanum Carbide) 27 g/cm2 thick primary target. The isotope of interest was singly ionized in the cavity using a three-step laser ionization scheme and extracted with a $60$ kV potential.

Yield measurements of the extracted beam showed that it was contaminated by In, see Paper I. The electro-chemical properties of In lead to surface ionization through contact with surrounding material and will accordingly contaminate the RIB. It is important to map the In isobaric contamination over time through the experiment, see Sec. 4.2.6). During the X08 experiment the In yield was reduced by adjusting a beam gate. The diffusion time through the primary target is shorter for In than for Sn. The beam gate was closed for 2.5 seconds after proton pulse impact and then open for 7 seconds before the next proton pulse arrived. For the X06 experiment the beam intensity was too low and the beam gate was not used in order to maximize the total yield from the primary target. For the X10 experiment the beam gate was opened immediately after proton pulse impact.

## 3.2 Post-acceleration at REX-ISOLDE

The low energy, singly charged, RIB delivered by ISOLDE is post-accelerated by the REX-linac. Before acceleration the ions are cooled, bunched, and charge bred. The increase in charge is advantageous especially for RIBs since it will shorten the acceleration distance of the beam and therefore the total time elapsed between ion production and experiment. Furthermore, the REX-linac requires a mass to charge ratio $A/q < 4.5$. The mass range can be extended by selecting certain charge states. More than 600 isotopes of approximately 70 elements are available [28].

Charge breeding is performed in the Electron Beam Ion Source (EBIS) [29]. Before injection into the EBIS, the beam is cooled and bunched by a Penning-type trap (REXTRAP) which is a $1.3$ m long construction contained in a superconducting magnet, that provides a $3$ T magnetic field parallel to the beam line. Depending on the beam, the cycle time is up to 20 ms.

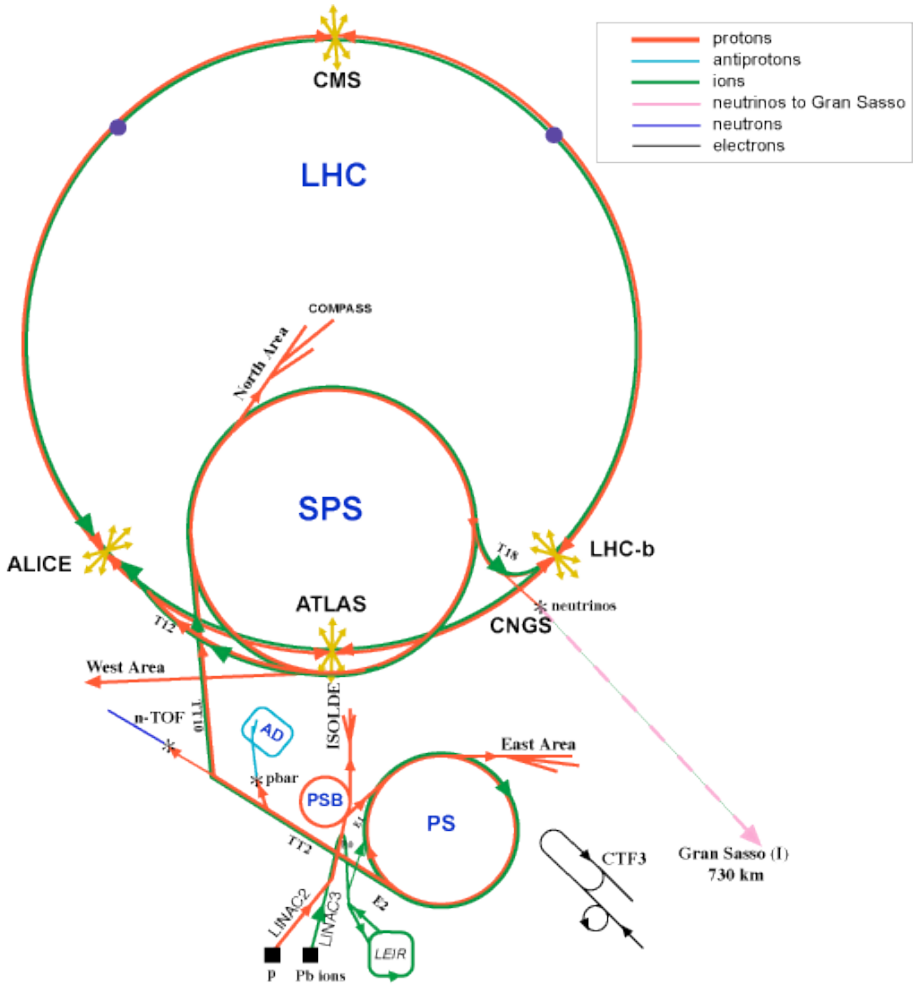


Figure 3.1: *The CERN accelerator complex. The protons are produced by stripping orbital electrons from hydrogen atoms. Linac2 accelerates the protons to 50 MeV and the PSB brings them up to 1.4 GeV. Some of the protons are delivered to ISOLDE while the remainder is injected into the Proton Synchrotron (PS) which supplies the entire CERN complex.*

The equations of motions inside an ideal Penning trap can be solved analytically [30]. Longitudinal confinement is provided by an applied electric potential. With a tuned buffer gas pressure[1] inside the trap, the energy loss due to collisions will be sufficient for the ions to not overcome the entrance potential after reflection at the exit potential barrier. Radial confinement of the particles is achieved by the applied magnetic field. The radial motion can be decomposed into two circular eigenmotions in the same direction, magnetron motion and reduced cyclotron motion, Fig. 3.3, with frequencies $\omega_-$ and $\omega_+$ respectively. The sum $\omega_+ + \omega_- = \omega_c$ is the true cyclotron frequency that depends on the charge of the ion, the magnetic field strength, and the ion mass. Due to collisions with the buffer gas the magnetron radius increases while the reduced-cyclotron motion is cooled. Hence, buffer gas cooling

[1] typically $10^{-4}$ mbar Ne in the trap center, [28]

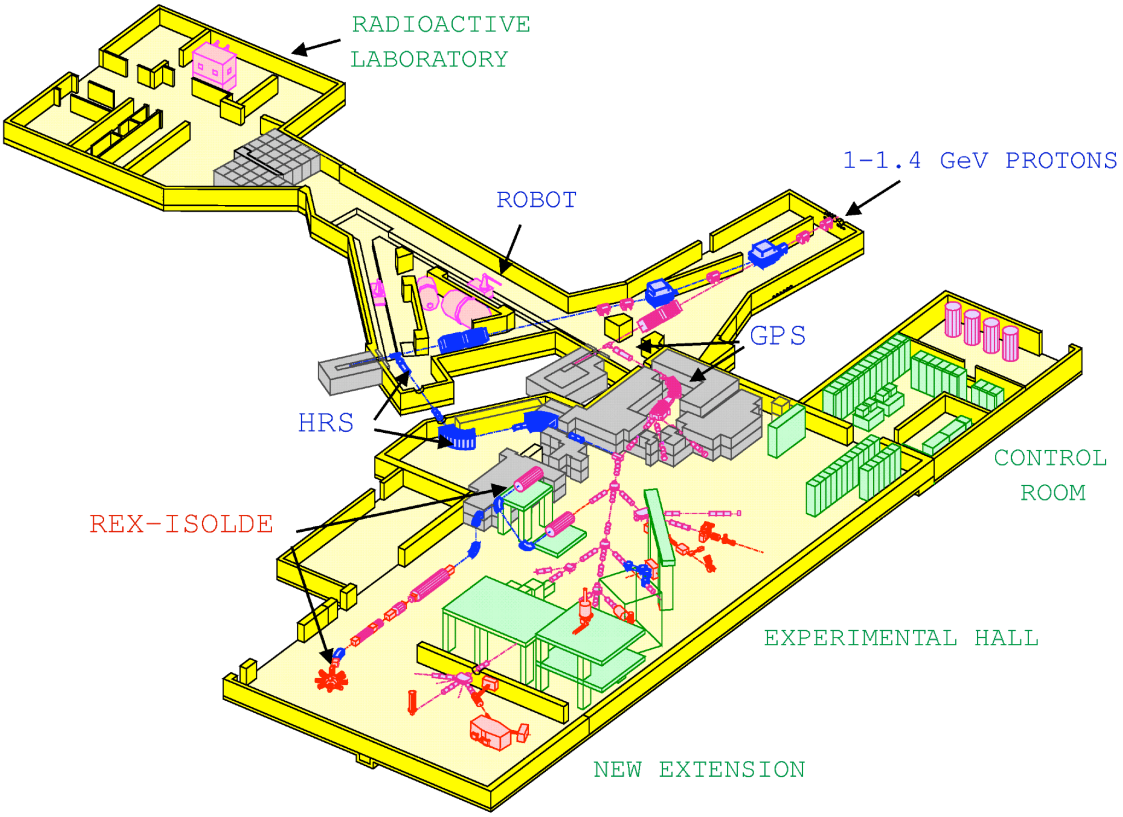


Figure 3.2: *The ISOLDE hall*

alone cannot cool the overall motion of the ions. A radio frequency field (rf) that oscillates with the cyclotron frequency $\omega_c$ couple the magnetron and reduced cyclotron motions. This so-called side-band cooling [31] causes an energy transfer between the two motions. The procedure is slightly perturbed by ion-ion interactions, but nonetheless the technique provide adequate cooling for injection into the EBIS.

The ion bunch is injected to the EBIS through a beam transfer line. Inside the EBIS a 4.5 keV strongly focused electron beam bombards the ions and they undergo stepwise ionization. The electron beam is confined in a 1m long cylindrical space by a longitudinal magnetic field. The ions are fixed in space by the negative potential of the electron beam and an electric potential. The charge breeding time increases with mass and charge state. The breeding time for the X06/X08 experiments were 67 ms for $26^+$ ions with a resulting beam period of 70 ms. The charge state for the Sn ions during the X10 experiment was $27^+$. The charge state of interest is selected by a mass separator after the EBIS. The separator also removes buffer gas remnants from the REXTRAP and the EBIS.

The beam energy is $\sim$ 5 keV/u after the EBIS and the REX-linac [32] accelerates the ions

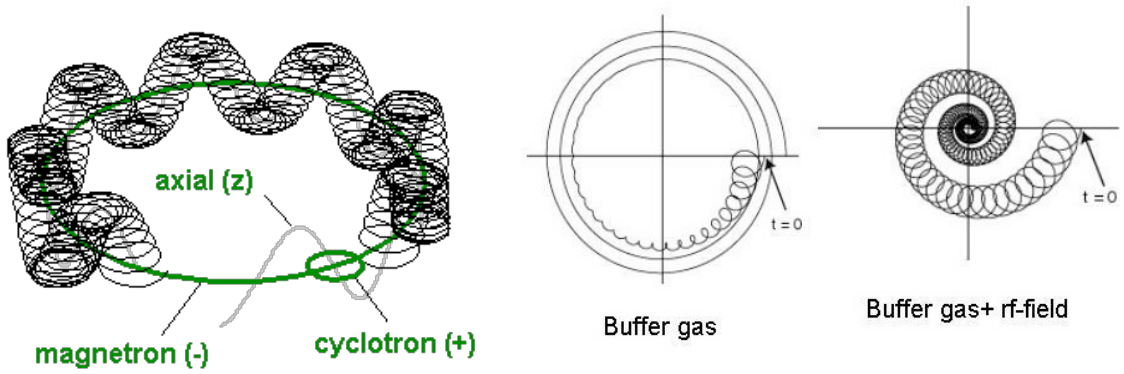


Figure 3.3: *(Left)The three eigenmotions of a single ion inside a Penning trap. The oscillation frequencies obey* $\omega_- << \omega_z << \omega_+ \approx \omega_c$*. (Center) The alone action of the applied magnetic field can not cool the ion motion. The radius of the magnetron motion increases. (Right) With the inclusion of an rf field the reduced-cyclotron motion and the magnetron motion is coupled and as a result radial cooling is achieved.*

to $\sim 3$ MeV/u. The linac consists of, in order, a radio-frequency quadrupole (RFQ), a resonator with drift tubes of increasing length (IH-structure), a 7-gap and a 9-gap resonator. For details about the linac and beam production at REX-ISOLDE see Ref. [28] and references therein.

## 3.3 Detectors

A schematic overview of the experimental process is presented in Fig. 3.4. Both the $^{58}$Ni target and the particle detector are placed in the target chamber, which is kept under a $10^{-6}$ mbar pressure. A PPAC monitors the beam, to steer it onto the center of the target. Approximately 1 m further downstream is the beam dump which is monitored by a coaxial Germanium detector. The angular coordinates are defined from a right-handed polar coordinate-system with the positive z-axis in the direction of the beam axis. The distance between the $^{58}$Ni target and the particle detector was $d = 30.6$ mm for the X10 experiment. For the X08/X06 experiments a few details had changed inside the target chamber. A protection plate originally mounted upstream in the chamber had been removed and was replaced by a tantalum collimator. The distance $d$ was calculated for the X08/X06 experiments using an $\alpha$-source placed at the target position. The geometry of the particle detector is known, and the ratio between the expected number of particles and the measured number of particles compared between all strips depend on $d$ due to differences in the solid angle coverage of each strip. Using this method gives $d = 30.0 \pm 0.6$ mm.

### 3.3.1 Particle Detector

The particle detector, Fig 3.5, is a circular Double-Sided Silicon Strip Detector [33] (DSSSD). The DSSSD comprises 4 independent quadrants. The front of the detector is divided into 16 annular strips of 1.9 mm width and 2 mm pitch. The back is divided into 24 sectors at $3.4^\circ$

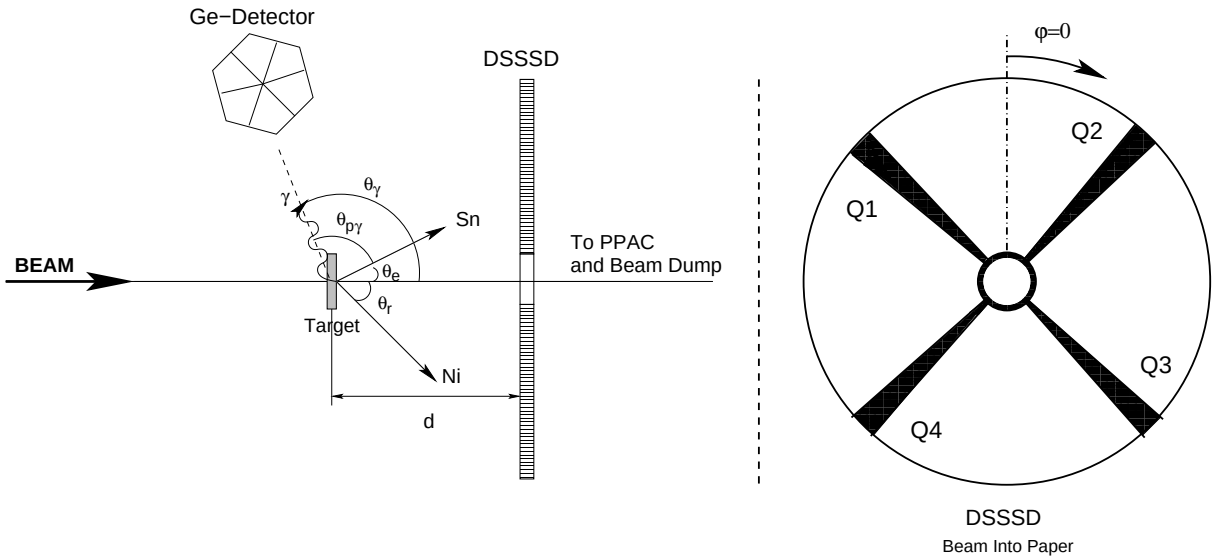


Figure 3.4: *A schematic drawing of the experimental setup. The angles are defined as they are referred to in the text.*

pitch, see Fig. 3.5. In total this gives $4 \cdot 16 \cdot 24 = 1536$ pixels for the DSSSD. However, in the electronic setup the radial back strips were connected pairwise, reducing the total number of pixels to 768. The Si wafer thickness was $480\ \mu m$. The active area of the detector was $91\%$ of the total area [34].

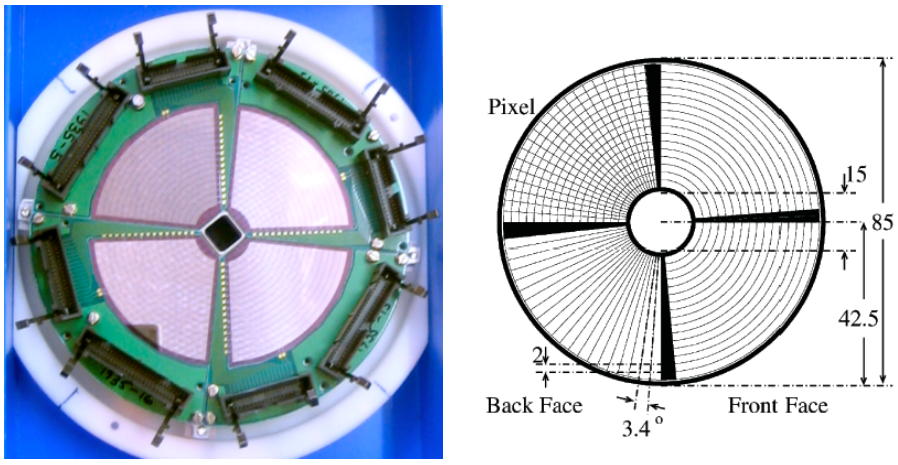


Figure 3.5: *The Double-Sided Silicon Strip Detector (DSSSD).*

### 3.3.2 $\gamma$-ray Detector

The MINIBALL detector array contains eight triple-clusters. Each triple-cluster comprises three $\gamma$-ray detectors, each referred to as a crystal. Each crystal is six-fold segmented. The

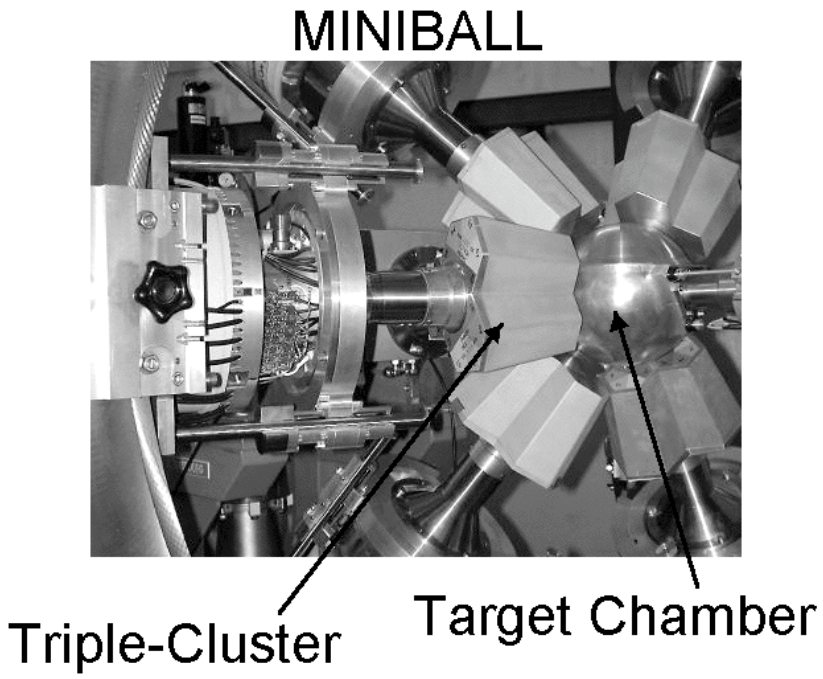


Figure 3.6: *The MINIBALL germanium detector array. Eight triple-clusters surround the target chamber in a close to $4\pi$ configuration.*

segmentation improves the angular resolution of the detected $\gamma$-ray. The crystals are High Purity Germanium (HPGe) detectors encapsulated in an aluminum cap. The six segments are read out independently. The central electrode of the crystal is referred to as the core to which the negative potential is applied. The voltage required to reach a sufficient depletion region is $2.5-4.5$ kV per crystal. The crystals are kept at liquid nitrogen (LN2) temperatures, supplied by LN2 transfer lines from a 500 liter dewar to each triple-cluster.

The distance between the $^{58}$Ni target and the crystal was $12.5$ cm. The tripe-cluster center to cluster core center distance was $3.5$ cm. The point of $\gamma$-ray interaction was assumed to be the center of gravity of the segment surface. The total solid angle coverage for the MINIBALL in this configuration is $\sim 60\%$ of $4\pi$ [34]. The position of a triple cluster is determined by three angles ($\theta$,$\phi$,$\alpha$), defined in Fig. 3.7

## 3.4 Electronic Setup and Data Acquisition

For a detailed description of the electronics setup see Ref. [35]. The experimental output are primarily of two different types; particle data and $\gamma$-ray data. Also in the particle data stream the DSSSD is divided into four quadrants. Each quadrant is treated separately from every other. As mentioned, the 24 radial back strips of a quadrant are paired in the hardware to 12 channels. The 16 annular front strips of each quadrant are all read out. For the X08/X06 experiments it was possible to distinguish multiple front/back signals within the same quadrant, while for the X10 experiment this was impossible since the electronic setup

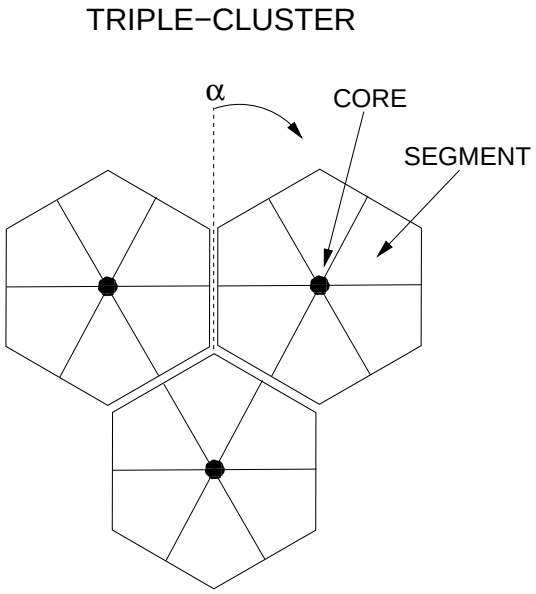


Figure 3.7: *A schematic drawing of a MINIBALL triple-cluster. The* $(\theta, \phi)$ *angles are defined from the same right-handed polar coordinate system as the rest of the experimental setup. The* $\alpha$ *angle determines the clockwise (as seen from the target position) rotation around the center of the triple-cluster.*

did not include TDC front strip readout.

The six segment signals plus one core signal from each $\gamma$-ray detector were read out by two XIA DGF modules [36]. The energy of the $\gamma$-ray was stored in the core channel. Pulse shape analysis [37] was not used in the experiment since it has a very small effect in this case [38]. The DGF modules were synchronized using a so called BUSY-SYNCH loop. When a DGF starts a run the BUSY output is set to logic one. All the BUSY outputs are OR'ed in a fan-in/fan-out module and the output is sent back into the input called SYNCH of each DGF. In this way all the DGF modules will start and stop acquisition at the same time.

A $\gamma$-gate signal was created whenever a core signal was detected. When the $\gamma-$gate was coincident with a particle signal a logic signal was sent to the trigger box. If the particle-$\gamma$ time difference was larger than $800$ ns the trigger box gave a signal only every $2^n$ coincidence, so-called downscaling. The experiments presented in this licentiate thesis use a downscaling of $n = 6$ ($2^6 = 64$). The signals required to produce an ADC readout gate are summarized and presented in Fig. 3.8.

Particle and $\gamma$-ray signals were correlated in time by sending each DSSSD gate to a dedicated DGF timestamp module.

### 3.4.1 MED Data Format

Data was written to disc in MED format (MBS Event Data) [39] which is a standard format. Notations used here are compliant with Ref. [39].

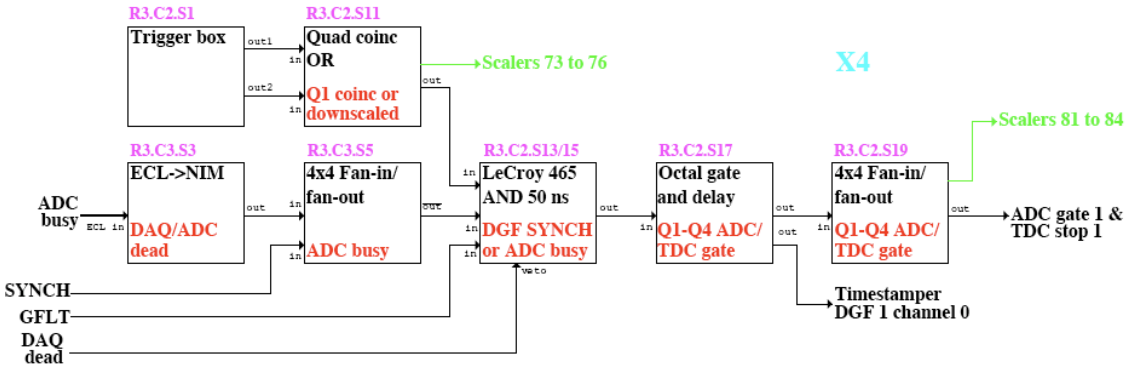


Figure 3.8: *The ADC gate will be produced and all the TDC modules will be stopped if: either particle-$\gamma$ coincidence or a downscaled particle was detected* ***and*** *either on or off window is detected (indicated by GFLT)* ***and*** *the ADC is not busy* ***and*** *the DGF is not busy* ***and*** *the DAQ is not dead.*

An MED data file contains a stream of MBS events of standard type. Each event contain a series of sub-events that follow the MARABOU [40] event type standard. The two types of sub-event formats of primary importance are given in the list below.

- DGF sub-event format. The $\gamma-$ray data storage format.
- CAEN sub-event format. The particle data storage format.

### DGF sub-event Buffer

Three types of information, which are of primary importance for the analysis, are stored in the XIA DGF sub-event buffer:

- The energy, timestamp, module number, and channel of the detected $\gamma-$ray. The timestamp gives the time of detection. The module number identifies which Ge-crystal the $\gamma$-ray was detected in. The channel is a number between 0 and 3, and identifies which segment the $\gamma$-ray was detected in.
- Particle DGF-timestamps. For each particle gate, the corresponding time is stored in a dedicated DGF module. A common time scale enable the particles to be correlated with the $\gamma$-rays.
- ISOLDE signal timestamps: EBIS, T1, PS. For each ISOLDE event, the time is stored in a dedicated DGF. The EBIS timestamp indicates the time of release of the particles. The T1 timestamp gives the time of the last proton pulse impact on the target. The PS timestamp gives the time of the last proton supercycle. A supercycle is defined as a group of 12 proton pulses.

A full account of the DGF sub-event buffer is given in Tab. 3.3. To relate a DGF module/channel number etc. with the physical equipment require information about the hardware cabling. The module numbers and channels used in the data analysis code is presented

| | buffer header |
|---|---|
| `buffer wc` | number of 16 bit words in this buffer |
| `module number` | module serial number[a] |
| `format descriptor` | data format used for channel data |
| `buffer time` | 48 bit buffer starting time |
| | event header |
| `hit pattern` | one bit per active channel |
| `event time` | 32 bit event starting time |
| | channel header |
| `word count` | number of 16 bit words written for this channel |
| `fast trigger time` | time of arrival |
| `energy` | converted energy value (note, not in keV) |
| `PSA value` | pulse shape analysis information |
| `GSLT time` | 48 bit arrival time of global second level trigger |
| `realtime` | time since last reboot or reset |
| `trace data` | array containing trace data |

[a] serial configuration stored in .rc file from running the Config.C script

Table 3.3: *DGF Sub-event buffer content. On the left hand side is the name of each data container as defined in [39] and on the right hand side a short description. See text and Ref. [39] for details.*

in Tab. 3.4 The time stamp is given in two formats, `realtime` and `fast trigger time`.

| `moduleNumber` | `channel` |
|---|---|
| 1-48 | For odd `moduleNumber` chn0=core chn1=seg chn2=seg chn3=empty<br>For even `moduleNumber` chn0=seg chn1=seg chn2=seg chn3=seg[a] |
| 49 | chn0=DSSSD Q1 DGF timestamp |
| 50 | chn0=DSSSD Q2 DGF timestamp |
| 51 | chn0=DSSSD Q3 DGF timestamp |
| 52 | chn0=DSSSD Q4 DGF timestamp |
| 53 | chn0=EBIS chn1=T1 chn2=PS |

[a] As mentioned, two DGF modules are required for each Ge-crystal.

Table 3.4: *The DGF modules, identification moduleNumber, and the physical equipment*

The `fast trigger time` is the time elapsed since the start of the event, and the `realtime` is the time with respect to a much larger time scale stretching over the entire experiment and longer. Time differences stretching over event boundaries must use `realtime`.

**CAEN sub-event buffer**

The particle ADC/TDC (CAEN V775) [41] were stored in the CAEN type sub-event buffers. Each CAEN buffer may contain up to 32 events. Each event is tagged with the module number. This is the information needed to connect the buffer data with the correct quadrant. The critical information is the module serial number and the channel data. The differences

| | |
|---|---|
| `crate` | crate number[a] |
| `wc` | number of channel data (32 bit) |
| `mserial` | module serial number |
| `channel` | channel number (0...31) |
| `data` | 12 bit ADC/TDC data + 1 bit overflow + 1 bit underflow |
| `event count` | number of events since the last reset |

[a] not used

Table 3.5: *The CAEN sub-event buffer*

| `mserial` | detector | information |
|---|---|---|
| 55 | DSSSD Q1 | ADC energy |
| 56 | DSSSD Q2 | ADC energy |
| 57 | DSSSD Q3 | ADC energy |
| 58 | DSSSD Q4 | ADC energy |
| 59 | DSSSD Q1 | TDC time |
| 60 | DSSSD Q2 | TDC time |
| 61 | DSSSD Q3 | TDC time |
| 62 | DSSSD Q4 | TDC time |

Table 3.6: *The CAEN modules and the corresponding information*

between the X10 experiment and the X08/X06 experiments regarding the hardware cabling and the type of data stored are:

- **X10:**
  - ADC chn 0-15: Front plane annular strips 0-15. Physically the strips are numbered from outer strip→ inner strip.
  - ADC chn 16-27: Back plane sector strips 0-11. Physically in the clockwise direction as seen from the direction of the beam.
  - TDC chn 0-11: Back plane TDC time for sector strips 0-11. Physically in the clockwise direction as seen from the direction of the beam.
  - No TDC Front plane data in data stream.
- **X08/X06:**
  - ADC chn 0-15: DSSSD front plane annular strips 0-15. Physically the strips are numbered from outer strip→ inner strip.
  - ADC chn 16-27: DSSSD back plane sector strips 0-11. Physically in the clockwise direction as seen from the direction of the beam.
  - TDC chn 0-7: DSSSD front plane TDC time for annular strips 0-15. The strips were coupled pairwise in the hardware.
  - TDC chn 16-27: DSSSD back plane TDC time for sector strips 0-11. Physically in the clockwise direction as seen from the direction of the beam.
  - ADC DSSSD Q1 chn 29: Laser Power (not present in the X10 experiment).

**Pattern Unit**

The pattern unit (PU) is read out for each ADC gate. The PU contains data regarding the particle data written and the laser status.

| bit | information |
|---|---|
| 1 | Downscaled particle Q1 |
| 2 | Particle-$\gamma$ coincidence Q1 |
| 3 | Downscaled particle Q2 |
| 4 | Particle-$\gamma$ coincidence Q2 |
| 5 | Downscaled particle Q3 |
| 6 | Particle-$\gamma$ coincidence Q3 |
| 7 | Downscaled particle Q4 |
| 8 | Particle-$\gamma$ coincidence Q4 |
| 9 | Laser flag (not present in the X10 experiment) |

Table 3.7: *Pattern Unit (PU) bits. A bit=1 means TRUE and 0 means FALSE. Regarding bit 9, the laser flag, 1 means Laser On, and 0 means Laser Off.*

## 3.5 Physical Event Structure

In our case a physical event involves two scattered particles and a $\gamma$-ray. To construct the physical event two pieces of information are needed; a particle-particle time coincidence cut and a particle-$\gamma$ time coincidence cut.

A particle was reconstructed from signals coincident in time between the front plane and the back plane of the DSSSD.

- For the X10 experiment there was no TDC front plane information. Therefore a particle was constructed only when the front plane *and* back plane hit multiplicity was equal to one.
- For the X08/X06 experiments a front-back hit time coincidence condition of 90 ns was deduced. Imposing this condition in the data analysis increased the number of particles possible to construct with 80%.
- A time coincidence condition of 60 ns was obtained for adjacent strip coincidences between the front plane or back plane strips. In total, 20% of the front plane hits and 13% of the back plane hits were coincident. The strip energies were added, and the strip with the highest energy was chosen to represent the position of the combined signal and the time was set to the average time of the two signals. With adjacent strip coincidences the ambiguous front-back particle coincidences were 4%.

The energy of the physical particle is the sum of the front and back plane energy and the particle time is the DGF time stamp for the corresponding quadrant.

Two different types of particle events can occur. Due to the kinematical situation, see Sec. 4.2.3,

the recoil can scatter with angles larger than what is covered by the particle detector. The projectile always undergo scattering with angles lower than the maximum particle detection angle. There exists an angular interval (2p range) that is covered by the DSSSD and in which both the projectile and recoil within the same event can scatter simultaneously. This type of event is called a two-particle event (2p). The particles in a 2p event are detected in opposite quadrants, see Fig. 3.9.

- Two scattered particles were considered to be of 2p type if they were detected in opposite quadrants of the DSSSD. Furthermore, the time difference between them had to be less than 100 ns, as deduced from Fig. 3.9.
- If only one particle was detected in the 2p range of the detector, the event was classified as a 1p event.
- The entire data set was composed of, 40% 2p events and 60% 1p events for the X10/X08 experiments, while for the X06 experiment the fractions were 80% 2p and 20% 1p. This merely reflects the effect of a higher particle rate in the X10/X08 experiments.

Regarding the $\gamma-$ray data:

- The $\gamma$-rays within a 4$\mu$s time window around each particle or particle pair[2] were assigned to the event.
- If a $\gamma$-ray could not be assigned to a particle unambiguously in time it was discarded.
- No $\gamma-$rays had to be discarded in the 2p event subset.
- For 1p events, a maximum of 4% of the $\gamma$-rays were discarded in the data from the X08 experiment.

[2]For 2p events the average time of the pair was used as particle timestamp.

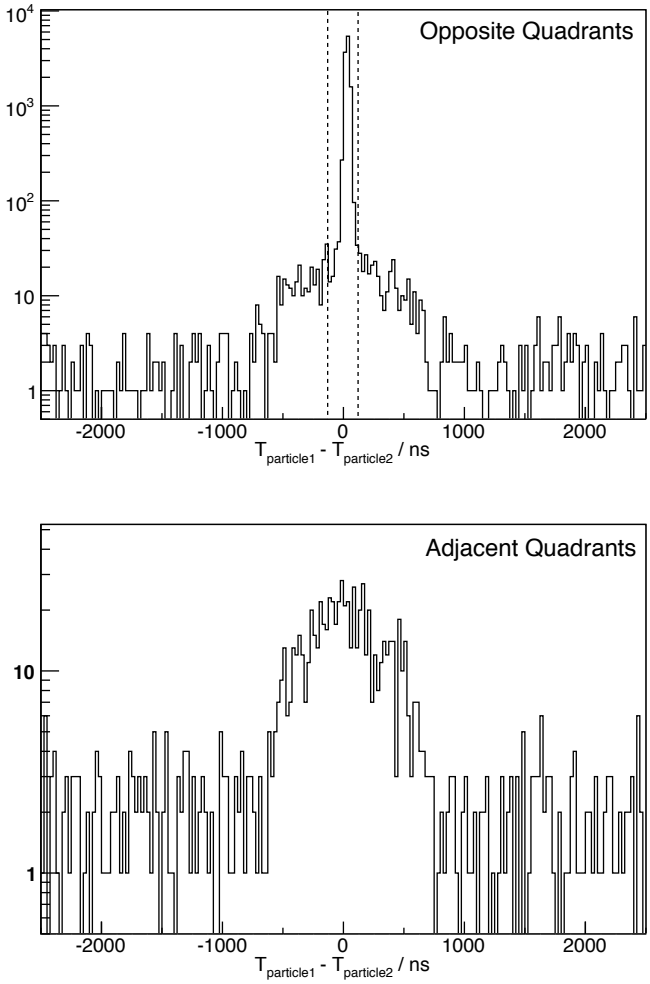


Figure 3.9: *The data is from the X08 experiment. Time difference between scattered particles within an MED event buffer. Particles are scattered in a plane and true coincidences will therefore occur in opposite quadrants. A 2p coincidence cut 100 ns was determined, indicated with dashed lines.*

# Chapter 4

# Data Analysis

This chapter describes the method used to extract the reduced transition probabilities,

$$B(E2; 0^+_{\rm gs} \rightarrow 2^+_1) \tag{4.1}$$

for the $^{106,108,110}$Sn isotopes. The low lying energy levels of the Sn isotopes are shown in Fig. 4.2.

## 4.1 Software

The data analysis was carried out within the ROOT framework [42]. The computer codes for offline data analysis were developed during the course of the work, Fig. 4.1.

- Format Conversion: convert MED data file, Sec. 3.4.1, to ROOT format. The I/O handling is based on R. Lutter's mbs2asc program [43].
- Event Building: Build physical events, Sec. 3.5.
- Analysis: Programs for Doppler correction.
- GOSIA2: Coulomb excitation analysis software written by T. Czosnyka et al. [26].

ROOT is a program intended for data analysis of particle and nuclear physics experiments. The ROOT data file can be handled with C++ compatible scripts and programs. The data file is compressed, but the access to a specific entry is very fast.

## 4.2 Analysis Method

The signature of Coulomb excitation from a state $|i\rangle$ to a state $|f\rangle$ is two scattered particles in coincidence with one emitted $\gamma$-ray coming from the $|f\rangle \rightarrow |i\rangle$ transition. The analysis comprised three steps:

- A particle-$\gamma$ coincidence condition.
- Doppler correction of detected $\gamma$-rays.
- Determination of the isobaric contamination of the beam, see Sec. 3.1.

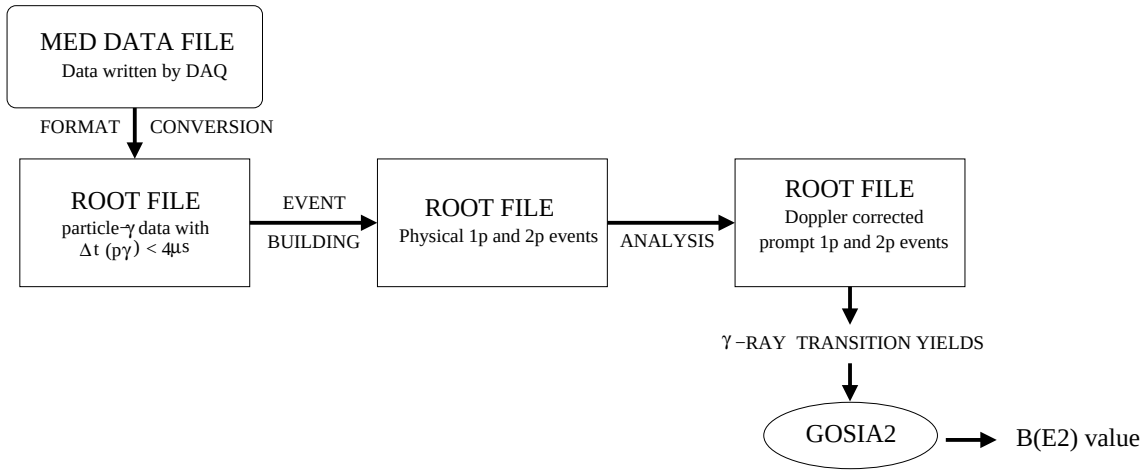


Figure 4.1: *Overview of the data-analysis method.*

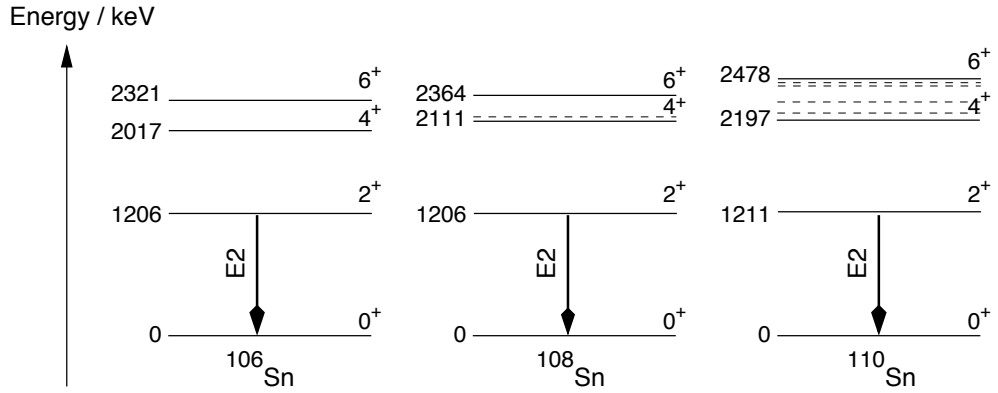


Figure 4.2: *The low lying energy levels in the $^{106,108,110}$Sn isotopes. The $6^+$ state present in all three isotopes is isomeric due to the small $E(6^+) - E(4^+)$ energy difference. The isomer hampers any lifetime measurement when populating the $2_1^+$ state from above. Therefore the method of sub-barrier Coulomb excitation is especially advantageous in these isotopes.*

Equation 4.2 relates the experimental data with the $B(E2)$ value of interest

$$B(E2)_{Sn} \propto \cdot \frac{N_\gamma(Sn)}{N_\gamma(Ni)} \cdot \frac{\varepsilon_\gamma(Ni)}{\varepsilon_\gamma(Sn)} \cdot B(E2)_{Ni} \cdot \mathcal{R}^{-1} \cdot \mathcal{W} \tag{4.2}$$

where $N_\gamma$ is the number of counts in the Coulomb excitation peak, $\varepsilon_\gamma$ is the relative $\gamma$-ray detection efficiency, $\mathcal{R}$ is the fraction of the the $N_\gamma(Ni)$ due to excitation caused by the Sn ions, $\mathcal{W}$ is the $\gamma$-ray angular distribution ratio between the projectile and target. In order to evaluate the proportionality in Eq. 4.2 exactly, the expression in Eq. 2.40 are integrated for both projectile and target for each experiment. The integration is done by GOSIA2, see Sec. 4.4.

### 4.2.1 Add-Back and $\gamma$-ray Detection Efficiency

The add-back routine increases the number of $\gamma$-ray counts in the peaks of interest. If two $\gamma$ rays are detected within a time window of $|\Delta t| < 100$ ns, Fig. 4.3, in neighboring Ge-crystals within the same triple-cluster their energies are added. The direction $(\theta_\gamma, \varphi_\gamma)$ of the resulting add-back $\gamma$-ray was chosen to correspond to the crystal in which the most energetic original $\gamma$ ray was detected. The resulting add-back $\gamma$-ray spectrum contains $\sim 10\%$ more statistics, Fig. 4.4. Add-back was used only for the X08/X06 experiments. Only the relative

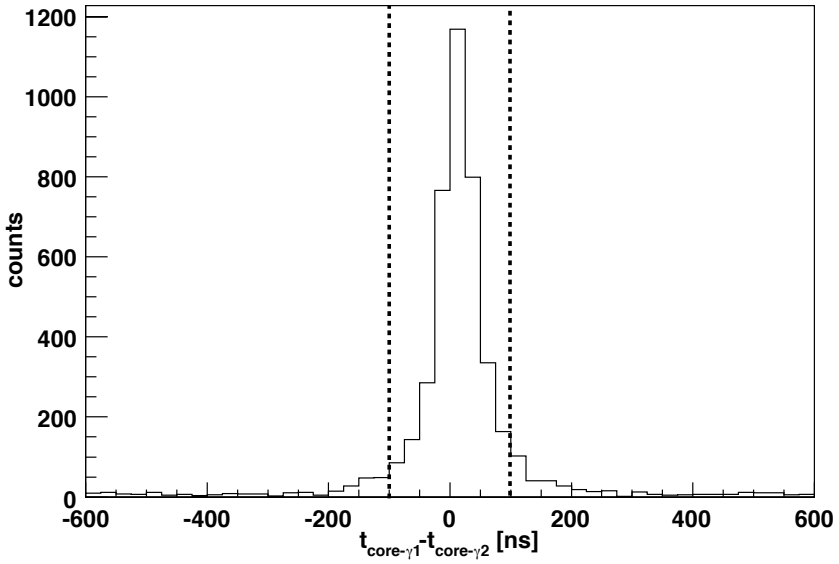


Figure 4.3: *Time difference between $\gamma$ rays in neighboring crystals within the same triple cluster. The dashed lines indicate the time coincidence cut of $|\Delta t| < 100ns$. If two gamma rays are detected within $\Delta t$ their energy are added. The plot shows $^{152}$Eu calibration data from X08. The corresponding plot for X06 is similar and the same time coincidence cut was extracted.*

efficiencies are of relevance in Eq. 4.2. This efficiency was determined by measuring single $\gamma$-rays from a $^{152}$Eu source. The relative intensities of the emitted $\gamma$-rays are known from Ref. [44]. The resulting efficiency curves are given in Fig. 4.5.

### 4.2.2 Particle-$\gamma$ Coincidence

The time difference,$\Delta t_{p\gamma}$, between a particle and a $\gamma$-ray allow for selecting only true particle-$\gamma$ coincidences, referred to as prompt. A $\Delta t_{p\gamma}$ was set for each quadrant. Table. 4.1 gives a a summary of all cuts and Figs. 4.6 and 4.7 show typical particle-$\gamma$ time differences. It is crucial to align the timing of the DAQ such that the prompt peak is not downscaled. See Sec. 3.4 for details regarding downscaling.

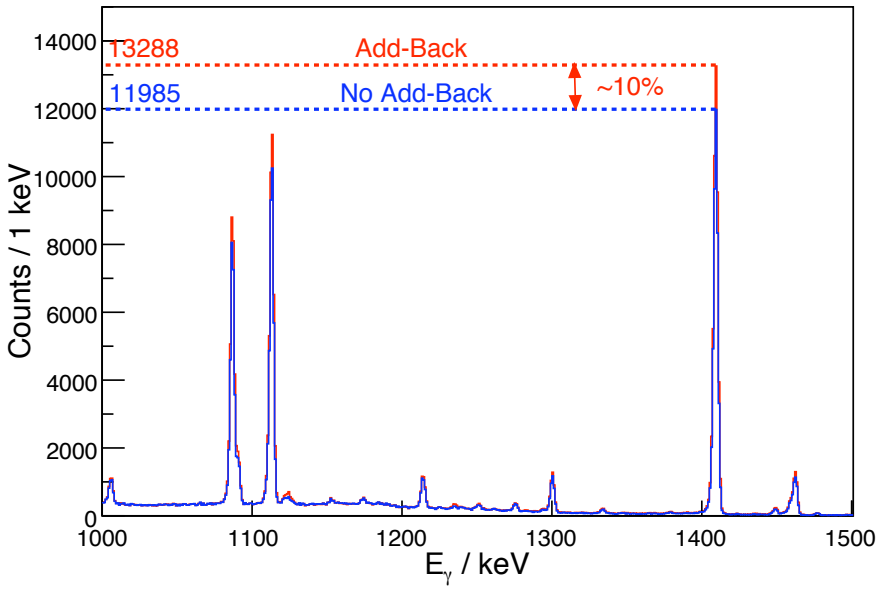


Figure 4.4: *$\gamma$-ray spectrum from a $^{152}$Eu source placed in the target position. The red $\gamma$-ray peaks include the add-back correction. The blue $\gamma$-ray peaks does not include the add-back correction. The peak marked for comparison in this figure is located at* 1408.0 *keV.*

### 4.2.3 Energy Loss and Kinematics

In our case the projectile nucleus is two times as heavy as the target nucleus leading to inverse kinematics. The mass asymmetry between target and projectile also implies a forward focused momentum cone and an upper limit of the projectile scattering angle in the laboratory frame of reference, $\theta_{LAB}^{max}$ [45]

$$\tan\theta_{LAB}^{max} = \frac{1}{\sqrt{K^2-1}}, \quad K = \frac{V}{\bar{v}} \tag{4.3}$$

where $V$ is the velocity of the center of mass frame in the laboratory, and $\bar{v}$ is the projectile velocity in the center of mass frame. The projectile $\theta_{LAB}^{max}$ is clearly visible in the left and right panels of Fig. 4.8. The scattered target nucleus has a maximum scattering angle larger than the angular coverage of the particle detector. As mentioned in Sec. 3.5, the 2p region is defined as the angular interval of detection into which a projectile and a target particle can scatter simultaneously. The lower limit of the 2p region is denoted $\theta_{2p}$.

The projectiles will undergo energy loss when traveling through the 2 mg/cm$^2$ thick (equivalent to 2.24 $\mu m$) $^{58}$Ni target. The energy loss per unit length traveled in the target, $dE/dx$, was calculated using the computer code SRIM [46]. Table 4.2 summarizes $\theta_{2p}$ assuming scattering in the center of the target with energy loss included. The 2p region is defined from these values.

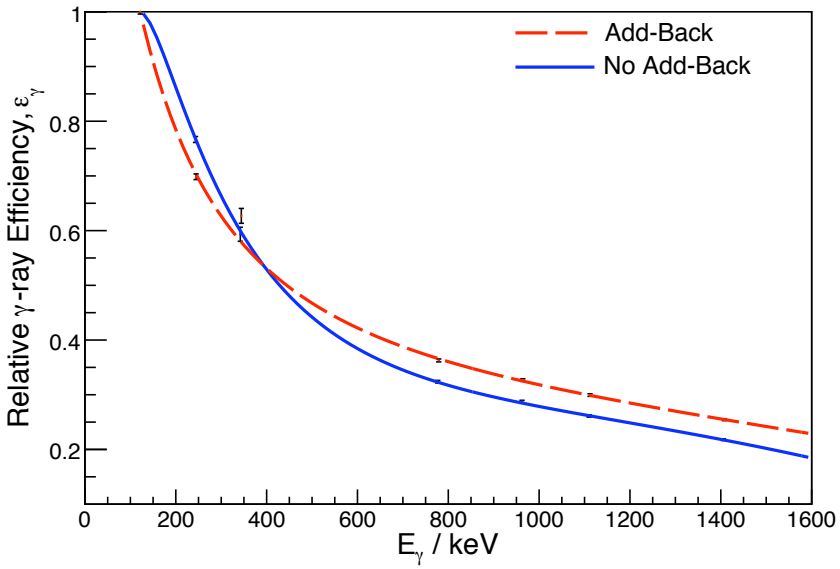


Figure 4.5: *Relative$\gamma$-ray efficiency curves for MINIBALL from X08/X06 based on a $^{152}$Eu source at the target position. The curves are parameterized using $\ln(\varepsilon_\gamma) = \sum_{i=0}^{4} A_i(\ln(E_{keV}))^i$. Note the difference in the $\gamma$-ray efficiency between using add-back and not.*

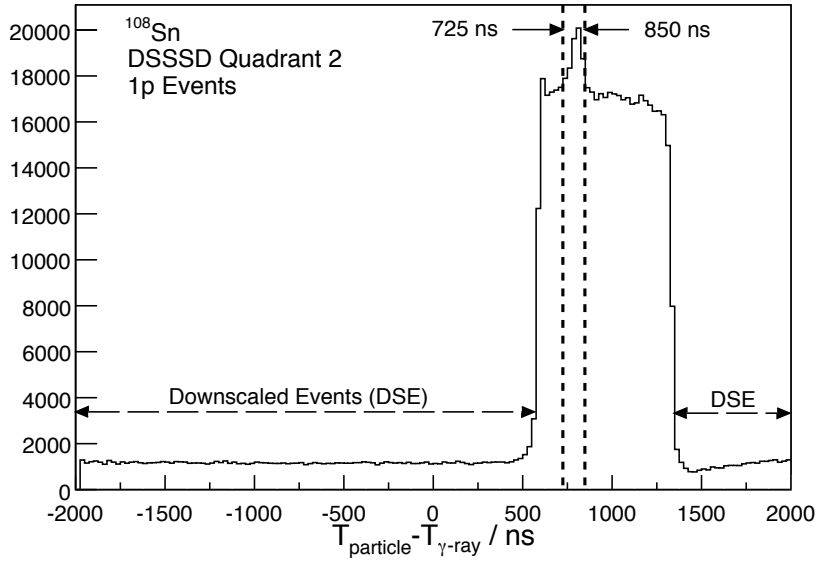


Figure 4.6: *Particle-$\gamma$ time difference spectrum for 1p events.*

Due to the finite width of the beam spot, the two different branches in Fig. 4.10 will be broadened. Imposing the 2p cut have many advantages. In the angular region below $24^\circ$

| Experiment | Quadrant | Event Type | $t_{p\gamma}^{low}$ / ns | $t_{p\gamma}^{high}$ /ns | $\lvert\Delta t_{p\gamma}\rvert$ / ns |
|---|---|---|---|---|---|
| X10 | Q1 | 1p | 710 | 840 | 130 |
| X10 | Q2 | 1p | 1143 | 1238 | 95 |
| X10 | Q3 | 1p | 718 | 810 | 92 |
| X10 | Q4 | 1p | 1045 | 1133 | 88 |
| X10 | Q1 | 2p | 710 | 840 | 130 |
| X10 | Q2 | 2p | 1143 | 1238 | 95 |
| X10 | Q3 | 2p | 718 | 810 | 92 |
| X10 | Q4 | 2p | 1045 | 1133 | 88 |
| X08 | Q1 | 1p | 725 | 825 | 100 |
| X08 | Q2 | 1p | 725 | 850 | 125 |
| X08 | Q3 | 1p | 700 | 800 | 100 |
| X08 | Q4 | 1p | 700 | 825 | 125 |
| X08 | Q1 | 2p | 700 | 800 | 100 |
| X08 | Q2 | 2p | 700 | 825 | 125 |
| X08 | Q3 | 2p | 700 | 800 | 100 |
| X08 | Q4 | 2p | 750 | 825 | 75 |
| X06 | Q1 | 1p | 725 | 825 | 100 |
| X06 | Q2 | 1p | 750 | 850 | 100 |
| X06 | Q3 | 1p | 700 | 800 | 100 |
| X06 | Q4 | 1p | 750 | 850 | 100 |
| X06 | Q1 | 2p | 725 | 800 | 75 |
| X06 | Q2 | 2p | 750 | 850 | 100 |
| X06 | Q3 | 2p | 700 | 800 | 100 |
| X06 | Q4 | 2p | 700 | 825 | 125 |

Table 4.1: *Summary of the particle-$\gamma$ time differences ,$t_{p\gamma}$. The condition is $t_{p\gamma}^{low} < t_{p\gamma} < t_{p\gamma}^{high}$. The width of the prompt peak is given by $\Delta t_{p\gamma}$.*

| Projectile | $\theta_{LAB}^{max}$ | $\theta_{2p}$ | $E_{center}$ |
|---|---|---|---|
| $^{110}$Sn | 31.6° | 24.1° | 263 MeV |
| $^{108}$Sn | 32.2° | 23.9° | 268 MeV |
| $^{106}$Sn | 32.9° | 24.3° | 254 MeV |

Table 4.2: *$\theta_{LAB}^{max}$ is the projectile maximum scattering angle in the laboratory frame of reference. $\theta_{2p}$ is the theoretical angle above which $2p$ events occur. $E_{center}$ is the energy of the projectile in the center of the target.*

it is difficult to make a clear separation between targets and projectiles. It should also be pointed out that the Coulomb excitation cross section is smaller for lower scattering angles as seen in Fig. 2.3.

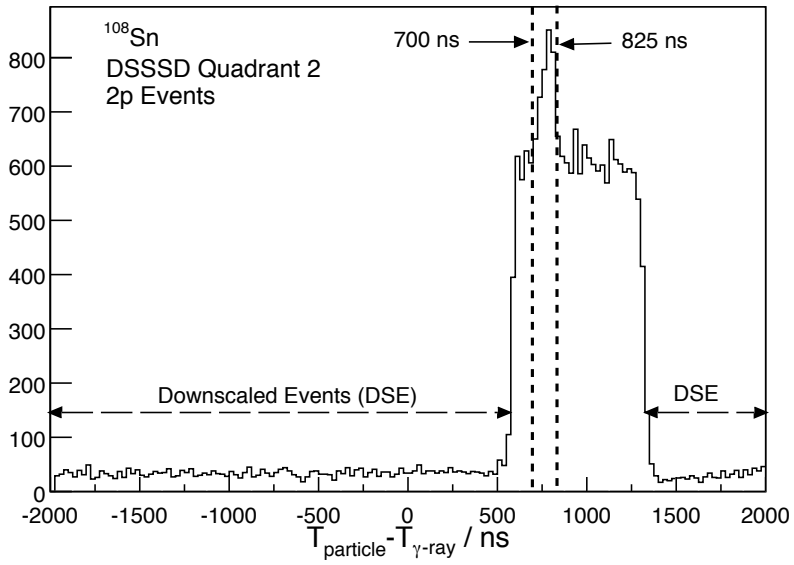


Figure 4.7: *Particle-$\gamma$ time difference spectrum for 2p events. Notice the relatively more prominent prompt peak as compared to Fig. 4.6*

### 4.2.4 Doppler Correction and $\gamma$-ray Angular Distribution

The projectile and recoil velocities are $\sim 0.05$c and $\sim 0.07$c, respectively. The $\gamma$-rays of interest are emitted in-flight and therefore Doppler shifted in energy due to the Doppler effect. This means that the $\gamma$-rays have to be Doppler corrected. The Doppler correction formula is given by

$$E_\gamma = \gamma E_\gamma^{detected} \cdot (1 - \beta \cos\theta_{p\gamma}) \tag{4.4}$$

where $E_\gamma$ is the rest frame energy of the emitted $\gamma$-ray and $E_\gamma^{detected}$ is the energy detected by the MINIBALL detector. The relativistic quantities are defined as $\beta = v/c$ and $\gamma = 1/\sqrt{1-\beta^2}$. The angle between the particle direction of motion and the direction of the $\gamma$-ray is given by

$$\cos\theta_{p\gamma} = \sin(\theta_p)\sin(\theta_\gamma)\cos(\phi_p - \phi_\gamma) + \cos(\theta_p)\sin(\theta_\gamma) \tag{4.5}$$

The detector positions determined from the MINIBALL frame where the detectors are mounted does not exactly correspond to their true position. By varying the angles of the detectors in the offline analysis, the shape of the Doppler corrected peaks could be optimized. The aim was to reach a small full width half maximum (FWHM) for the Doppler corrected $\gamma-$ray peaks.

The $\gamma$-rays are emitted in-flight from target and projectile nuclei which have different masses. This leads to different $\gamma$-ray angular distributions, which are evaluated and corrected for. This is handled internally by GOSIA2 in the calculation of the $B(E2)$ value. However, it is interesting to get a handle on the size of the effect. The $\gamma$-ray angular distribution for an E2 excitation is given by [23]

$$W_{CM}(\vartheta_\gamma) = 1 + A_2^{(2)} \cdot a_2^{E2}(\eta,\xi)P_2(\cos\vartheta_\gamma) + A_4^{(2)} a_4^{E2}(\eta,\xi)P_4(\cos\vartheta_\gamma) \tag{4.6}$$

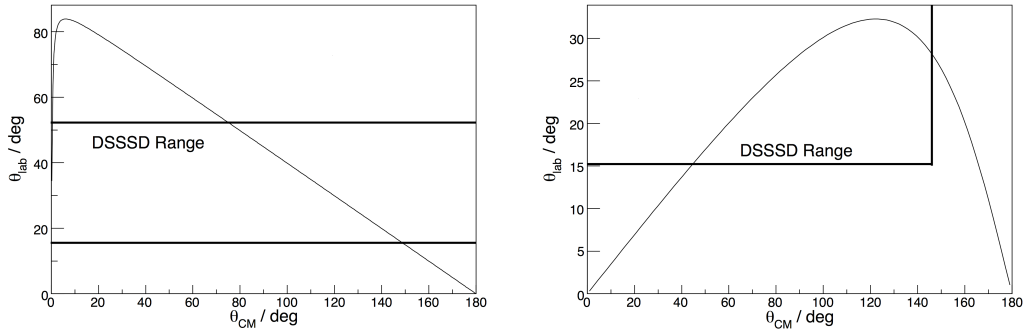


Figure 4.8: *Kinematical plots calculated using a projectile with an energy of 310 MeV in the laboratory frame of reference.(Left) Target: Scattering angle in the laboratory frame of reference versus scattering angle in the center of mass frame of reference. (Right) Projectile: Scattering angle in the laboratory frame of reference versus scattering angle in the center of mass frame of reference*

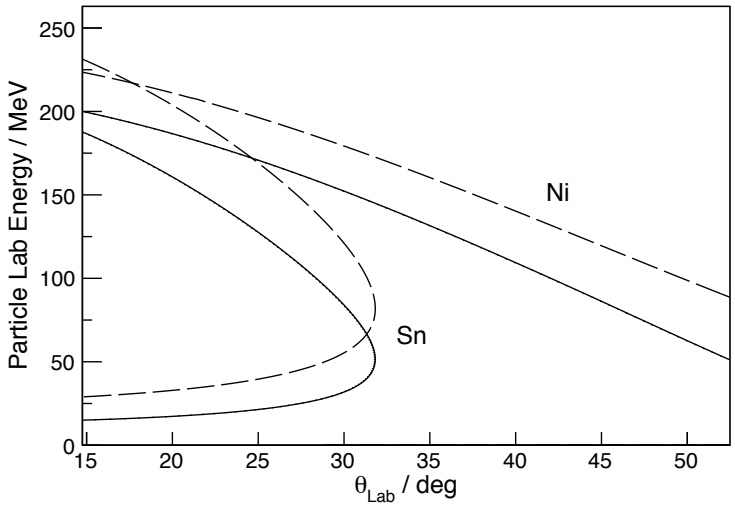


Figure 4.9: *Scattered particle energy plotted against scattering angle. The dashed curves assume scattering in the center of the target. The solid curves include the energy loss when traveling through the remaining half of the target.*

where $\vartheta_\gamma$ is the angle between the $z$-axis (the beam axis) and direction of propagation of the $\gamma$-ray in the rest frame of the nucleus emitting the $\gamma$-ray. The angular distribution coefficients $a_2^{E2}$ and $a_4^{E2}$, and the $\gamma - \gamma$ correlations coefficients $A_2$ and $A_4$ for a pure E2 $2 \rightarrow 0$ de-excitation are tabulated in [23]. The angular distribution is given in the center of mass frame, but evaluated in the laboratory frame of reference. The transformation between these frames is given by [24]

$$W_{LAB} = W_{CM} \cdot \frac{d\Omega_{LAB}}{d\Omega_{CM}} = W_{CM} \cdot \frac{1-\beta^2}{(1-\beta\cos\theta_\gamma)^2} \tag{4.7}$$

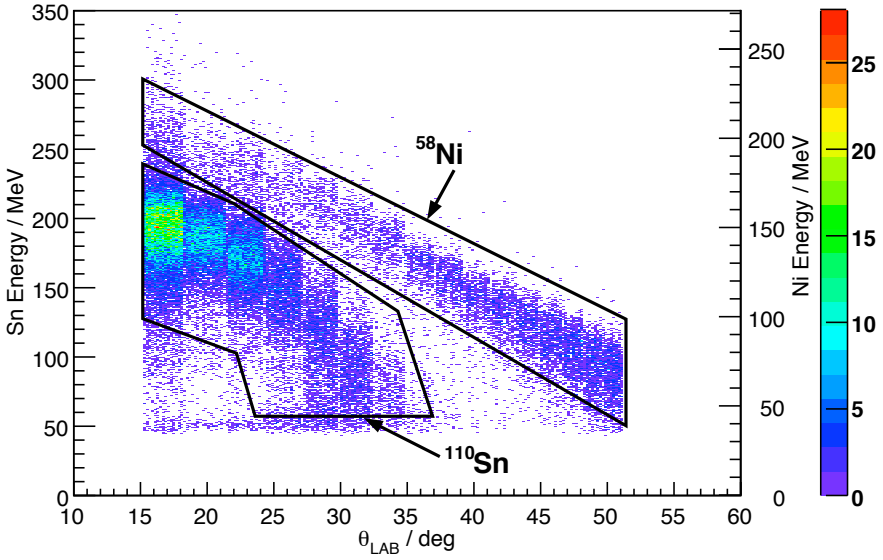


Figure 4.10: *Experimental particle energy, as calibrated using SRIM, versus detection angle in DSSSD. The data is from the X10 experiment.*

and the transformation of the detected $\gamma$-ray angle $\theta_\gamma$ and the rest frame angle $\vartheta_\gamma$ is given by [24]

$$\tan\left(\frac{1}{2}\vartheta_\gamma\right) = \sqrt{\frac{1+\beta}{1-\beta}}\tan\left(\frac{1}{2}\theta_\gamma\right) \tag{4.8}$$

In order to estimate the angular distribution ratio $\mathcal{W}$, a $\beta_{Sn} = 0.06$ and $\beta_{Ni} = 0.07$ was chosen together with $\eta = 131$ and $\xi_{Sn} = 0.91$ and $\xi_{Ni} = 0.75$. The resulting ratio is $\mathcal{W} = W_{Ni}/W_{Sn} = 0.999$. Typical angular distribution $W$ in both the laboratory frame of reference and the center of mass frame of reference for both projectile and target nuclei are given in Fig. 4.12

### 4.2.5 Particle Reconstruction

The missing particle in the 1p events is reconstructed. The reconstruction of the second particle from the detected particle follow a scheme:

- With a known energy and angle of the detected particle, it's center of mass scattering angle is also known.
- The center of mass scattering angles of two particles from the same physical event is equal. This means that the energy and angle, in the laboratory frame of reference, of the second particle can be calculated.

The ratio of the number of $\gamma$-rays in the Sn Coulomb excitation peak to the number of $\gamma$-rays in the Ni Coulomb excitation peak must remain consistent when adding the 1p and reconstructed events to the 2p events. This was verified for all three experiments, see Tab. 4.3

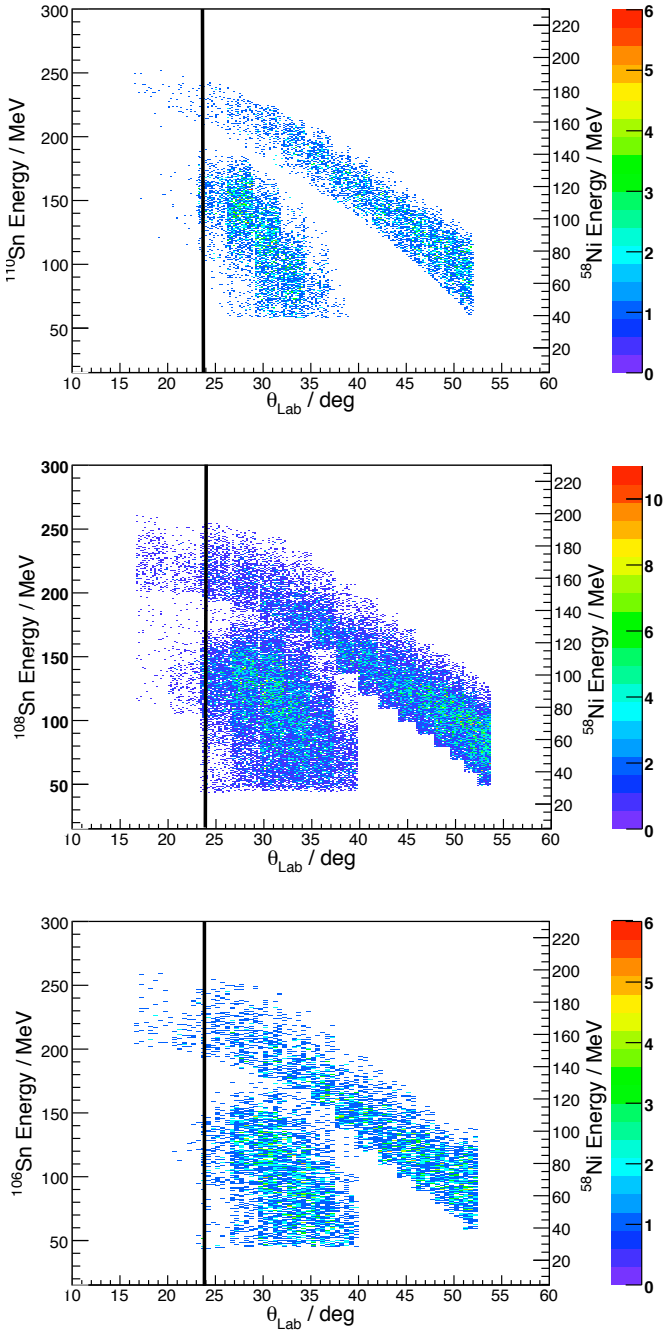


Figure 4.11: *Experimental particle data. Scattered particle energy, calibrated using SRIM, versus detection angle in DSSSD. The 2p coincidence is applied. (Top) X10 (Middle) X08 (Bottom) X06.*

### 4.2.6 Determination of isobaric Contamination

As mentioned in Sec. 3.1, the isobaric contamination comes from surface ionized In[1]. The contamination fraction of the beam was determined by repeatedly switching the RILIS laser

[1] $^{A}$In contaminant in a $^{A}$Sn beam

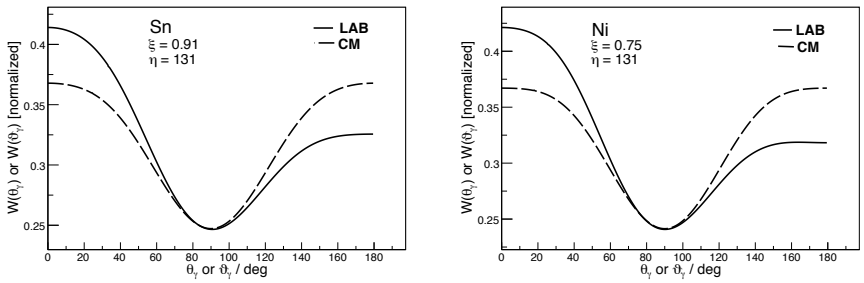


Figure 4.12: *$\gamma$-ray angular distributions calculated for $\beta_{Sn} = 0.06$ and $\beta_{Ni} = 0.07$. The plotted $W$ functions in the laboratory frame of reference (LAB) and center of mass frame of reference (CM) correspond to typical distributions.*

| Event Types | X10 $N_\gamma(Sn)/N_\gamma(Ni)$ | X08 $N_\gamma(Sn)/N_\gamma(Ni)$ | X06 $N_\gamma(Sn)/N_\gamma(Ni)$ |
|---|---|---|---|
| 2p | $2.41 \pm 0.37$ | $1.73 \pm 0.22$ | $0.69 \pm 0.15$ |
| 2p + 1p + Rec. | $2.44 \pm 0.19$ | $1.72 \pm 0.12$ | $0.64 \pm 0.09$ |

Table 4.3: *Adding the reconstructed (rec.) particles to the 1p event subset is consistent.*

on and off. When the laser was switched off, the beam consisted of In only. The laser status (on or off) was stored in the data stream for the X08/X06 experiments. For the X10 experiment none of the laser related data were stored in the offline data set. The quantity $\mathcal{R}$ used in Eq. 4.2 is

$$\mathcal{R} = \frac{N_{TOT}(Sn)}{N_{TOT}(Sn + In)} \tag{4.9}$$

where $N_{TOT}(Sn)$ denotes the total number of detected Sn ions, and $N_{TOT}(Sn + In)$ denotes the total number of detected beam ions.

**Laser On/Off Runs**

For the X08/X06 experiments the repetition frequency was dictated by the PS signal. This signal indicates the start of a new PS Booster cycle and comes every $14.4$ seconds. The RILIS is off for 14.4 seconds then on for 14.4 seconds. The primary target properties can be assumed not to fluctuate on this time scale. So the In component during one RILIS on period can be estimated from the previous RILIS off period. When running the laser in on/off mode, the scattered Sn fraction of the beam is

$$\mathcal{R}_{OnOff} = \frac{N_{ON} - N_{OFF}}{N_{ON}} \left( = 1 - \frac{N_{OFF}}{N_{ON}} \right) \tag{4.10}$$

Where $N_{ON}(N_{OFF})$ denotes the number of particles detected in the DSSSD during an on(off) period. The uncertainty $\Delta\mathcal{R}_{ON/OFF}$ can be estimated from $N_{ON}$ and $N_{OFF}$ using Poisson statistics.

**Extrapolation to Entire Experiment**

In order to get a measure on $\mathcal{R}$, a relationship between on/off runs and pure on runs must be established. Indium can be Coulomb excited by the target nuclei. The beam energy and detector setup is kept fixed making the excitation cross section constant. The Coulomb excitation yield from In during laser off periods in an on/off run is denoted $I_\gamma^{OFF}(In)$. This is proportional to $N_{OFF}$, with a constant of proportionality $\tilde{\sigma}$

$$I_\gamma^{OFF}(In) = N_{OFF} \cdot \tilde{\sigma} \tag{4.11}$$

If we denote the total intensity in the In Coulomb excitation peak with $I_\gamma^{TOT}(In)$ and the total number of detected In ionwith $N_{TOT}(In)$

$$I_\gamma^{TOT}(In) = N_{TOT}(In) \cdot \tilde{\sigma} \tag{4.12}$$

then using Eq. 4.11 gives

$$N_{TOT}(In) = \frac{I_\gamma^{TOT}(In)}{\tilde{\sigma}} = \frac{I_\gamma^{TOT}(In) \cdot N_{OFF}}{I_\gamma^{OFF}(In)} \tag{4.13}$$

The total number of detected particles is known, $N_{TOT}$, which means that a good estimate of $\mathcal{R}$ is given by

$$\mathcal{R} = 1 - \frac{N_{OFF}(In) \cdot I_\gamma^{TOT}(In)}{N_{TOT} \cdot I_\gamma^{OFF}(In)} \tag{4.14}$$

The uncertainty $\Delta\mathcal{R}$ can be estimated using Poisson statistics.

## 4.3 The Three Experiments

The $\gamma$-ray peak content coming from both target and projectile excitation was extracted, and the isobaric contamination was determined. Two types of integration methods were applied. Method one (Integral): The peaks were fitted with a linear/exponential + Gaussian function and then integrated. Method two (Discrete sum): A simple discrete sum of the bin content. The background was estimated from an average of the bin content to the left and right of the peak.

### 4.3.1 $^{110}$Sn

$\gamma$-ray spectra without any conditions in the data analysis can be viewed in Fig. 4.13. Peaks of interest and the origin of prominent peaks are marked. After applying prompt cuts, selecting only 2p events, reconstructing the 1p events, and a subsequent Doppler correction, the Coulomb excitation peaks are clearly visible, Fig. 4.14.

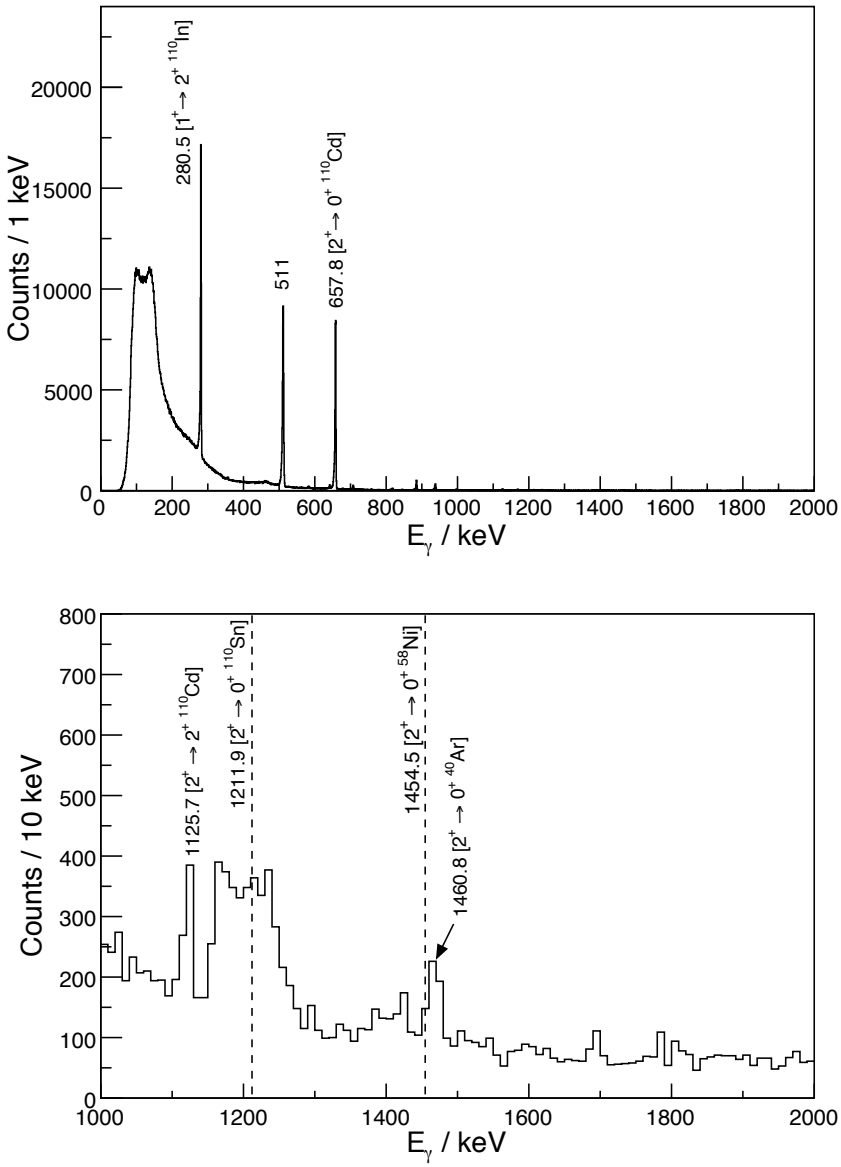


Figure 4.13: *(Top) Singles $\gamma$-ray spectrum from X10. The most prominent peaks are marked, showing energy, transition, and nucleus. (Bottom) Singles $\gamma$-ray spectrum zoomed in around the energy region of interest. Transitions in target and projectile are marked with dashed lines.*

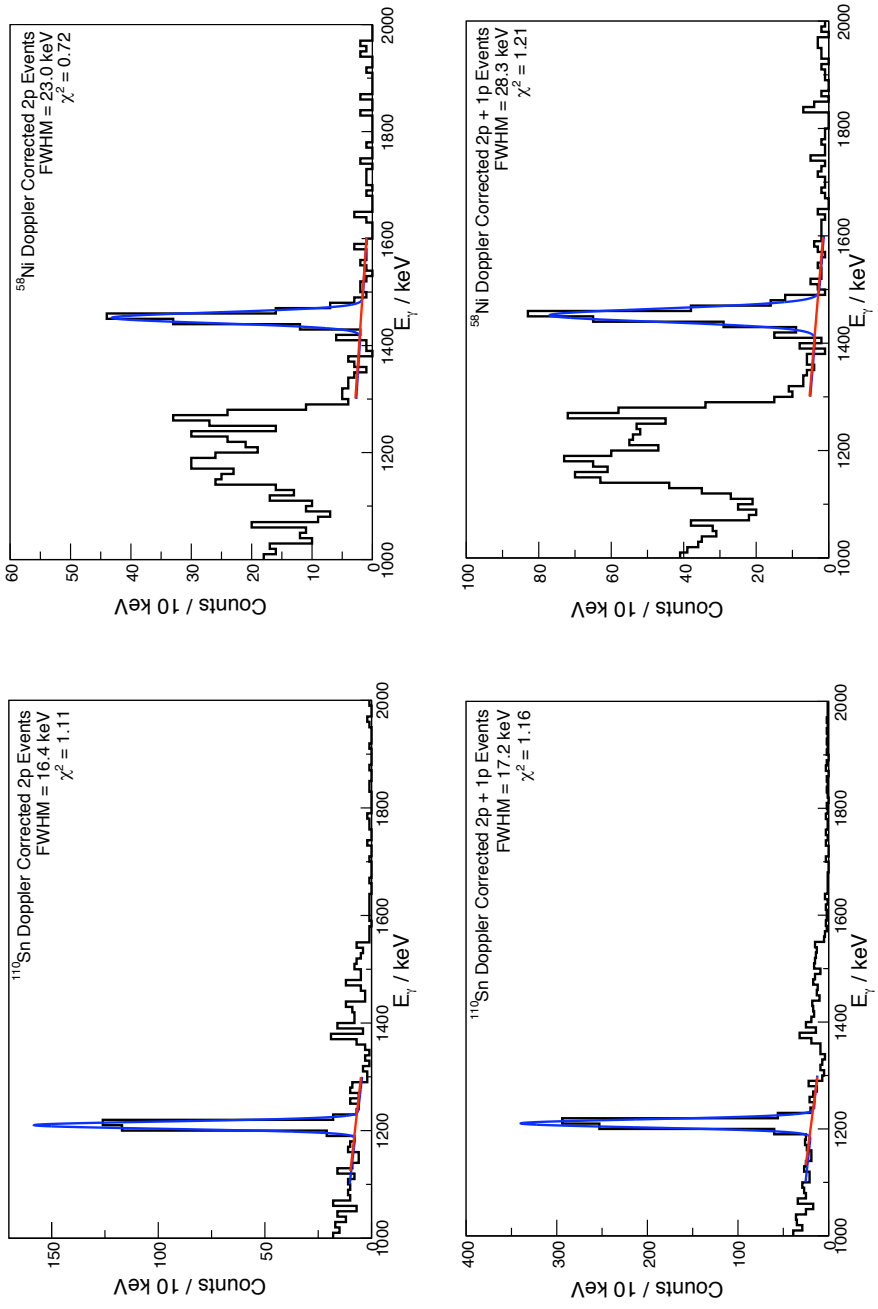


Figure 4.14: *Final $\gamma$-ray spectra from the X10 analysis. Type of spectrum and technical information regarding the fit can be found in the top right corner of each spectrum. (Top panels) The $\gamma$-ray spectra of 2p event type for both projectile and target. (Bottom panels) The $\gamma$-ray spectra of 2p+1p event type for both projectile and target. The increase in FWHM comes from adding Doppler corrected $\gamma$-rays from reconstructed particle events.*

| Nucleus | Transition | Energy / keV | Counts | Integration Method |
|---|---|---|---|---|
| $^{110}$Sn | $2_1^+ \rightarrow 0_{gs}^+$ | 1211.9 | $579.0 \pm 24.1$ | Discrete Sum |
| $^{110}$Sn | $2_1^+ \rightarrow 0_{gs}^+$ | 1211.9 | $588.1 \pm 24.3$ | Integral |
| $^{58}$Ni | $2_1^+ \rightarrow 0_{gs}^+$ | 1454.5 | $237.5 \pm 15.4$ | Discrete Sum |
| $^{58}$Ni | $2_1^+ \rightarrow 0_{gs}^+$ | 1454.5 | $222.8 \pm 14.9$ | Integral |

Table 4.4: *The Coulomb excitation $\gamma$-ray yields extracted from the X10 data set.*

The Coulomb excitation peaks of interest and the corresponding $\gamma$-ray yields are summarized in Tab. 4.4.

**Isobaric Contamination**

The isobaric contamination was determined during the experiment by measuring the beam current with a Faraday cup both when the RILIS laser was on and off. This currents gave a measure of the isobaric contamination. This procedure was repeated 10 times during the experiment in order to detect possible variations in the beam composition. The ratio $\mathcal{R}$ was

$$\mathcal{R} = 0.900 \pm 0.014 \tag{4.15}$$

This is consistent with the online yield measurements at the primary target, see Paper I.

### 4.3.2 $^{108}$Sn

$\gamma$-ray spectra without any conditions in the data analysis can be viewed in Fig. 4.15. Peaks of interest and the origin of prominent peaks are marked. After applying prompt cuts, selecting only 2p events, reconstructing the 1p events, and a subsequent Doppler correction, the Coulomb excitation peaks are clearly visible, Fig. 4.16.

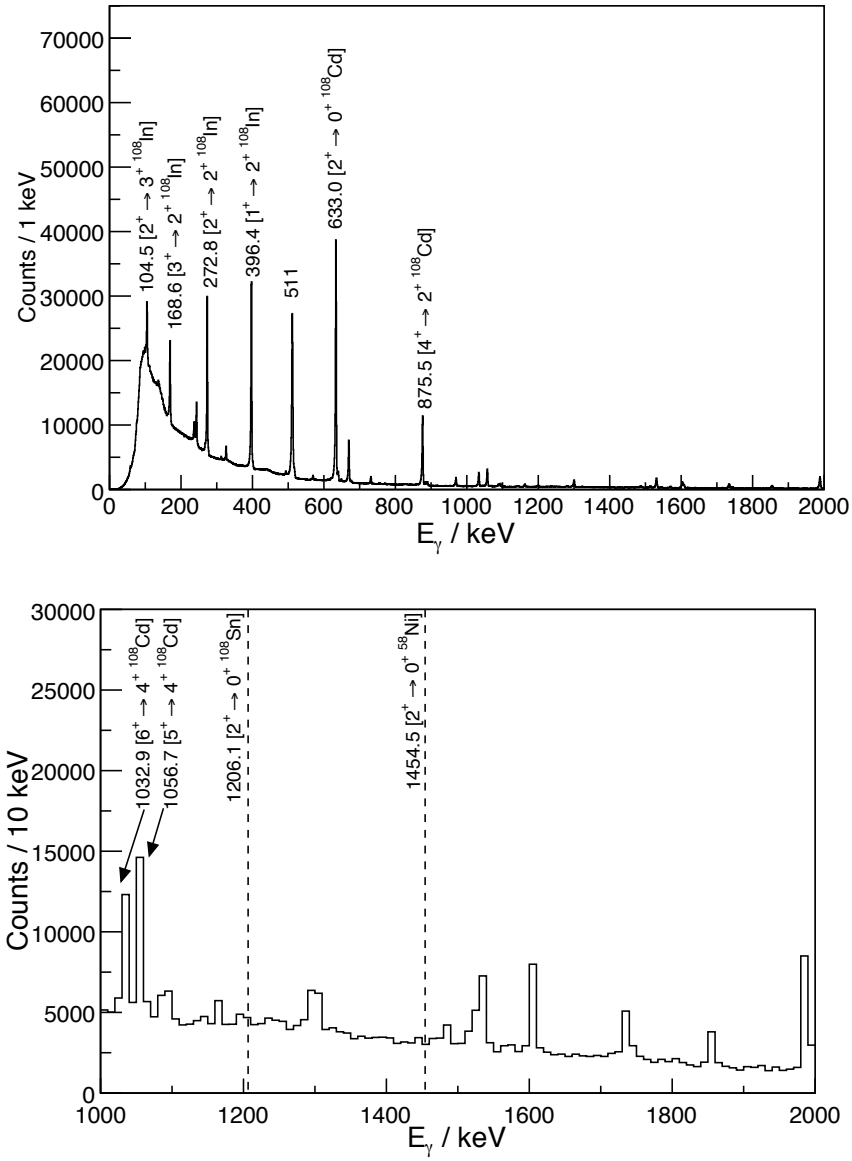


Figure 4.15: *(Top) Singles $\gamma$-ray spectrum from X08. The most prominent peaks are marked, showing energy, transition, and nucleus. (Bottom) Singles $\gamma$-ray spectrum zoomed in around the energy region of interest. Transitions in target and projectile are marked with dashed lines.*

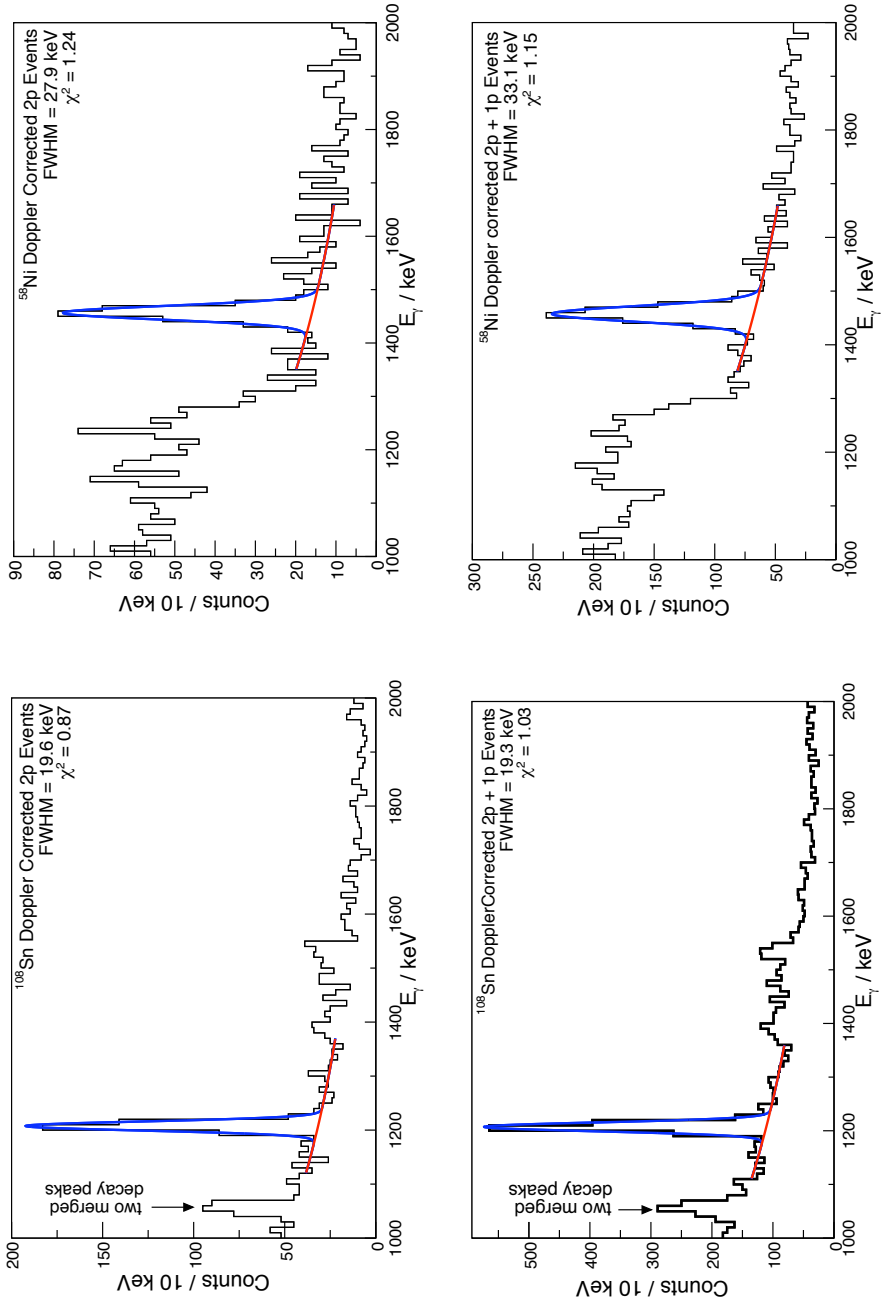


Figure 4.16: *Final $\gamma$-ray spectra from the X08 analysis. Type of spectrum and technical information regarding the fit can be found in the top right corner of each spectrum. (Top panels) The $\gamma$-ray spectra of 2p event type for both projectile and target. (Bottom panels) The $\gamma$-ray spectra of 2p+1p event type for both projectile and target. The increase in FWHM comes from adding Doppler corrected $\gamma$-rays from reconstructed particle events.*

| Nucleus | Transition | Energy / keV | Counts | Integration Method |
|---|---|---|---|---|
| $^{108}$Sn | $2_1^+ \rightarrow 0_{gs}^+$ | 1206.1 | $994.0.0 \pm 38.3$ | Discrete Sum |
| $^{108}$Sn | $2_1^+ \rightarrow 0_{gs}^+$ | 1206.1 | $1034.7 \pm 60.7$ | Integral |
| $^{58}$Ni | $2_1^+ \rightarrow 0_{gs}^+$ | 1454.5 | $576.5 \pm 33.5$ | Discrete Sum |
| $^{58}$Ni | $2_1^+ \rightarrow 0_{gs}^+$ | 1454.5 | $589.5 \pm 33.7$ | Integral |

Table 4.5: *The Coulomb excitation $\gamma$-ray yields extracted from the X08 data set.*

**Coulomb Excitation Yields**

The Coulomb excitation peaks of interest and the corresponding $\gamma$-ray yields are summarized in Tab. 4.5.

**Isobaric Contamination**

Using Eqs. 4.10 and 4.14 the $^{108}$Sn fraction in the beam during on/off runs could be determined

$$\mathcal{R}_{OnOff} = 0.597 \pm 0.007 \tag{4.16}$$

The extrapolation to the full experiment utilized the $^{108}$In Coulomb excitation transition at 237 keV. The sum of Coulomb excitation $\gamma$-rays in $^{108}$In during laser off was determined to $I_\gamma = 262.7 \pm 29.5$. While the corresponding quantity collected over the whole experiment was determined to $I_\gamma = 1526.7 \pm 100.3$. The number of scattered particles into the DSSSD during laser off was $N_{OFF} = 15563$ and in total during the whole experiment $N_{TOT} = 220968$. This leads to an extrapolated Sn fraction of

$$\mathcal{R} = 0.590 \pm 0.027 \tag{4.17}$$

**Correlation Between Laser Power and Isobaric Contamination**

A measure of the laser power was continuously stored in the data stream, as well as the number of scattered particles into the DSSSD. During laser on/off periods, the number of scattered Sn particles, $N_{Sn}$, should be related to the laser power, $L_P$, applied in the primary target cavity. $N_{Sn}$ was estimated from the laser on/off runs

$$N_{Sn}^{ON} = N_{Sn+In}^{ON} - N_{In}^{OFF} \tag{4.18}$$

under the assumption $N_{In}^{ON} = N_{In}^{OFF}$ for consecutive on and off periods. In order to minimize the influence of random fluctuations, the quantities were averaged over a time period $T$. The sample correlation coefficient[2], $\mathcal{C}(\langle N_{Sn}\rangle_T, \langle L_P\rangle_T)$, is the standard Pearson product-moment correlation coefficient

$$\mathcal{C}(\langle N_{Sn}\rangle_T, \langle L_P\rangle_T) = \frac{n\sum_i^n x_i y_i - \sum_i^n x_i \sum_i^n y_i}{\sqrt{n\sum_i^n x_i^2 - (\sum_i^n x_i)^2}\sqrt{n\sum_i^n y_i^2 - (\sum_i^n y_i)^2}}, \quad x_i = \langle N_{Sn}\rangle_{T,i}, \quad y_i = \langle L_P\rangle_{T,i} \tag{4.19}$$

The time interval $T$ was dictated by the correlation coefficient, Tab. 4.6 The relation between

[2]Correlation does not imply causality, which in this case can be inferred from the technical and physical knowledge of the RILIS.

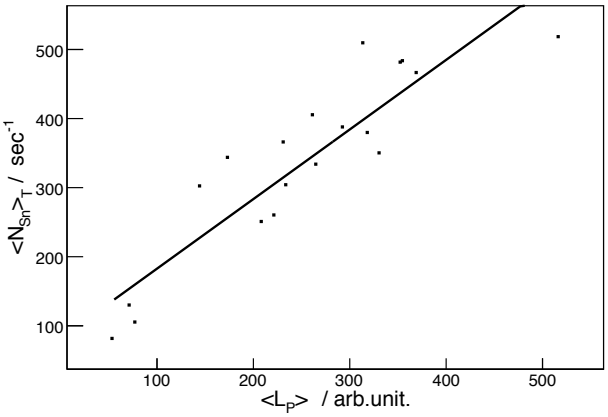


Figure 4.17: *Time-averaged values of scattered $^{108}$Sn versus laser power*

| T (min) | $\mathcal{C}(\langle N_{Sn}\rangle_T, \langle L_P\rangle_T)$ |
|---|---|
| 10 | 0.86 |
| 20 | 0.87 |
| 30 | 0.85 |
| **40** | **0.90** |
| 50 | 0.86 |

Table 4.6: *The correlation coefficient $\mathcal{C}$ for various time intervals $T$. The optimal $T$ is marked with bold font.*

$\langle N_{Sn}\rangle_{40}$ and $\langle L_P\rangle_{40}$ is plotted in Fig. 4.17. For completeness, the sample correlation coefficient between the contaminant and the laser power, $\mathcal{C}(\langle N_{In}\rangle_T, \langle L_P\rangle_T)$, was found to be 0.38. The value is low since there should be no correlation. The correlation between the laser power and the number of Sn particles scattered into the DSSSD gives an alternative measure on $\mathcal{R}$. This we denote $\mathcal{R}^{\mathcal{C}}$,

$$\mathcal{R}^{\mathcal{C}} = 0.58 \pm 0.01 \tag{4.20}$$

### 4.3.3 $^{106}$Sn

The Coulomb excitation peaks of interest and the corresponding $\gamma$-ray yields are summarized in Tab. 4.7.

| Nucleus | Transition | Energy / keV | Counts | Integration Method |
|---|---|---|---|---|
| $^{106}$Sn | $2_1^+ \rightarrow 0_{gs}^+$ | 1206 | $132.5 \pm 14.9$ | Discrete Sum |
| $^{106}$Sn | $2_1^+ \rightarrow 0_{gs}^+$ | 1206 | $139.8 \pm 19.9$ | Integral |
| $^{58}$Ni | $2_1^+ \rightarrow 0_{gs}^+$ | 1454.5 | $206.5 \pm 16.1$ | Discrete Sum |
| $^{58}$Ni | $2_1^+ \rightarrow 0_{gs}^+$ | 1454.5 | $204.5 \pm 18.8$ | Integral |

Table 4.7: *The Coulomb excitation $\gamma$-ray yields extracted from the X06 data set.*

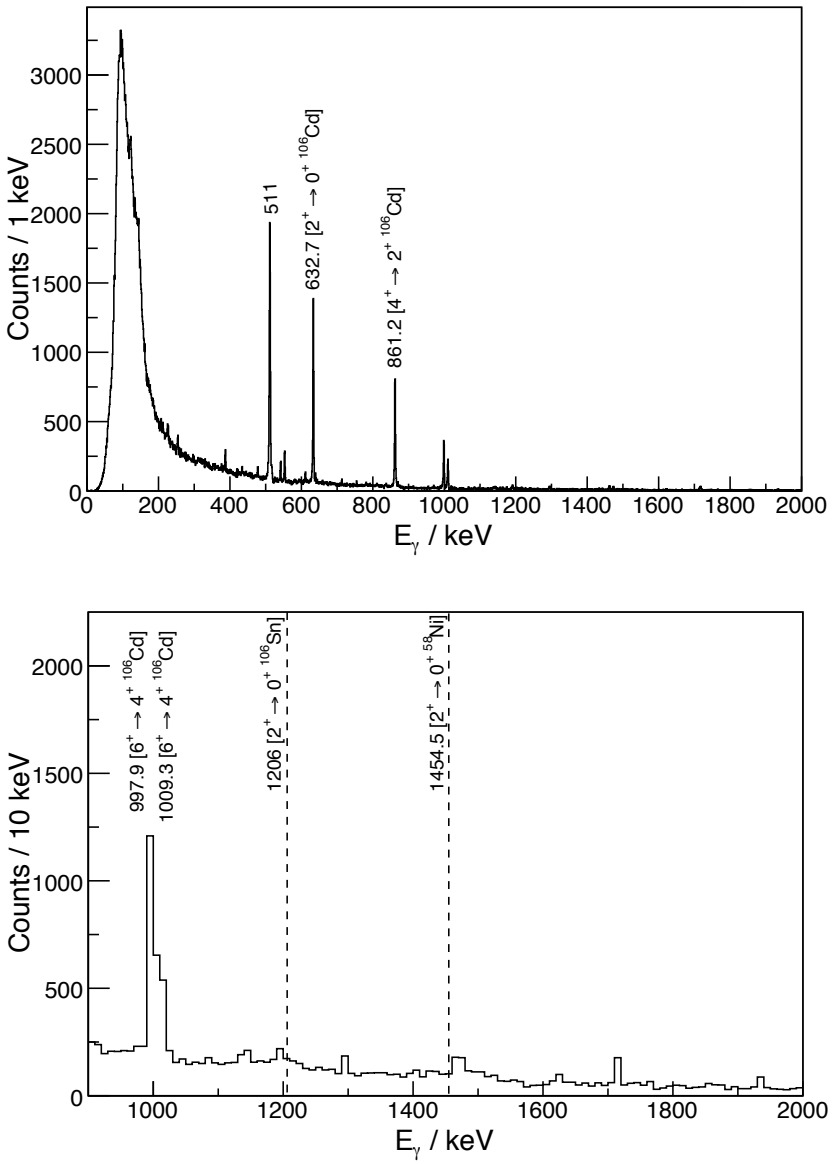


Figure 4.18: *(Top) Singles $\gamma$-ray spectrum from X06. The most prominent peaks are marked, showing energy, transition, and nucleus. (Bottom) Singles $\gamma$-ray spectrum zoomed in around the energy region of interest. Transitions in target and projectile are marked with dashed lines.*

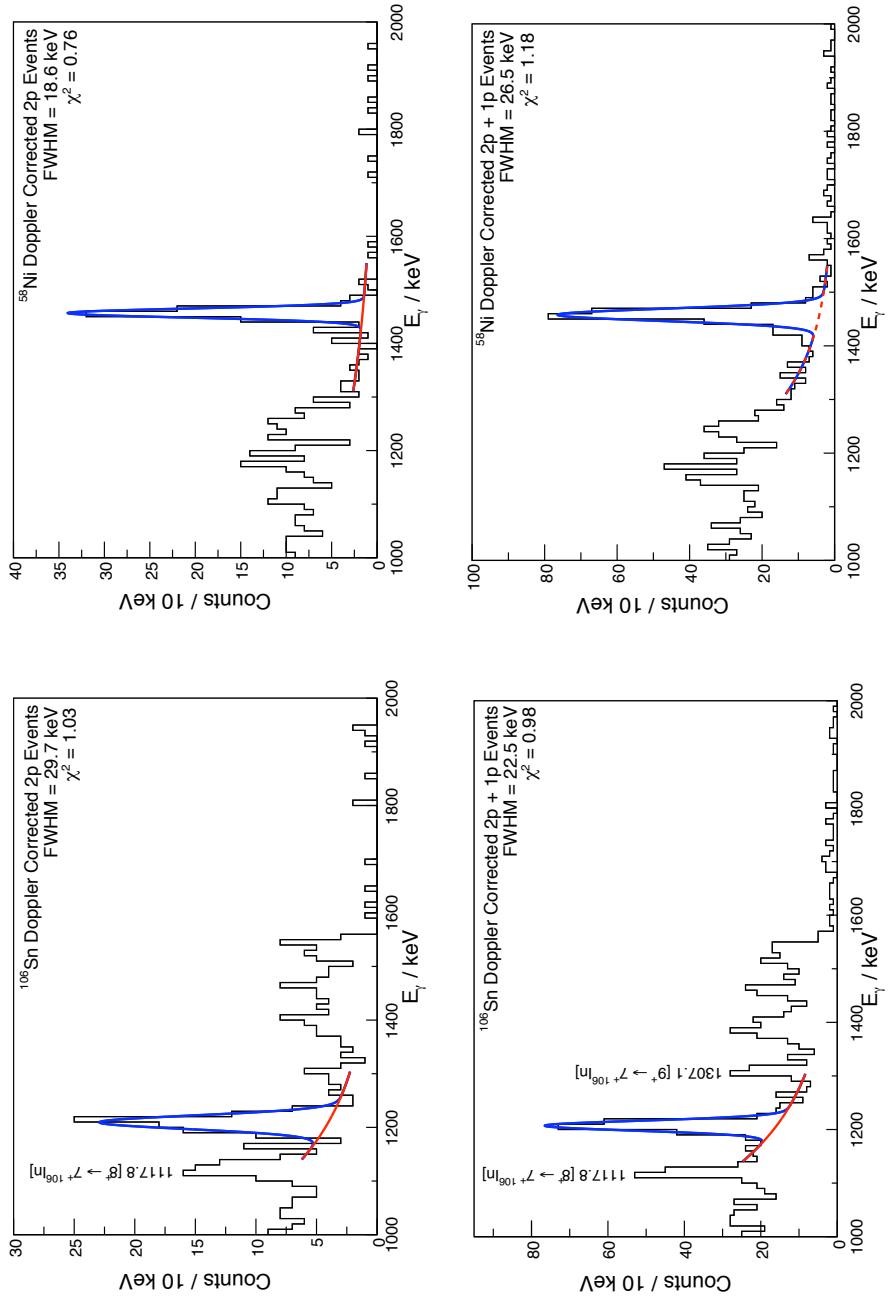


Figure 4.19: *Final $\gamma$-ray spectra from the X06 analysis. Type of spectrum and technical information regarding the fit can be found in the top right corner of each spectrum. (Top panels) The $\gamma$-ray spectra of 2p event type for both projectile and target. (Bottom panels) The $\gamma$-ray spectra of 2p+1p event type for both projectile and target. The increase in FWHM comes from adding Doppler corrected $\gamma$-rays from reconstructed particle events.*

**Isobaric Contamination**

With the laser status (on or off) in the data stream it was possible to determine the isobaric contamination in the offline analysis. Using Eqs. 4.10 and 4.14 the $^{106}$Sn fraction in the beam during on/off runs could be determined

$$\mathcal{R}_{OnOff} = 0.235 \pm 0.020 \tag{4.21}$$

The extrapolation to the full experiment utilized the $^{106}$In Coulomb excitation transitions at $368$ keV, $147$ keV, and $121$ keV [47]. A random background subtraction was performed in order to improve the peak to background and remove the decay component[3] in the 121 keV and 147 kev peaks. The sum of Coulomb excitation $\gamma$-rays in $^{108}$In during laser off was determined to $I_\gamma = 274.7 \pm 29.2$. While the corresponding quantity collected over the whole experiment was determined to $I_\gamma = 1718.7 \pm 101.3$. The number of scattered particles into the DSSSD during laser off was $N_{OFF} = 3606$ and in total during the whole experiment $N_{TOT} = 31872$. This leads to an extrapolated Sn fraction of

$$\mathcal{R} = 0.292 \pm 0.042 \tag{4.22}$$

This value in comparison with the $\mathcal{R}_{OnOff}$ value reflects the importance of doing an extrapolation to the full experiment.

It was not possible to correlate the laser power with the number of scattered $^{106}$Sn particles. This can indicate that the position of the laser beam has drifted during the experiment. The laser power is only a measure of the injected ionization effect, not the real ionization effect.

## 4.4 Coulomb Excitation Analysis with GOSIA2

GOSIA2[4] is a computer code specially developed for Coulomb excitation experiments using RIBs. It can calculate amongst other things Coulomb excitation probabilities $P(\theta)$ and determine transition probabilities from experimental $\gamma$-ray yields.

### 4.4.1 Numerical Method

The aim of the calculation is to fit the unknown reduced transition matrix elements $\mathcal{M}_{if}$, where $B(\mathcal{O}\lambda) \propto |\mathcal{M}_{if}|^2$, to reproduce the experimental $\gamma$-ray yields. The program carries out the $(E, \theta, \phi)$ integration of the differential cross section and can take into account internal conversion coefficients, $\gamma$-ray transition branching ratios, and mixing ratios $\delta$.

The Schrödinger equation to solve is:

$$i\hbar\frac{\partial}{\partial t}|\psi(\vec{r},t)\rangle = (\mathcal{H}_0 + V(\vec{r},t))|\psi(\vec{r},t)\rangle \tag{4.23}$$

[3] coming from $^{108}$Sn $\rightarrow$ $^{108}$In decay.

[4] GOSIA2 and GOSIA are identical regarding handling of Coulomb excitation theory etc. The only difference between the two codes is how the normalization is done.

where $V(\vec{r},t)$ is electromagnetic monopole-multipole interaction between the projectile and target, and $|\psi(\vec{r},t)\rangle$ is the state vector of the nucleus that is excited. For example, the target is excited by the multipole field of the projectile and vice versa. The monopole-monopole interaction determines the time-dependent trajectory of particles. When the nuclei are infinitely separated the nucleus to be excited is described by a free-nucleus Hamiltonian $\mathcal{H}_0$ defined from

$$\mathcal{H}_0|\Phi_n\rangle = E_n|\Phi_n\rangle \tag{4.24}$$

where $|\Phi_n\rangle$ is the free-nucleus wave function. The index $n$ indicates which internal nuclear state the nucleus is in. The time-dependent nuclear state vector can be expressed in the free-nucleus state vectors if the time-dependent expansion coefficients[5] $a_n(t)$ are introduced

$$\psi(\vec{r},t)\rangle = \sum_n a_n(t)|\Phi_n(\vec{r})\rangle e^{-iE_nt/\hbar} \tag{4.25}$$

which means that Eq. 4.23 can be written

$$ih\sum_n \frac{da_n(t)}{dt}|\Phi_n(\vec{r})\rangle e^{-iE_nt/\hbar} = \sum a_n(t)V(t)|\Phi(\vec{r})e^{-iE_nt/\hbar} \tag{4.26}$$

The free nucleus wave functions are orthonormal, $\langle\Phi_k|\Phi_n\rangle = \delta_{kn}$, meaning that

$$\frac{da_k(t)}{dt} = -\frac{i}{\hbar}\sum_n a_n(t)\langle\Phi_k|V(t)|\Phi_n\rangle e^{-it(E_k-E_n)/\hbar} \tag{4.27}$$

Following the standard theory of multipole expansion, the interaction potential $V(t)$ can be written

$$V(t) = \sum_{\lambda=1}^{\infty}\sum_{\mu=-\lambda}^{\lambda}\frac{4\pi Ze}{2\lambda+1}(-1)^{-\mu}S_{\lambda\mu}(t)\mathcal{M}(\lambda,-\mu) \tag{4.28}$$

where the $S_\lambda$ now contains the motion of the potential and the multipole components $\mathcal{M}(\lambda,\mu)$ for the electric case is given by Eq. 2.42. Using the multipole expansion, Eq. 4.27 can be written

$$\frac{da_k(t)}{dt} = -i\frac{4\pi Ze}{\hbar}\sum_n a_n(t)e^{it/\hbar(E_k-E_n)}\sum_{\lambda\mu}(-1)^{\mu}S_{\lambda\mu}(t)\langle\Phi_k|\mathcal{M}(\lambda,-\mu)|\Phi_n\rangle \tag{4.29}$$

According to Ref. [23] the time-dependent $S_{\lambda\mu}$ functions are convenient to express in a coordinate system, for which in the center of mass frame, the $z$-axis is along the symmetry axis of the incoming particle trajectory and the $y$-axis is in the trajectory plane such that the incoming particle velocity component $v_y > 0$. The $x$-axis is defined so that the coordinate system is right-handed and Cartesian. The new parameters to describe the trajectories are $\omega$ and $\varepsilon$. The parameter $\varepsilon$ is the orbit eccentricity, and time $t$ is now parameterized by $\omega$

$$\varepsilon = \frac{1}{\sin\frac{\theta_{cm}}{2}}, \quad t = \frac{b}{v_i}(\varepsilon\sinh\omega + \omega) \tag{4.30}$$

and the transformation to a Cartesian system is given by

$$x = 0, \quad y = b(\varepsilon^2-1)^{1/2}\sinh\omega, \quad z = b(\cosh\omega+\varepsilon), \quad r = b(\varepsilon\cosh\omega+1) \tag{4.31}$$

[5] These are the same expansion coefficients related to $P$ in Eq. 2.38

The $S_{\lambda\mu}(t)$ functions expressed in this system are called collision functions $Q_{\lambda\mu}(\varepsilon,\omega)$. The collision functions that GOSIA2 use are listed in Ref. [26]. Equation 4.29 expressed in the $\varepsilon,\omega$ system are given by

$$\frac{da_k}{d\omega} = -i\sum_{\lambda\mu n} Q_{\lambda\mu}(\varepsilon,\omega)\zeta_{kn}^{(\lambda\mu)}\langle\Phi_k||\mathcal{M}(\lambda)||\Phi_n\rangle \exp(i\xi_{kn}(\varepsilon\sinh\omega+\omega))a_n(\omega) \tag{4.32}$$

where $\zeta_{kn}^{(\lambda\mu)}$ are angular momentum coupling coefficients given in Ref. [26]. The collision functions for electric and magnetic excitations are different. However, no explicit distinction is made here. Equation 4.32 completely defines the excitation process. The excitation probability can be obtained by integrating this differential equation. Some further approximations are implemented in GOSIA2. Equation 4.32 can be written as

$$\frac{da_k}{d\omega} = \sum_{lmn}\zeta_{kn}^{(lm)}M_{kn}^{(1)}f_{lm}(\omega)a_n(\omega) \tag{4.33}$$

where $f_{lm}(\omega) = -iQ_{lm}(\omega)\exp[i(\varepsilon\sinh\omega+\omega)]$, and $M_{kn}^{(1)} = \langle k||\mathcal{M}(l)||n\rangle$. Only couplings between magnetic substates differing with $\delta m = 0,1$ are made since the strength of the interaction rapidly decrease with $\delta m$ [23, 26], and magnetic excitations are neglected. The only electric multipolarities allowed are $\lambda = 1-6$. The main GOSIA2 code approximation lies in the treatment of the collision parameter $f_{lm}(\omega)$. The $\omega$-dependence is removed, and the $f_{lm}(\omega)$ function is replaced with a constant effective interaction strength $q_{lm}$, extended over a finite range $I_\omega$. The effective strength parameter $q$ depend on $\xi$, $\Delta m$, and weakly on $\zeta$. The $q$ is approximated based on exact solutions of the excitation amplitudes for a two-level system at discrete $\xi$ points. Further details are found in Ref. [26].

During the minimization procedure, the Coulomb excitation cross section is integrated over the scattering angles and target thickness[6] only once. The integrated yield

$$Y(i\to f) = \int_{E_{p,min}}^{E_{p,max}} \frac{1}{dE_p/dx}\,dE_p \int_{\theta_{p,min}}^{\theta_{p,max}} \sin(\theta_p)\int \frac{d^2\sigma(i\to f)}{d\Omega_\gamma d\Omega_p}d\phi_p d\theta_p \tag{4.34}$$

is given in a unit of $(mb/srad)\cdot(mg/cm^2)$. The transition matrix elements are fitted to reproduce the experimental yields for a constant particle energy and angle. Once the minimization routine has converged ($\chi^2$ minimization with tolerance defined by the user) the full integration is done once again.

### 4.4.2 Calculation of the $B(E2)$ Values

The $B(E2)$ value for the $^{58}$Ni target was taken from the BNL Evaluated Nuclear Structure Data File (ENSDF)[7].

$$\text{For } ^{58}\text{Ni}: B(E2; 0_{\text{gs}}\to 2_1^+) = 0.0705(18)\ \text{e}^2\text{b}^2 \tag{4.35}$$

The static quadrupole moment of the first excited $2^+$ state in the $^{106,108,110}$Sn isotopes was set to 0 eb. This is in line with the measurements on the stable even mass Sn-isotopes [48].

[6] The integration is done over projectile energy. Energy loss parameters are supplied to GOSIA by the user.
[7] Evaluated 26-sep 2006

**Input**

The following must be given as input [26]

- The $\gamma$-ray yields $I_\gamma$ for the transition i both target and projectile.
- The known $B(E2)$ value from the target transition.
- The energy and scattering angle of the projectile to be used in evaluation of the point yields. For instance the energy in center of target and the angle halfway between minimum and maximum detection.
- The positions of the 24 Ge-detectors.
- Internal conversion coefficients. The ones used in this licentiate thesis were taken from [49]
- Energy loss parameters for $^{106,108,110}$Sn in $^{58}$Ni, calculated by SRIM [46]
- Projectile energy integration limits.
- Projectile scattering angle integration limits. Min: $\theta_{2p}$ Max: $\theta_{LAB}^{max}$
- Experimental level schemes for target and projectile (from ENSDF), see Fig. 4.2

The numerical interpolation of targets thicker than 1 mg/cm$^2$ can yield inconsistent results [50]. The target should be split into parts of 1 mg/cm$^2$ thickness each. The integration routine must be checked for consistency by changing the number of integration points. The minimization routine converged for all three calculations.

# Chapter 5

# Experimental Results

The reduced transition probabilities $B(E2; 0^+_{\rm gs} \rightarrow 2^+_1)$ in the neutron-deficient $^{106,108,110}$Sn isotopes were extracted using sub-barrier Coulomb excitation to the first excited $2^+$ state in both the projectile Sn isotopes and the target $^{58}$Ni. The experiments were performed at the RIB facility REX-ISOLDE located at CERN. The $B(E2)$ values were calculated using the coupled-channels computer code GOSIA2 with input from the discrete value $\gamma$-ray yields of Tabs. 4.4, 4.5, and 4.7. The $B(E2)$ value for the $^{58}$Ni target was taken from the BNL Evaluated Nuclear Structure Data File (ENSDF).

$$\text{For } ^{58}\text{Ni} : B(E2; 0_{\rm gs} \rightarrow 2^+_1) = 0.0705(18)\ \text{e}^2\text{b}^2 \tag{5.1}$$

The static quadrupole moment of the $2^+_1$ state in $^{106,108,110}$Sn was set to 0 eb in the analysis. This is in line with the measured values in the stable even-mass Sn isotopes [48]. The following results were obtained:

- In $^{110}$Sn: $B(E2; 0^+_{gs} \rightarrow 2^+_1) = (0.221 \pm 0.022)\ \text{e}^2\text{b}^2$ [1]
- In $^{108}$Sn: $B(E2; 0^+_{gs} \rightarrow 2^+) = (0.222 \pm 0.019)\ \text{e}^2\text{b}^2$
- In $^{106}$Sn: $B(E2; 0^+_{gs} \rightarrow 2^+) = (0.195 \pm 0.039)\ \text{e}^2\text{b}^2$

The above listed values are plotted in Figs. 5.1 and 5.1 together with adopted values for heavier Sn-isotopes and two theoretical calculations [1]. See Ch. 6 for details regarding the theoretical calculations.

[1] This is the result using GOSIA2. Using CLX gives $0.220 \pm 0.022$ which is the value stated in paper I of this licentiate thesis.

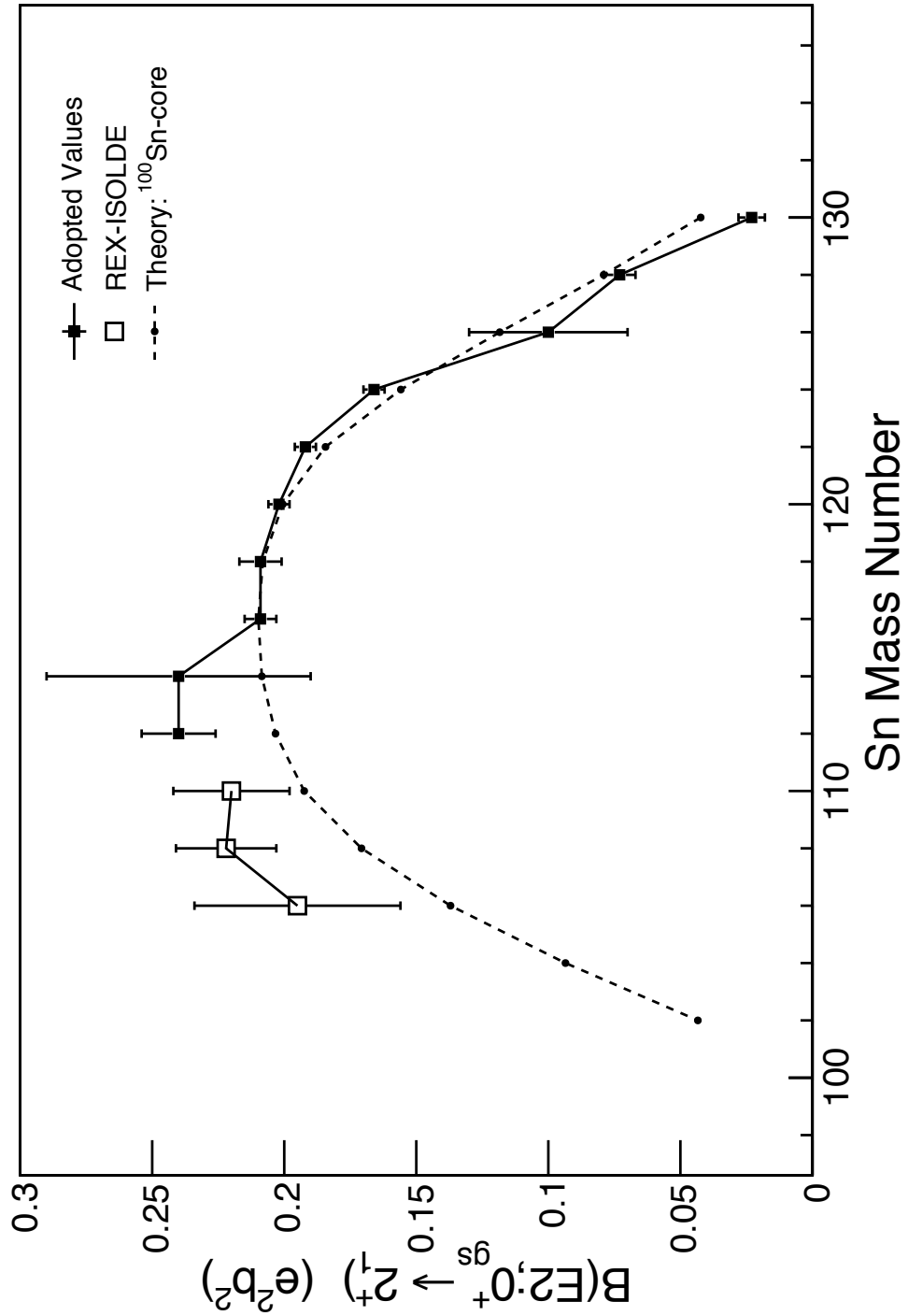


Figure 5.1: *Known $B(E2;\uparrow)$ values, given in $e^2b^2$, for the even-mass Sn-isotopes. The hollow squares indicate the experimental values measured at REX-ISOLDE that are presented in this licentiate thesis. The filled squares represent adopted values from [1]. The dashed line represents the results of shell-model calculations using $^{100}$Sn as an inert core. See Ch. 6 for details.*

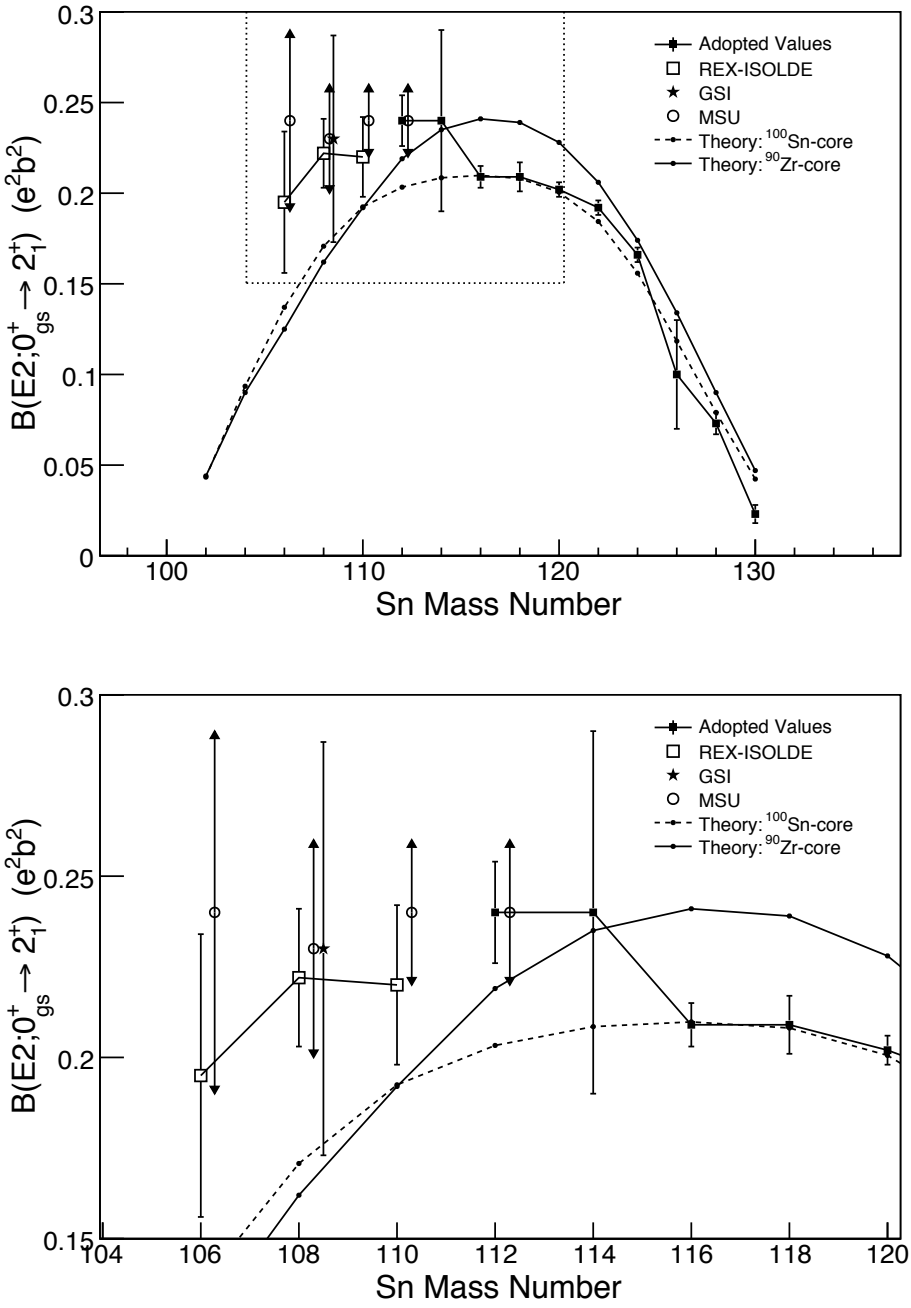


Figure 5.2: *Known $B(E2;\uparrow)$ values, given in $e^2b^2$, for the even-mass Sn-isotopes. The hollow squares indicate the experimental values measured at REX-ISOLDE that are presented in this licentiate thesis. The filled squares represent adopted values from [1]. The dashed line represents results of shell-model calculations using $^{100}$Sn as an inert core. The solid line represents the results of shell-model calculations using $^{90}$Zr as an inert core.*

# Chapter 6

# Discussion

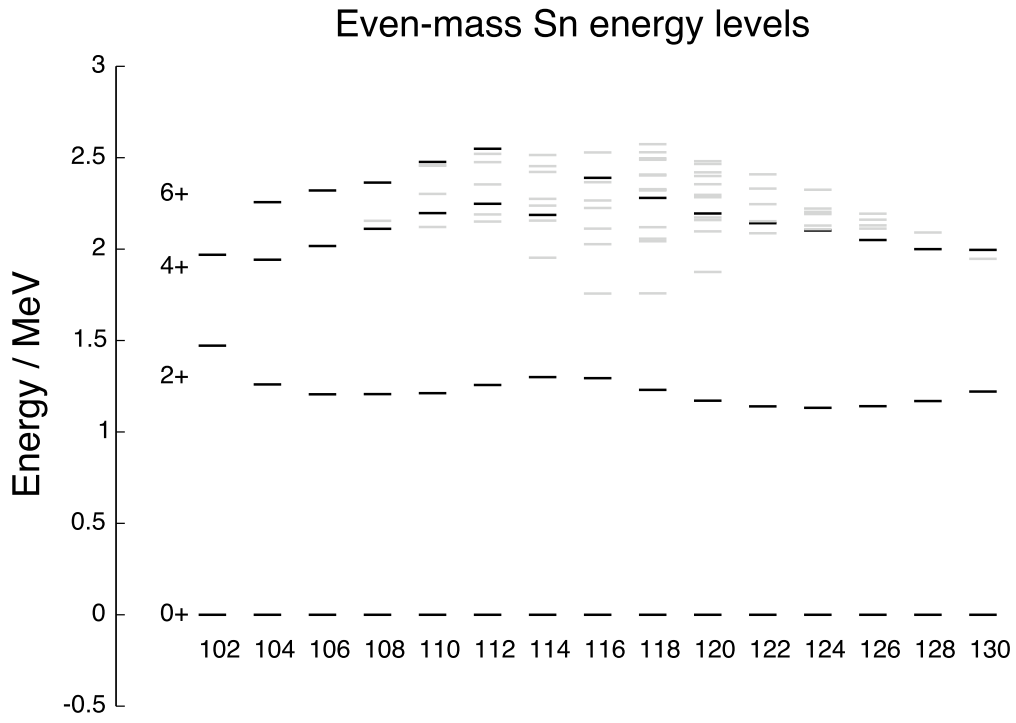


Figure 6.1: *Experimental low lying energy levels in the even-mass Sn isotopes* $^{102-130}$*Sn. The black lines represent, in order, the position of the first* $2^+, 4^+$*, and* $6^+$ *where present. Remaining low-lying levels are gray-shaded and included for completeness.*

The nearly constant energy spacings between the first $2^+$ state and $0^+$ ground state in $^{102-130}$Sn, see Fig. 6.1, are explained within the generalized seniority model [51]. In general, with the addition or removal of protons, the seniority model would no longer be valid for the present case. Instead the onset of deformation driving forces start to dominate which can drastically change the level structure [52, 53].

Excited states in $^{132}$Sn have been known since long via $\beta^-$-decay studies of $^{132}$In produced in fission [54]. The $2_1^+$ state in $^{132}$Sn is located at 4.04 MeV. The high excitation energy implies a shell closure at $N = 82$. This is strengthened by the experimental and theoretical $B(E2)$ values in the vicinity of $^{132}$Sn, see Fig. 5.1.

The $B(E2)$ value between the $2_1^+$ state and the ground state in $^{114}$Sn was re-measured recently with sub-barrier Coulomb excitation at GSI. It remains shifted to a higher value while the uncertainty was reduced to a level comparable with the other stable Sn isotopes [55]. The shift in the adopted $B(E2)$ values when moving from $^{114}$Sn to $^{116}$Sn could indicate a sub-shell closure at neutron number $N = 64$. However, a shell-closure is traditionally detected in nucleon separation energy systematics. In Fig. 6.2 the two-neutron separation energy is plotted for the even-mass Sn isotopes. The changes in the two-neutron separation energy is closely related with pairing and the superfluid phase in the nuclear condensate [56]. Without pairing, equivalently destroyed seniority, the two-neutron separation energy outside the closed $^{100}$Sn core would follow a step function with cusps at neutron numbers corresponding to the single particle orbits. The sub-shell closure indicated in the difference between the experimental $B(E2)$ values for $^{114}$Sn and $^{116}$Sn is not found in Fig. 6.2. The trend of

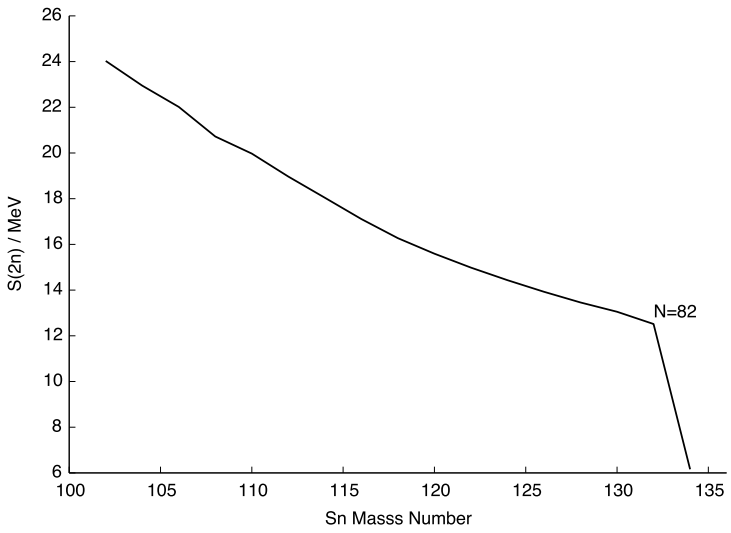


Figure 6.2: *Experimental two-neutron separation energies $S(2n)$ for the even-mass Sn isotopes [44]. A sharp drop is observed after $N = 82$, indicating that a shell-closure is formed at this neutron number*

increasing energies of the first $2^+$ state and the first $4^+$ state towards $^{100}$Sn [57] indicate a good shell closure at $N = Z = 50$. However, the experimental $B(E2)$ values , see Fig. 5.1, indicate a larger than predicted collectivity in the neutron deficient Sn isotopes, which in turn points towards a weakening of the shell closure. The currently available experimental $B(E2; 0_{gs} \rightarrow 2_1^+)$ values in $^{106,108,110}$Sn [1, 58, 59] are consistent with each other. Furthermore, they are not reproduced in any shell-model calculation. A relativistic quasi-particle random phase calculation[60] does reproduce the trend of increasing $B(E2)$ values towards the proton drip-line. However, it does not agree with the experimental $B(E2)$ data on the

neutron rich side. The energies of the first $2^+$ state and the first $4^+$ state in the $N = Z + 2$ nucleus $^{110}$Xe was recently measured [61]. It was concluded there that the trend of increasing energy of the first $2^+$ state and the first $4^+$ state with decreasing neutron number was broken as the $N = 50$ shell gap was approached and that this could imply a weakening of the $N = Z = 50$ gap [61].

The $^{100}$Sn core is not LS-closed since the $N = Z = 50$ shell gap emerges from the splitting of $1g$ orbit due to the spin-orbit force, Fig. 2.2. Quadrupole excitations are therefore allowed across the $1g_{9/2} - 1g_{7/2}$ shell gap[1]. An E2 excitation is not allowed from an LS-closed core such as $^{16}$O unless it takes place to the second major oscillator shell above the core. There are only two self-conjugate non-LS closed cores; $^{100}$Sn and $^{56}$Ni.

Neutrons and protons occupy the same orbits in $N = Z$ nuclei. It is shown in [62] that the interaction between nucleons in spin-orbit partner orbits $\ell \pm 1/2$ [2] interact in a certain way. The $\ell_\uparrow$ - $\ell_\downarrow$ interaction is strongly attractive especially between neutrons and protons. The $\ell_\uparrow$-$\ell_\uparrow$ and $\ell_\downarrow$-$\ell_\downarrow$ interaction is repulsive. This tensor force could strongly modify the effective single particle energies [62]. The spin-orbit splitting between the neutron $2p_{3/2} - 2p_{1/2}$ was recently investigated experimentally [63]. The single particle energies of $^{47}$Ar (Z=18) were obtained via transfer reactions. The location of the neutron $2p_{3/2}$ and $2p_{1/2}$ orbits in $^{49}$Ca (Z=20) were 875(130)keV larger. This was suggested [63] to originate in the weakened spin-orbit interaction due to the removal of two protons from $1d_{3/2}$ and $2s_{1/2}$. The combined effect caused a weakening of the $N = 28$ shell closure [63].

The variation of the spin-orbit force with nucleon number and relative spin orientation of the particles is of the same origin as the neutron-proton correlations discussed in [64, 52]. With analogous reasoning the proton $1g_{9/2}$ orbit could become less bound as the number of neutrons in the $1g_{7/2}$ orbit decrease as the proton drip line is approached. This would favor the probability for proton excitations across the $Z = 50$ shell gap, which would increase the $B(E2; 0_{gs} \rightarrow 2_1^+)$ values in neutron-deficient Sn isotopes towards the proton drip line. A seniority truncated shell-model calculation[3] using $^{90}$Zr as an inert core clearly shows the increase in transition probability as proton excitations across the $Z = 50$ are included [1], see Fig. 6.4. The proton effective charge was set to $1.5$ e and the neutron effective charge was to $0.5$ e in this calculation. The model space comprised the neutron $1g_{7/2}2d3s1h_{11/2}$ orbits and the proton $1g2d3s$ orbits.

The $B(E2; 6_1^+ \rightarrow 4_1^+)$ in the even-mass $^{102-110}$Sn isotopes are known from experiment [65, 66, 67] and summarized in Tab. 6.1. The consensus amongst published microscopic calculations with G-matrix interactions [68] is that an effective neutron charge of $2.0$ e is required in order to reproduce the experimental values. A large effective charge clearly indicates the need for an expanded valence space within shell-model calculation.

[1] The parity of the $E\lambda$ operator is $(-1)^\lambda$

[2] $\ell_\uparrow \equiv \ell + 1/2$ and $\ell_\downarrow \equiv \ell - 1/2$

[3] By imposing seniority the $B(E2)$ trend across the Sn isotopic chain will automatically be of symmetric parabolic character

| Isotope | $E(6_1^+)$ / MeV | $E_\gamma$ / MeV | $B(E2; 6_1^+ \rightarrow 4_1^+)$ / $e^2b^2$ |
|---|---|---|---|
| $^{102}$Sn[a] | 2.02 | 0.05 | $1.16(50) \cdot 10^{-2}$ |
| $^{104}$Sn[b] | 2.26 | 0.32 | $1.13(17) \cdot 10^{-2}$ |
| $^{106}$Sn[c] | 2.32 | 0.30 | $7.4(1.3) \cdot 10^{-3}$ |
| $^{108}$Sn | 2.36 | 0.25 | $6.8(4) \cdot 10^{-3}$ |
| $^{110}$Sn | 2.48 | 0.28 | $5.5(4) \cdot 10^{-3}$ |

Table 6.1: *Experimental $B(E2)$ values for higher lying transitions in $^{102-110}$Sn. The third column contains the transition energy.*

[a] Ref. [67]
[b] Ref. [66]
[c] Ref. [65] $^{106-110}$Sn

## 6.1 Shell-Model Calculations in the Sn Isotopes

For the calculations presented here, the size of the valence space is restricted to the neutron orbits between $N = 50 - 82$; $1g_{7/2}2d_{5/2}3s_{1/2}2d_{3/2}1h_{11/2}$. The restriction is due to current computational limitations. The neutron $1g_{7/2} - 2d_{5/2}$ energy difference was recently measured [69] in $^{101}$Sn to $171.7(6)$ keV. The light Sn isotopes have been investigated theoretically in e.g. [70, 71, 1] and references therein. Two sets of single particle energies are considered here, see Fig. 6.3. The calculation from [1] is based on $^{100}$Sn as inert core and use SPE(1).It

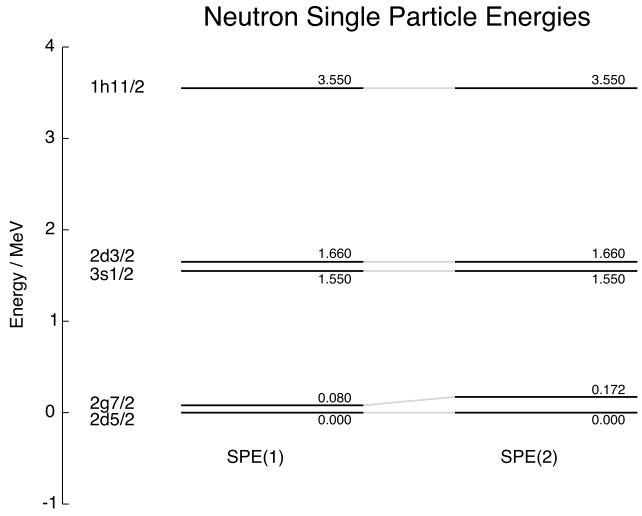


Figure 6.3: *Neutron single particle energies (SPE) used in the shell-model calculations presented here. SPE(1) was used in [1], while the experimentally determined $1g_{7/2} - 2d_{5/2}$ is included in SPE(2).*

successfully reproduces the energy of the $2_1^+$ states in the even-mass $^{102-130}$Sn isotopes, see Tab 6.2. The CD-Bonn interaction was renormalized using the G-matrix with the oscillator parameter $\hbar\omega = 45A^{-1/3} - 25A - 2/3 = 8.5$ MeV [14]. The effective interaction was constructed using third order many body perturbation theory allowing for excitations up

to $2\hbar\omega$, see Sec. 2.2. The calculations were carried out using computer codes developed by Hjorth-Jensen [14]. With an effective neutron charge set to $e_{\text{eff}} = 1.0$ e the experimental $B(E2; 0_{gs} \rightarrow 2_1^+)$ values in $^{116-130}$Sn are reproduced, Fig. 5.1. The calculation fails to reproduce the experimental $B(E2)$ values for isotopes with $N < 66$. Using single particle energies denoted SPE(2) in Fig. 6.3 instead of single particle energies denoted SPE(1) in the same figure gave negligible differences.

A second set of shell-model calculation was carried out here. Compared to the prior calculation, they now allowed for $5\hbar\omega$ excitations, but in all other respects they were identical. However, apart from the CD-Bonn interaction a calculation based on the N3LO interaction was also carried out. The calculated $B(E2)$ values differ slightly from [1], see Fig. 6.4. The

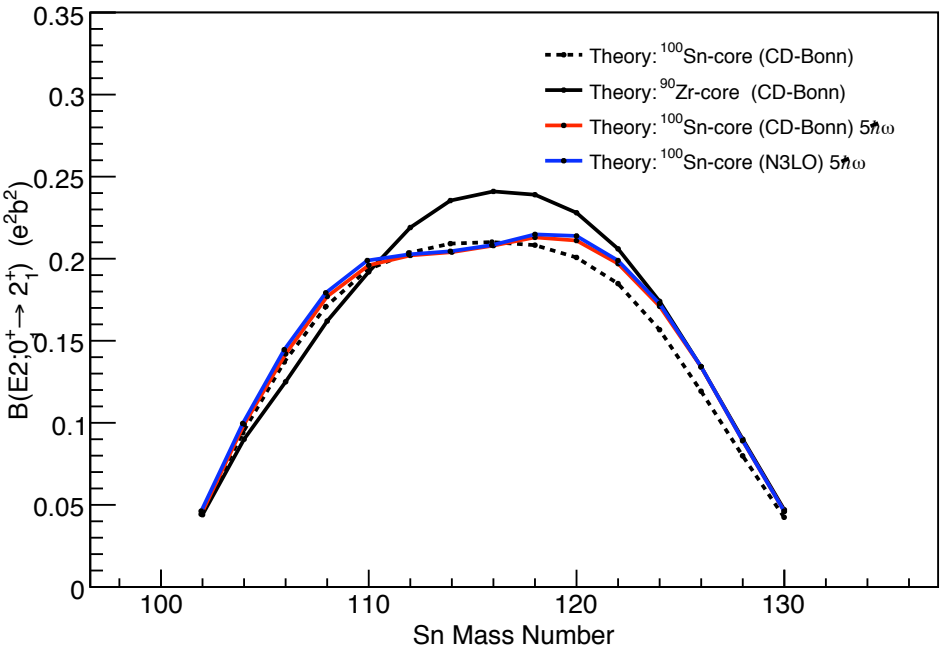


Figure 6.4: *A summary of the $B(E2)$ values. The calculation based on $^{90}$Zr core was seniority truncated. The remaining calculations differ only in number of excitations allowed for in the perturbative scheme, $2\hbar\omega$ or $5\hbar\omega$. The interaction was either CD-Bonn or N3LO. See text for further details.*

difference can possibly be attributed to the range of allowed excitations in the perturbative scheme. It is interesting to note that the inclusion of higher order excitations gives a result that start to deviate slightly from a good seniority picture. The resulting two-body matrix elements using the N3LO interaction are close to identical to the ones obtained from CD-Bonn. See App. A for details regarding the $5\hbar\omega$ calculations. The energy level-structure in $^{102-130}$Sn calculated with N3LO is compared with the CD-Bonn results in Fig. 6.5. The theoretical energy levels from N3LO and CD-Bonn (using both $2\hbar\omega$ and $5\hbar\omega$) are compared with the experimental results in Tab. 6.2. A theoretical energy spectrum for $^{108}$Sn including higher

lying levels is compared with the corresponding experimental levels in Fig. 6.6.

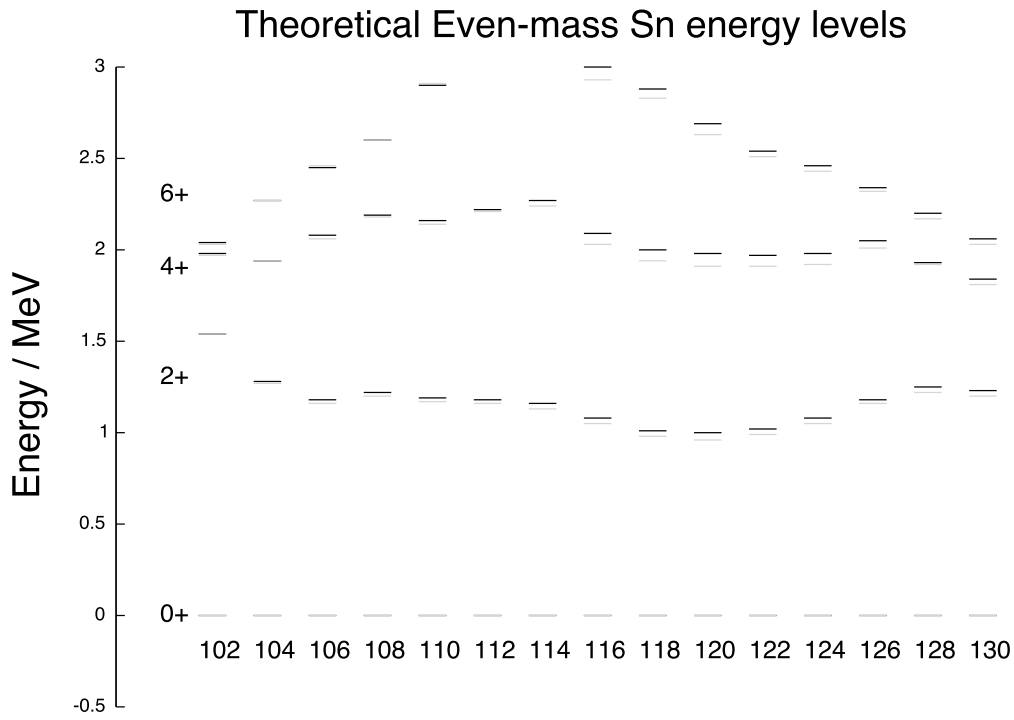


Figure 6.5: *black - CD-Bonn , grey - N3LO. The lines represent, in order, the position of the first* $2^+, 4^+$*, and* $6^+$ *where present. Many more levels are obtained from the diagonalization, however they are left out in this figure in order to make the CD-Bonn/N3LO comparison clear. See text for details.*

## 6.2 Outlook

The experimental $B(E2)$ values in the neutron-deficient isotopes might be reproduced in an extended shell-model calculation with the inclusion of the neutron and the proton $1g_{9/2}$ orbit. Without the aforementioned seniority truncation, the model space dimension will grow combinatorially larger than the present-day computational limit of a $\sim 10^9$ model space dimension. The model space dimensions for the calculations presented here are shown in Fig. 6.7. The dimensions of the extended model space can be reduced by freezing a few particles to the $1g_{9/2}$ orbit. Nevertheless, the calculations must be carried out on a computational cluster. A parallel shell-model code that can handle both proton and neutron excitations is under production by the Oslo group [72].

Measurements of the $B(E2)$ values in $^{100,102,104}$Cd are planned for 2008. The Cd isotopes have two protons less than the $^{100}$Sn core. Results from shell-model calculations of neutron-

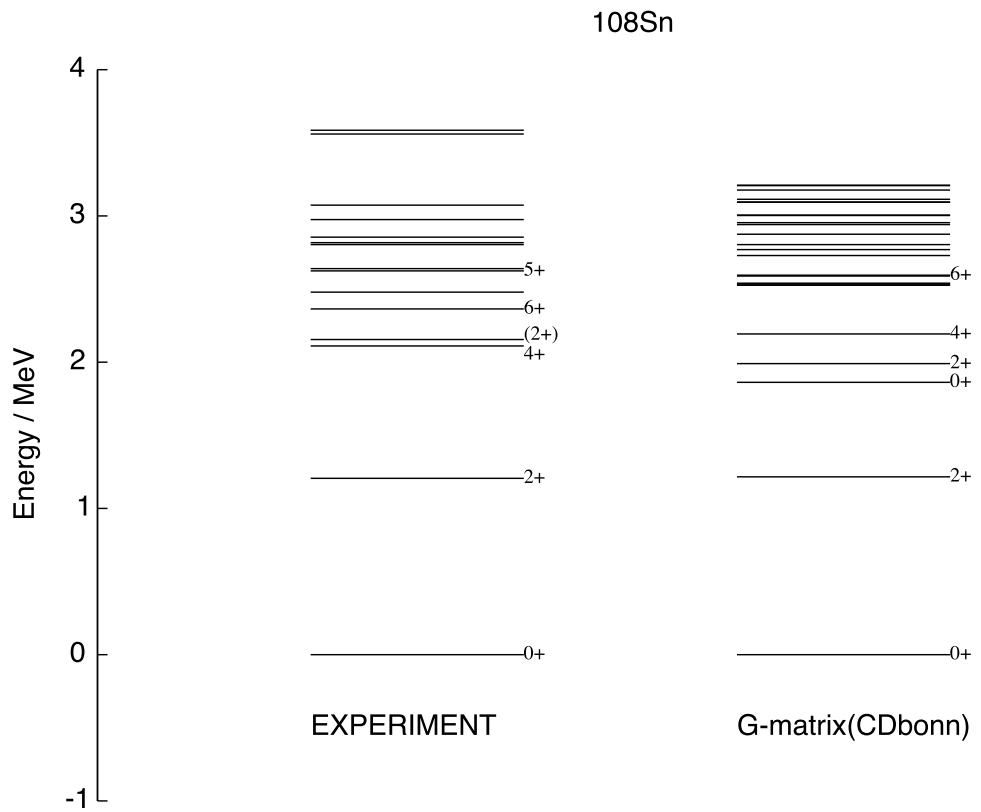


Figure 6.6: *Calculated energy levels in $^{108}$Sn compared with the experimental levels. The calculation is based on the CD-Bonn interaction with $5\hbar\omega$ excitations. The first excited $2^+$ and $4^+$ states are well reproduced. The higher lying theoretical level structure is more difficult to interpret.*

deficient even-mass Cd isotopes show that the neutrons and protons are weakly coupled in these nuclei. This implies that one can expect the neutron degree of freedom to be similar to the one in the even-mass tin isotopes [72].

It is also of interest to measure the $B(E2)$ values in $^{104}$Sn and the even lighter isotope $^{102}$Sn and ultimately $^{100}$Sn. These experiments are currently limited due to the relatively low beam intensities.

| | Experiment | | CD-Bonn ($5\hbar\omega$) | | CD-Bonn ($2\hbar\omega$) | N3LO ($5\hbar\omega$) | |
|---|---|---|---|---|---|---|---|
| Isotope | $E(2_1^+)$ | $E(4_1^+)$ | $E(2_1^+)$ | $E(4_1^+)$ | $E(2_1^+)$ | $E(2_1^+)$ | $E(4_1^+)$ |
| $^{102}$Sn | 1.47 | 1.97 | 1.54 | 1.98 | 1.65 | 1.54 | 1.97 |
| $^{104}$Sn | 1.26 | 1.94 | 1.28 | 1.94 | 1.34 | 1.27 | 1.94 |
| $^{106}$Sn | 1.21 | 2.02 | 1.18 | 2.08 | 1.23 | 1.16 | 2.06 |
| $^{108}$Sn | 1.21 | 2.11 | 1.22 | 2.19 | 1.24 | 1.20 | 2.18 |
| $^{110}$Sn | 1.21 | 2.20 | 1.19 | 2.16 | 1.26 | 1.17 | 2.14 |
| $^{112}$Sn | 1.26 | 2.25 | 1.18 | 2.22 | 1.24 | 1.16 | 2.21 |
| $^{114}$Sn | 1.30 | 2.19 | 1.16 | 2.27 | 1.21 | 1.13 | 2.24 |
| $^{116}$Sn | 1.30 | 2.39 | 1.08 | 2.09 | 1.14 | 1.05 | 2.03 |
| $^{118}$Sn | 1.23 | 2.28 | 1.01 | 2.00 | 1.07 | 0.98 | 1.04 |
| $^{120}$Sn | 1.17 | 2.19 | 1.00 | 1.98 | 1.04 | 0.96 | 1.91 |
| $^{122}$Sn | 1.14 | 2.14 | 1.02 | 1.97 | 1.08 | 0.99 | 1.91 |
| $^{124}$Sn | 1.13 | 2.10 | 1.08 | 1.98 | 1.12 | 1.05 | 1.92 |
| $^{126}$Sn | 1.14 | 2.05 | 1.18 | 2.05 | 1.21 | 1.16 | 2.01 |
| $^{128}$Sn | 1.17 | 2.00 | 1.25 | 1.93 | 1.23 | 1.22 | 1.92 |
| $^{130}$Sn | 1.22 | 2.00 | 1.23 | 1.84 | 1.19 | 1.20 | 1.81 |

Table 6.2: *Experimental and theoretical energies of the $2_1^+$ and $4_1^+$ levels in the even-mass Sn isotopes. The theoretical results are based on two different nuclear interactions, CD-Bonn or N3LO. The energy truncation in the G-matrix perturbation is given within parenthesis.*

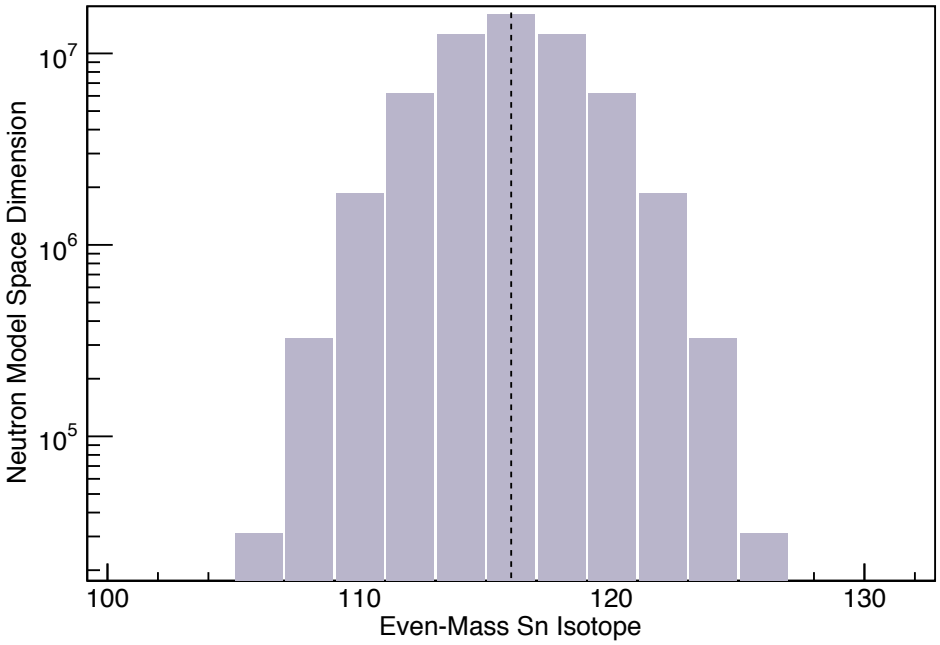


Figure 6.7: *The neutron $1g_{7/2}2d_{5/2}3s_{1/2}1h_{11/2}$ model space dimension in shell-model calculations.*

# Acknowledgments

First and foremost, I would like to thank my supervisor, Joakim Cederkäll, for his professional guidance, team spirit and invaluable advice in all aspects of the work.

I would also like to thank my co-supervisor, Claes Fahlander, for support and very interesting and helpful discussions.

My office mates, Emma Johansson, Lise-Lotte Andersson and former office mate Diego Torres together with the rest of the nuclear structure group in Lund for creating a very pleasant working atmosphere.

Thank you Morten Hjorth-Jensen, for answering all my questions about nuclear interactions and for the financial support allowing me to spend two inspiring weeks at Oslo University. Thank you Torgeir Engeland at Oslo University, for helping me with the shell-model codes.

I would also like to thank Kungliga Fysiografiska Sällskapet in Lund for the financial support that enabled me to spend three months at CERN.

# Appendix A

# Effective Two-Body Matrix Elements

Neutron Two-Body Matrix Elements (TBME) given in Tabs. A.1 and A.4 are of the form

$$\langle n_a \ell_a j_a n_b \ell_b j_b | V_{\text{eff}} | n_c \ell_c j_c n_d \ell_d j_d \rangle_{JT} \tag{A.1}$$

The two rightmost columns give the value in MeV for the two different effective nucleon-nucleon interactions, $V_{\text{eff}}$, of relevance in the present case. The TBME were used as input in the shell-model calculations described in Ch. 6
Explanation of notation:

- $n$ - radial quantum number
- $\ell$ - orbital angular momentum
- $j$ - total angular momentum of the nucleon orbit
- $J$ - total coupled angular momentum of the interaction
- $T$ - total isopin of the interaction

The following input was used when renormalizing the free nucleon-nucleon interaction for use with a $^{100}$Sn core shell-model calculation.

*G-matrix calculation*

- $V_{\mathcal{NN}}$: N$^3$LO or CD-Bonn
- The oscillator energy $\hbar\omega = 8.5$ MeV[1]
- Number of nucleons, $A = 100$. The G-matrix result has a weak dependence on A. The problem is connected with the spurious states originating in center of mass motion coming from translational non-invariance in the one-body field $u_i$ in the residual interaction $V$. The $A$-dependence in the $G-$matrix comes from the $\frac{k_i \cdot k_j}{mA}$ center of mass term. With $A$ =100, this term is negligible.
- A square Pauli operator $\mathcal{Q}_F$ [14]
- A $Q$-space truncated at $\ell_{LAB} = 7$ and $n_{LAB} = 3$, leading to 72 orbits included up to $N = 7$.
- Include nucleon-nucleon interaction data for partial waves $0 \leq \ell \leq 10$
- 10 $G-$matrix starting energies between -5.0 and -150.0 MeV

*Perturbation Expansion:*

- Third order many body perturbation theory using open-diagrams.
- Allowing intermediate state excitation of maximum 5 $\hbar\omega$
- Degenerate valence energies in the neutron $(1g_{7/2}2d3s1h_{11/2})$ model space set to $-10.0$ MeV
- Starting energy of $-20.0$ MeV

The $P$ space defined to include the neutron orbits $1g_{7/2}2d3s1h_{11/2}$. In order to avoid poles[2] in a perturbative expansion of a multi-shell (non-LS closed) $P$ space the $1g_{7/2}$ and $1h_{11/2}$ orbits were altered to belong to the same major oscillator shell as the $2d3s$ orbits.

[1] Using parameterization $\hbar\omega = 45 \cdot A^{-2/3} - 25A^{1/3}$

[2] See p.219 in Ref. [14]. Result in program termination

| $n_a$ | $\ell_a$ | $j_a$ | $n_b$ | $\ell_b$ | $j_b$ | $n_c$ | $\ell_c$ | $j_c$ | $n_d$ | $\ell_d$ | $j_d$ | $2T$ | $2J$ | N3lO | CD-Bonn |
|---|---|---|---|---|---|---|---|---|---|---|---|---|---|---|---|
| 0 | 4 | 7 | 0 | 4 | 7 | 0 | 4 | 7 | 0 | 4 | 7 | 2 | 0 | -1.294649 | -1.292410 |
| 0 | 4 | 7 | 0 | 4 | 7 | 1 | 2 | 5 | 1 | 2 | 5 | 2 | 0 | -0.630048 | -0.636278 |
| 0 | 4 | 7 | 0 | 4 | 7 | 1 | 2 | 3 | 1 | 2 | 3 | 2 | 0 | -0.652301 | -0.648606 |
| 0 | 4 | 7 | 0 | 4 | 7 | 2 | 0 | 1 | 2 | 0 | 1 | 2 | 0 | -0.308742 | -0.311734 |
| 0 | 4 | 7 | 0 | 4 | 7 | 0 | 5 | 11 | 0 | 5 | 11 | 2 | 0 | 1.290802 | 1.321735 |
| 1 | 2 | 5 | 1 | 2 | 5 | 1 | 2 | 5 | 1 | 2 | 5 | 2 | 0 | -0.886330 | -0.870426 |
| 1 | 2 | 5 | 1 | 2 | 5 | 1 | 2 | 3 | 1 | 2 | 3 | 2 | 0 | -1.062040 | -1.065016 |
| 1 | 2 | 5 | 1 | 2 | 5 | 2 | 0 | 1 | 2 | 0 | 1 | 2 | 0 | -0.453857 | -0.442361 |
| 1 | 2 | 5 | 1 | 2 | 5 | 0 | 5 | 11 | 0 | 5 | 11 | 2 | 0 | 0.875475 | 0.879563 |
| 1 | 2 | 3 | 1 | 2 | 3 | 1 | 2 | 3 | 1 | 2 | 3 | 2 | 0 | -0.445816 | -0.432020 |
| 1 | 2 | 3 | 1 | 2 | 3 | 2 | 0 | 1 | 2 | 0 | 1 | 2 | 0 | -0.378740 | -0.370515 |
| 1 | 2 | 3 | 1 | 2 | 3 | 0 | 5 | 11 | 0 | 5 | 11 | 2 | 0 | 0.602774 | 0.609465 |
| 2 | 0 | 1 | 2 | 0 | 1 | 2 | 0 | 1 | 2 | 0 | 1 | 2 | 0 | -0.916551 | -0.913477 |
| 2 | 0 | 1 | 2 | 0 | 1 | 0 | 5 | 11 | 0 | 5 | 11 | 2 | 0 | 0.385177 | 0.387503 |
| 0 | 5 | 11 | 0 | 5 | 11 | 0 | 5 | 11 | 0 | 5 | 11 | 2 | 0 | -1.306377 | -1.305552 |
| 0 | 4 | 7 | 1 | 2 | 5 | 0 | 4 | 7 | 1 | 2 | 5 | 2 | 2 | -0.185566 | -0.153967 |
| 0 | 4 | 7 | 1 | 2 | 5 | 1 | 2 | 5 | 1 | 2 | 3 | 2 | 2 | -0.021650 | -0.021458 |
| 0 | 4 | 7 | 1 | 2 | 5 | 1 | 2 | 3 | 2 | 0 | 1 | 2 | 2 | -0.112921 | -0.108018 |
| 1 | 2 | 5 | 1 | 2 | 3 | 1 | 2 | 5 | 1 | 2 | 3 | 2 | 2 | -0.017921 | 0.000909 |
| 1 | 2 | 5 | 1 | 2 | 3 | 1 | 2 | 3 | 2 | 0 | 1 | 2 | 2 | -0.021708 | -0.021128 |
| 1 | 2 | 3 | 2 | 0 | 1 | 1 | 2 | 3 | 2 | 0 | 1 | 2 | 2 | 0.060759 | 0.075675 |
| 0 | 4 | 7 | 0 | 4 | 7 | 0 | 4 | 7 | 0 | 4 | 7 | 2 | 4 | -0.330022 | -0.325755 |
| 0 | 4 | 7 | 0 | 4 | 7 | 0 | 4 | 7 | 1 | 2 | 5 | 2 | 4 | -0.034693 | -0.026919 |
| 0 | 4 | 7 | 0 | 4 | 7 | 0 | 4 | 7 | 1 | 2 | 3 | 2 | 4 | -0.353656 | -0.354116 |
| 0 | 4 | 7 | 0 | 4 | 7 | 1 | 2 | 5 | 1 | 2 | 5 | 2 | 4 | -0.103557 | -0.106056 |
| 0 | 4 | 7 | 0 | 4 | 7 | 1 | 2 | 5 | 1 | 2 | 3 | 2 | 4 | -0.197251 | -0.197269 |
| 0 | 4 | 7 | 0 | 4 | 7 | 1 | 2 | 5 | 2 | 0 | 1 | 2 | 4 | -0.205870 | -0.207795 |
| 0 | 4 | 7 | 0 | 4 | 7 | 1 | 2 | 3 | 1 | 2 | 3 | 2 | 4 | -0.242040 | -0.239232 |
| 0 | 4 | 7 | 0 | 4 | 7 | 1 | 2 | 3 | 2 | 0 | 1 | 2 | 4 | 0.127824 | 0.129585 |
| 0 | 4 | 7 | 0 | 4 | 7 | 0 | 5 | 11 | 0 | 5 | 11 | 2 | 4 | 0.250180 | 0.261629 |
| 0 | 4 | 7 | 1 | 2 | 5 | 0 | 4 | 7 | 1 | 2 | 5 | 2 | 4 | 0.015173 | 0.032952 |
| 0 | 4 | 7 | 1 | 2 | 5 | 0 | 4 | 7 | 1 | 2 | 3 | 2 | 4 | 0.267724 | 0.264671 |
| 0 | 4 | 7 | 1 | 2 | 5 | 1 | 2 | 5 | 1 | 2 | 5 | 2 | 4 | 0.077200 | 0.077180 |
| 0 | 4 | 7 | 1 | 2 | 5 | 1 | 2 | 5 | 1 | 2 | 3 | 2 | 4 | 0.097109 | 0.095398 |
| 0 | 4 | 7 | 1 | 2 | 5 | 1 | 2 | 5 | 2 | 0 | 1 | 2 | 4 | 0.086970 | 0.088653 |
| 0 | 4 | 7 | 1 | 2 | 5 | 1 | 2 | 3 | 1 | 2 | 3 | 2 | 4 | 0.025179 | 0.025656 |
| 0 | 4 | 7 | 1 | 2 | 5 | 1 | 2 | 3 | 2 | 0 | 1 | 2 | 4 | -0.098159 | -0.095201 |
| 0 | 4 | 7 | 1 | 2 | 5 | 0 | 5 | 11 | 0 | 5 | 11 | 2 | 4 | -0.282206 | -0.283253 |
| 0 | 4 | 7 | 1 | 2 | 3 | 0 | 4 | 7 | 1 | 2 | 3 | 2 | 4 | -0.443691 | -0.441678 |
| 0 | 4 | 7 | 1 | 2 | 3 | 1 | 2 | 5 | 1 | 2 | 5 | 2 | 4 | -0.183420 | -0.181415 |
| 0 | 4 | 7 | 1 | 2 | 3 | 1 | 2 | 5 | 1 | 2 | 3 | 2 | 4 | -0.193863 | -0.194449 |
| 0 | 4 | 7 | 1 | 2 | 3 | 1 | 2 | 5 | 2 | 0 | 1 | 2 | 4 | -0.246399 | -0.245654 |
| 0 | 4 | 7 | 1 | 2 | 3 | 1 | 2 | 3 | 1 | 2 | 3 | 2 | 4 | -0.212077 | -0.211698 |
| 0 | 4 | 7 | 1 | 2 | 3 | 1 | 2 | 3 | 2 | 0 | 1 | 2 | 4 | 0.296783 | 0.293865 |
| 0 | 4 | 7 | 1 | 2 | 3 | 0 | 5 | 11 | 0 | 5 | 11 | 2 | 4 | 0.401225 | 0.408985 |

Table A.1: *Two-Body Matrix Elements (TBME) given in MeV. See text for details*

| $n_a$ | $\ell_a$ | $j_a$ | $n_b$ | $\ell_b$ | $j_b$ | $n_c$ | $\ell_c$ | $j_c$ | $n_d$ | $\ell_d$ | $j_d$ | $2T$ | $2J$ | N3lO | CD-Bonn |
|---|---|---|---|---|---|---|---|---|---|---|---|---|---|---|---|
| 1 | 2 | 5 | 1 | 2 | 5 | 1 | 2 | 5 | 1 | 2 | 5 | 2 | 4 | -0.320944 | -0.316008 |
| 1 | 2 | 5 | 1 | 2 | 5 | 1 | 2 | 5 | 1 | 2 | 3 | 2 | 4 | -0.120252 | -0.126757 |
| 1 | 2 | 5 | 1 | 2 | 5 | 1 | 2 | 5 | 2 | 0 | 1 | 2 | 4 | -0.350513 | -0.348293 |
| 1 | 2 | 5 | 1 | 2 | 5 | 1 | 2 | 3 | 1 | 2 | 3 | 2 | 4 | -0.233662 | -0.237051 |
| 1 | 2 | 5 | 1 | 2 | 5 | 1 | 2 | 3 | 2 | 0 | 1 | 2 | 4 | 0.286912 | 0.285653 |
| 1 | 2 | 5 | 1 | 2 | 5 | 0 | 5 | 11 | 0 | 5 | 11 | 2 | 4 | 0.410746 | 0.410922 |
| 1 | 2 | 5 | 1 | 2 | 3 | 1 | 2 | 5 | 1 | 2 | 3 | 2 | 4 | -0.076793 | -0.065589 |
| 1 | 2 | 5 | 1 | 2 | 3 | 1 | 2 | 5 | 2 | 0 | 1 | 2 | 4 | -0.157982 | -0.154730 |
| 1 | 2 | 5 | 1 | 2 | 3 | 1 | 2 | 3 | 1 | 2 | 3 | 2 | 4 | -0.272372 | -0.274532 |
| 1 | 2 | 5 | 1 | 2 | 3 | 1 | 2 | 3 | 2 | 0 | 1 | 2 | 4 | 0.273993 | 0.272151 |
| 1 | 2 | 5 | 1 | 2 | 3 | 0 | 5 | 11 | 0 | 5 | 11 | 2 | 4 | 0.029695 | 0.032622 |
| 1 | 2 | 5 | 2 | 0 | 1 | 1 | 2 | 5 | 2 | 0 | 1 | 2 | 4 | -0.524481 | -0.519514 |
| 1 | 2 | 5 | 2 | 0 | 1 | 1 | 2 | 3 | 1 | 2 | 3 | 2 | 4 | -0.272544 | -0.268868 |
| 1 | 2 | 5 | 2 | 0 | 1 | 1 | 2 | 3 | 2 | 0 | 1 | 2 | 4 | 0.556202 | 0.561456 |
| 1 | 2 | 5 | 2 | 0 | 1 | 0 | 5 | 11 | 0 | 5 | 11 | 2 | 4 | 0.226482 | 0.228937 |
| 1 | 2 | 3 | 1 | 2 | 3 | 1 | 2 | 3 | 1 | 2 | 3 | 2 | 4 | -0.007621 | -0.003363 |
| 1 | 2 | 3 | 1 | 2 | 3 | 1 | 2 | 3 | 2 | 0 | 1 | 2 | 4 | 0.159747 | 0.159501 |
| 1 | 2 | 3 | 1 | 2 | 3 | 0 | 5 | 11 | 0 | 5 | 11 | 2 | 4 | 0.103165 | 0.105564 |
| 1 | 2 | 3 | 2 | 0 | 1 | 1 | 2 | 3 | 2 | 0 | 1 | 2 | 4 | -0.227764 | -0.217922 |
| 1 | 2 | 3 | 2 | 0 | 1 | 0 | 5 | 11 | 0 | 5 | 11 | 2 | 4 | -0.228625 | -0.230979 |
| 0 | 5 | 11 | 0 | 5 | 11 | 0 | 5 | 11 | 0 | 5 | 11 | 2 | 4 | -0.737822 | -0.727424 |
| 0 | 4 | 7 | 1 | 2 | 5 | 0 | 4 | 7 | 1 | 2 | 5 | 2 | 6 | 0.129725 | 0.137180 |
| 0 | 4 | 7 | 1 | 2 | 5 | 0 | 4 | 7 | 1 | 2 | 3 | 2 | 6 | 0.087133 | 0.089538 |
| 0 | 4 | 7 | 1 | 2 | 5 | 0 | 4 | 7 | 2 | 0 | 1 | 2 | 6 | -0.134365 | -0.127879 |
| 0 | 4 | 7 | 1 | 2 | 5 | 1 | 2 | 5 | 1 | 2 | 3 | 2 | 6 | -0.033893 | -0.033497 |
| 0 | 4 | 7 | 1 | 2 | 5 | 1 | 2 | 5 | 2 | 0 | 1 | 2 | 6 | -0.038422 | -0.038148 |
| 0 | 4 | 7 | 1 | 2 | 3 | 0 | 4 | 7 | 1 | 2 | 3 | 2 | 6 | 0.149367 | 0.150591 |
| 0 | 4 | 7 | 1 | 2 | 3 | 0 | 4 | 7 | 2 | 0 | 1 | 2 | 6 | -0.129980 | -0.121497 |
| 0 | 4 | 7 | 1 | 2 | 3 | 1 | 2 | 5 | 1 | 2 | 3 | 2 | 6 | -0.010662 | -0.010795 |
| 0 | 4 | 7 | 1 | 2 | 3 | 1 | 2 | 5 | 2 | 0 | 1 | 2 | 6 | -0.004603 | -0.004771 |
| 0 | 4 | 7 | 2 | 0 | 1 | 0 | 4 | 7 | 2 | 0 | 1 | 2 | 6 | 0.154456 | 0.163704 |
| 0 | 4 | 7 | 2 | 0 | 1 | 1 | 2 | 5 | 1 | 2 | 3 | 2 | 6 | -0.000734 | 0.000084 |
| 0 | 4 | 7 | 2 | 0 | 1 | 1 | 2 | 5 | 2 | 0 | 1 | 2 | 6 | 0.025881 | 0.026636 |
| 1 | 2 | 5 | 1 | 2 | 3 | 1 | 2 | 5 | 1 | 2 | 3 | 2 | 6 | 0.075141 | 0.083941 |
| 1 | 2 | 5 | 1 | 2 | 3 | 1 | 2 | 5 | 2 | 0 | 1 | 2 | 6 | -0.049404 | -0.051015 |
| 1 | 2 | 5 | 2 | 0 | 1 | 1 | 2 | 5 | 2 | 0 | 1 | 2 | 6 | -0.020682 | -0.008809 |
| 0 | 4 | 7 | 0 | 4 | 7 | 0 | 4 | 7 | 0 | 4 | 7 | 2 | 8 | 0.099841 | 0.095694 |
| 0 | 4 | 7 | 0 | 4 | 7 | 0 | 4 | 7 | 1 | 2 | 5 | 2 | 8 | 0.096596 | 0.099669 |
| 0 | 4 | 7 | 0 | 4 | 7 | 0 | 4 | 7 | 1 | 2 | 3 | 2 | 8 | -0.248174 | -0.243946 |
| 0 | 4 | 7 | 0 | 4 | 7 | 0 | 4 | 7 | 2 | 0 | 1 | 2 | 8 | 0.105993 | 0.106312 |
| 0 | 4 | 7 | 0 | 4 | 7 | 1 | 2 | 5 | 1 | 2 | 5 | 2 | 8 | -0.077049 | -0.078122 |
| 0 | 4 | 7 | 0 | 4 | 7 | 1 | 2 | 5 | 1 | 2 | 3 | 2 | 8 | -0.219163 | -0.220008 |
| 0 | 4 | 7 | 0 | 4 | 7 | 0 | 5 | 11 | 0 | 5 | 11 | 2 | 8 | 0.147878 | 0.154518 |
| 0 | 4 | 7 | 1 | 2 | 5 | 0 | 4 | 7 | 1 | 2 | 5 | 2 | 8 | 0.114006 | 0.117002 |
| 0 | 4 | 7 | 1 | 2 | 5 | 0 | 4 | 7 | 1 | 2 | 3 | 2 | 8 | 0.178078 | 0.180120 |

Table A.2: *Two-Body Matrix Elements (TBME) given in MeV. See text for details*

| $n_a$ | $\ell_a$ | $j_a$ | $n_b$ | $\ell_b$ | $j_b$ | $n_c$ | $\ell_c$ | $j_c$ | $n_d$ | $\ell_d$ | $j_d$ | $2T$ | $2J$ | N3lO | CD-Bonn |
|---|---|---|---|---|---|---|---|---|---|---|---|---|---|---|---|
| 0 | 4 | 7 | 1 | 2 | 5 | 0 | 4 | 7 | 2 | 0 | 1 | 2 | 8 | -0.303928 | -0.297828 |
| 0 | 4 | 7 | 1 | 2 | 5 | 1 | 2 | 5 | 1 | 2 | 5 | 2 | 8 | 0.079388 | 0.078683 |
| 0 | 4 | 7 | 1 | 2 | 5 | 1 | 2 | 5 | 1 | 2 | 3 | 2 | 8 | 0.188972 | 0.186851 |
| 0 | 4 | 7 | 1 | 2 | 5 | 0 | 5 | 11 | 0 | 5 | 11 | 2 | 8 | -0.201159 | -0.203205 |
| 0 | 4 | 7 | 1 | 2 | 3 | 0 | 4 | 7 | 1 | 2 | 3 | 2 | 8 | 0.069284 | 0.066520 |
| 0 | 4 | 7 | 1 | 2 | 3 | 0 | 4 | 7 | 2 | 0 | 1 | 2 | 8 | 0.254114 | 0.252030 |
| 0 | 4 | 7 | 1 | 2 | 3 | 1 | 2 | 5 | 1 | 2 | 5 | 2 | 8 | -0.060081 | -0.058122 |
| 0 | 4 | 7 | 1 | 2 | 3 | 1 | 2 | 5 | 1 | 2 | 3 | 2 | 8 | -0.185335 | -0.183183 |
| 0 | 4 | 7 | 1 | 2 | 3 | 0 | 5 | 11 | 0 | 5 | 11 | 2 | 8 | 0.143230 | 0.146483 |
| 0 | 4 | 7 | 2 | 0 | 1 | 0 | 4 | 7 | 2 | 0 | 1 | 2 | 8 | -0.086085 | -0.085442 |
| 0 | 4 | 7 | 2 | 0 | 1 | 1 | 2 | 5 | 1 | 2 | 5 | 2 | 8 | 0.119102 | 0.115660 |
| 0 | 4 | 7 | 2 | 0 | 1 | 1 | 2 | 5 | 1 | 2 | 3 | 2 | 8 | 0.244951 | 0.241241 |
| 0 | 4 | 7 | 2 | 0 | 1 | 0 | 5 | 11 | 0 | 5 | 11 | 2 | 8 | -0.200677 | -0.202878 |
| 1 | 2 | 5 | 1 | 2 | 5 | 1 | 2 | 5 | 1 | 2 | 5 | 2 | 8 | -0.060738 | -0.058723 |
| 1 | 2 | 5 | 1 | 2 | 5 | 1 | 2 | 5 | 1 | 2 | 3 | 2 | 8 | -0.396255 | -0.399192 |
| 1 | 2 | 5 | 1 | 2 | 5 | 0 | 5 | 11 | 0 | 5 | 11 | 2 | 8 | 0.205420 | 0.205277 |
| 1 | 2 | 5 | 1 | 2 | 3 | 1 | 2 | 5 | 1 | 2 | 3 | 2 | 8 | -0.583800 | -0.581503 |
| 1 | 2 | 5 | 1 | 2 | 3 | 0 | 5 | 11 | 0 | 5 | 11 | 2 | 8 | 0.196102 | 0.198948 |
| 0 | 5 | 11 | 0 | 5 | 11 | 0 | 5 | 11 | 0 | 5 | 11 | 2 | 8 | -0.240486 | -0.240174 |
| 0 | 4 | 7 | 1 | 2 | 5 | 0 | 4 | 7 | 1 | 2 | 5 | 2 | 10 | 0.190943 | 0.190990 |
| 0 | 4 | 7 | 1 | 2 | 5 | 0 | 4 | 7 | 1 | 2 | 3 | 2 | 10 | -0.013754 | -0.009450 |
| 0 | 4 | 7 | 1 | 2 | 3 | 0 | 4 | 7 | 1 | 2 | 3 | 2 | 10 | 0.208427 | 0.213010 |
| 0 | 4 | 7 | 0 | 4 | 7 | 0 | 4 | 7 | 0 | 4 | 7 | 2 | 12 | 0.259528 | 0.254002 |
| 0 | 4 | 7 | 0 | 4 | 7 | 0 | 4 | 7 | 1 | 2 | 5 | 2 | 12 | 0.187409 | 0.186700 |
| 0 | 4 | 7 | 0 | 4 | 7 | 0 | 5 | 11 | 0 | 5 | 11 | 2 | 12 | 0.100030 | 0.104087 |
| 0 | 4 | 7 | 1 | 2 | 5 | 0 | 4 | 7 | 1 | 2 | 5 | 2 | 12 | -0.370617 | -0.364030 |
| 0 | 4 | 7 | 1 | 2 | 5 | 0 | 5 | 11 | 0 | 5 | 11 | 2 | 12 | -0.267955 | -0.270407 |
| 0 | 5 | 11 | 0 | 5 | 11 | 0 | 5 | 11 | 0 | 5 | 11 | 2 | 12 | -0.066066 | -0.065383 |
| 0 | 5 | 11 | 0 | 5 | 11 | 0 | 5 | 11 | 0 | 5 | 11 | 2 | 16 | 0.017921 | 0.019717 |
| 0 | 5 | 11 | 0 | 5 | 11 | 0 | 5 | 11 | 0 | 5 | 11 | 2 | 20 | 0.077298 | 0.079112 |
| 0 | 4 | 7 | 0 | 5 | 11 | 0 | 4 | 7 | 0 | 5 | 11 | 2 | 4 | -0.793741 | -0.760910 |
| 0 | 4 | 7 | 0 | 5 | 11 | 0 | 4 | 7 | 0 | 5 | 11 | 2 | 6 | -0.368338 | -0.346760 |
| 0 | 4 | 7 | 0 | 5 | 11 | 1 | 2 | 5 | 0 | 5 | 11 | 2 | 6 | 0.228142 | 0.227580 |
| 1 | 2 | 5 | 0 | 5 | 11 | 1 | 2 | 5 | 0 | 5 | 11 | 2 | 6 | -0.711804 | -0.711073 |
| 0 | 4 | 7 | 0 | 5 | 11 | 0 | 4 | 7 | 0 | 5 | 11 | 2 | 8 | -0.012296 | -0.002379 |
| 0 | 4 | 7 | 0 | 5 | 11 | 1 | 2 | 5 | 0 | 5 | 11 | 2 | 8 | 0.084006 | 0.079690 |
| 0 | 4 | 7 | 0 | 5 | 11 | 1 | 2 | 3 | 0 | 5 | 11 | 2 | 8 | -0.145208 | -0.141453 |
| 1 | 2 | 5 | 0 | 5 | 11 | 1 | 2 | 5 | 0 | 5 | 11 | 2 | 8 | -0.022759 | -0.021721 |
| 1 | 2 | 5 | 0 | 5 | 11 | 1 | 2 | 3 | 0 | 5 | 11 | 2 | 8 | -0.181359 | -0.175836 |
| 1 | 2 | 3 | 0 | 5 | 11 | 1 | 2 | 3 | 0 | 5 | 11 | 2 | 8 | -0.139598 | -0.131063 |
| 0 | 4 | 7 | 0 | 5 | 11 | 0 | 4 | 7 | 0 | 5 | 11 | 2 | 10 | -0.075806 | -0.072983 |
| 0 | 4 | 7 | 0 | 5 | 11 | 1 | 2 | 5 | 0 | 5 | 11 | 2 | 10 | 0.083312 | 0.087069 |
| 0 | 4 | 7 | 0 | 5 | 11 | 1 | 2 | 3 | 0 | 5 | 11 | 2 | 10 | -0.225635 | -0.221966 |
| 0 | 4 | 7 | 0 | 5 | 11 | 2 | 0 | 1 | 0 | 5 | 11 | 2 | 10 | 0.125697 | 0.126275 |
| 1 | 2 | 5 | 0 | 5 | 11 | 1 | 2 | 5 | 0 | 5 | 11 | 2 | 10 | -0.121646 | -0.124839 |

Table A.3: *Two-Body Matrix Elements (TBME) given in MeV. See text for details*

| $n_a$ | $\ell_a$ | $j_a$ | $n_b$ | $\ell_b$ | $j_b$ | $n_c$ | $\ell_c$ | $j_c$ | $n_d$ | $\ell_d$ | $j_d$ | $2T$ | $2J$ | N3lO | CD-Bonn |
|---|---|---|---|---|---|---|---|---|---|---|---|---|---|---|---|
| 1 | 2 | 5 | 0 | 5 | 11 | 1 | 2 | 3 | 0 | 5 | 11 | 2 | 10 | 0.166938 | 0.167883 |
| 1 | 2 | 5 | 0 | 5 | 11 | 2 | 0 | 1 | 0 | 5 | 11 | 2 | 10 | -0.357959 | -0.356202 |
| 1 | 2 | 3 | 0 | 5 | 11 | 1 | 2 | 3 | 0 | 5 | 11 | 2 | 10 | 0.014901 | 0.013873 |
| 1 | 2 | 3 | 0 | 5 | 11 | 2 | 0 | 1 | 0 | 5 | 11 | 2 | 10 | 0.298324 | 0.294660 |
| 2 | 0 | 1 | 0 | 5 | 11 | 2 | 0 | 1 | 0 | 5 | 11 | 2 | 10 | -0.196224 | -0.198450 |
| 0 | 4 | 7 | 0 | 5 | 11 | 0 | 4 | 7 | 0 | 5 | 11 | 2 | 12 | 0.117378 | 0.123891 |
| 0 | 4 | 7 | 0 | 5 | 11 | 1 | 2 | 5 | 0 | 5 | 11 | 2 | 12 | 0.065722 | 0.064216 |
| 0 | 4 | 7 | 0 | 5 | 11 | 1 | 2 | 3 | 0 | 5 | 11 | 2 | 12 | -0.097299 | -0.092825 |
| 0 | 4 | 7 | 0 | 5 | 11 | 2 | 0 | 1 | 0 | 5 | 11 | 2 | 12 | 0.013522 | 0.013378 |
| 1 | 2 | 5 | 0 | 5 | 11 | 1 | 2 | 5 | 0 | 5 | 11 | 2 | 12 | 0.164113 | 0.163946 |
| 1 | 2 | 5 | 0 | 5 | 11 | 1 | 2 | 3 | 0 | 5 | 11 | 2 | 12 | -0.009808 | -0.006785 |
| 1 | 2 | 5 | 0 | 5 | 11 | 2 | 0 | 1 | 0 | 5 | 11 | 2 | 12 | -0.168174 | -0.162448 |
| 1 | 2 | 3 | 0 | 5 | 11 | 1 | 2 | 3 | 0 | 5 | 11 | 2 | 12 | 0.160972 | 0.159622 |
| 1 | 2 | 3 | 0 | 5 | 11 | 2 | 0 | 1 | 0 | 5 | 11 | 2 | 12 | -0.087185 | -0.081944 |
| 2 | 0 | 1 | 0 | 5 | 11 | 2 | 0 | 1 | 0 | 5 | 11 | 2 | 12 | 0.109364 | 0.112287 |
| 0 | 4 | 7 | 0 | 5 | 11 | 0 | 4 | 7 | 0 | 5 | 11 | 2 | 14 | -0.109254 | -0.112465 |
| 0 | 4 | 7 | 0 | 5 | 11 | 1 | 2 | 5 | 0 | 5 | 11 | 2 | 14 | 0.112161 | 0.114372 |
| 0 | 4 | 7 | 0 | 5 | 11 | 1 | 2 | 3 | 0 | 5 | 11 | 2 | 14 | -0.340429 | -0.338570 |
| 1 | 2 | 5 | 0 | 5 | 11 | 1 | 2 | 5 | 0 | 5 | 11 | 2 | 14 | 0.000075 | -0.001066 |
| 1 | 2 | 5 | 0 | 5 | 11 | 1 | 2 | 3 | 0 | 5 | 11 | 2 | 14 | 0.335393 | 0.334817 |
| 1 | 2 | 3 | 0 | 5 | 11 | 1 | 2 | 3 | 0 | 5 | 11 | 2 | 14 | -0.403368 | -0.401296 |
| 0 | 4 | 7 | 0 | 5 | 11 | 0 | 4 | 7 | 0 | 5 | 11 | 2 | 16 | 0.167402 | 0.169920 |
| 0 | 4 | 7 | 0 | 5 | 11 | 1 | 2 | 5 | 0 | 5 | 11 | 2 | 16 | 0.054687 | 0.056191 |
| 1 | 2 | 5 | 0 | 5 | 11 | 1 | 2 | 5 | 0 | 5 | 11 | 2 | 16 | 0.162742 | 0.168935 |
| 0 | 4 | 7 | 0 | 5 | 11 | 0 | 4 | 7 | 0 | 5 | 11 | 2 | 18 | -0.882250 | -0.876815 |

Table A.4: *Two-Body Matrix Elements (TBME) given in MeV. See text for details*

# Bibliography


[1] A. Banu *et al.*, Physical Review C **72** (2005).

[2] N. Ishii, S. Aoki, and T. Hatsuda, Physical Review Letters **99**, 022001 (2007).

[3] S. Weinberg, Physica A **96** (1979).

[4] S. Weinberg, Physics Letters B **251**, 288 (1990).

[5] A. M. Bernstein, Opening remarks at chiral dynamics 2006: Experimental tests of chiral symmetry breaking, arXiv:hep-ph/07074250v1.

[6] D. R. Entem and R. Machleidt, Phys. Rev. C **68**, 041001 (2003).

[7] D. R. Entem and R. Machleidt, Phys. Rev. C **66**, 014002 (2002).

[8] E. Epelbaum, A. Nogga, W. Glöcke, U.-G. Kamada, H. Meissner, and H. Witala, The European Physics Journal A **15**, 543 (2002).

[9] R. Machleidt, The meson theory of nuclear forces and nuclear structure, in *Advances In Nuclear Physics*, volume 19, chap. 2, Plenum Press, New York, 1989.

[10] R. Machleidt, Phys. Rev. C **63**, 024001 (2001).

[11] R. Machleidt and G. Q. Li, Physics Reports , 5 (1994).

[12] A. M. Lane and R. G. Thomas, Rev. Mod. Phys. **30**, 257 (1958).

[13] L. Engvik, M. Hjorth-Jensen, R. Machleidt, H. Muther, and A. Polls, Nuclear Physics A **627** (1997).

[14] M. Horth-Jensen, T. T.S. Kuo, and E. Osnes, Physics Reports **261**, 125 (1995).

[15] P. J. Ellis and E. Osnes, Rev. Mod. Phys. **49**, 777 (1977).

[16] P. J. Brussaard and G. P. W. M., *Shell-Model Applications in Nuclear Spectroscopy* (North-Holland, 1977).

[17] A. deShalit and H. Feshbach, *Theoretical Nuclear Physics*volume I: Nuclear Structure (John Wiley& Sons, inc., 1974).

[18] S. A. Moszkowski and B. L. Scott, Annals of Physics **11**, 65 (1960).

[19] P. Ring and P. Schuck, *The Nuclear Many-Body Problem* (Springer, 1980).

[20] A. Bohr and B. R. Mottelson, *Nuclear Structure Volume I* (W. A. Benjamin, 1969).

[21] M. G. Mayer, Phys. Rev. **75**, 1969 (1949).

[22] O. Haxel, J. H. D. Jensen, and H. E. Suess, Phys. Rev. **75**, 1766 (1949).

[23] K. Alder, A. Bohr, T. Huus, B. Mottelson, and A. Winther, Rev. Mod. Phys. **28**, 432 (1956).

[24] K. Alder and A. Winther, *Electromagnetic Excitation* (North-Holland Publishing Company, 1975).

[25] A. Winther and K. Alder, Nuclear Physics A **319**, 518 (1979).

[26] T. Czosnyka, D. Cline, and C. Wu, *Coulomb Excitation Data Analysis Code; GOSIA*, Nuclear Structure Research Laboratory, University of Rochester, 2007.

[27] M. Lindroos, the CERN ISOLDE team, the ISOLDE Collaboration, and the REX-ISOLDE Collaboration, Nuclear Instruments and Methods in Physics Research B **204**, 730 (2003).

[28] F. Ames, J. Cederkall, T. Sieber, and F. Wenander, *The REX-ISOLDE Facility, Design and Commissioning Report* (CERN, 2005).

[29] F. Wenanader, Nuclear Physics A **701**, 528 (2002).

[30] P. K. Ghosh, *Ion Traps* (Oxford Science Publications, 1990).

[31] G. Savard *et al.*, Physics Letters A **158**, 247 (1991).

[32] O. Kester *et al.*, Nuclear Instruments and Methods in Physics Research B **204**, 20 (2003).

[33] A. N. Ostrowski *et al.*, Nuclear Instruments and Methods in Physics Research A **480**, 448 (2002).

[34] J. V. de Walle, *Coulomb excitation of neutron rich Zn isotopes*, PhD thesis, Instituut voor Kern- en Stralingsfysica, Leuven, Belgium, 2006.

[35] N. Warr, *Miniball Electronics at CERN*, http://www.miniball.york.ac.uk/wiki/DocForElectronics.

[36] XIA, *User's Manual Digital Gamma Finder (DGF)*, X-Ray Instrumentation Associates, 8450 Central Ave, Newark, CA. 94560 USA, 2004.

[37] G. C, *The 6-fold Segmented MINIBALL Module Simulation and Experiment*, PhD thesis, MPI, Heidelberg, Germany, 2000.

[38] O. Niedermaier, *Low-Energy Coulomb Excitation of the Neutron-Rich Mg Isotopes $^{30}Mg$ and $^{32}Mg$*, PhD thesis, Heidelberg, Germany, 2005.

[39] R. Lutter, Med data structure, 2005.

[40] R. Lutter and O. Schaile, Marabou - mbs and root based online/offline utility, http://www.bl.physik.unimuenchen.de/marabou/html.

[41] CAEN, url http://www.caen.it.

[42] ROOT, url http://root.cern.ch.

[43] marabou, url http://www.bl.physik.uni-muenchen.de/marabou/html/.

[44] Lund/lbnl nuclear data base, url http://nucleardata.nuclear.lu.se/nucleardata/toi.

[45] A. Michalowicz, *Kinematics of Nuclear Reactions* (Iliffe Books Ltd., 1967).

[46] SRIM, url http://www.srim.org.

[47] D. Seweryniak *et al.*, Nuclear Physics A **589** (1995).

[48] R. Graetzer, S. M. Cohick, and J. X. Saladin, Phys. Rev. C **12**, 1462 (1975).

[49] Band-ramana internal conversion coefficients, url http://www.nndc.bnl.gov/bricc/.

[50] J. Iwanicki, private communication.

[51] I. Talmi, Nuclear Physics A **172** (1971).

[52] P. Federman and S. Pittel, Phys. Rev. C **20**, 820 (1979).

[53] G. Wenes, P. Van Isacker, M. Waroquier, K. Heyde, and J. Van Maldeghem, Phys. Rev. C **23**, 2291 (1981).

[54] A. Kerek, G. B. Holm, l. E. De Geer, and S. Borg, Physics Letters B **44**, 252 (1973).

[55] P. Doornenbal *et al.*, To be published .

[56] D. Warner, M. A. Bentley, and P. van Isacker, Nature **2** (2006).

[57] M. Lipoglavsek *et al.*, Zeitschrift fur Physik A **356** (1996).

[58] J. Cederkäll *et al.*, Physical Review Letters **98**, 172501 (2007).

[59] C. Vaman *et al.*, Physical Review Letters **99**, 162501 (2007).

[60] A. Ansari and P. Ring, Physical Review C **74**, 054313 (2006).

[61] M. Sandzelius *et al.*, Physical Review Letters **99**, 022501 (2007).

[62] T. Otsuka, T. Suzuki, R. Fujimoto, H. Grawe, and Y. Akaishi, Physical Review Letters **95**, 232502 (2005).

[63] L. Gaudefroy *et al.*, Physical Review Letters **97**, 092501 (2006).

[64] P. Federman and S. Pittel, Physics Letters B **69** (1977).

[65] W. Andrejtscheff, L. K. Kostov, P. Petkov, S. Y. Sy, and C. Stoyanov, Nuclear Physics A **505**, 397 (1989).

[66] H. Grawe *et al.*, Progress in Particle and Nuclear Physics **14**, 281 (1992).

[67] M. Lipoglavsek *et al.*, Physics Letters B **440** (1998).

[68] M. Lipoglavsek, *Rigidity of the Doubly-Magic* $^{100}$*Sn Core*, PhD thesis, Lund University, 1998.

[69] D. Seweryniak *et al.*, Physical Review Letters **99**, 022504 (2007).

[70] N. Sandulescu *et al.*, Phys. Rev. C **55**, 2708 (1997).

[71] A. Holt, T. Engeland, M. Hjorth-Jensen, and E. Osnes, Nuclear Physics A **634**, 41 (1998).

[72] M. Hjorth-Jensen, private communication.

# Paper I

# Sub-Barrier Coulomb Excitation of $^{110}$Sn and Its Implications for the $^{100}$Sn Shell Closure

J. Cederkäll,[1,2] A. Ekström,[2] C. Fahlander,[2] A. M. Hurst,[3] M. Hjorth-Jensen,[4] F. Ames,[5] A. Banu,[6,7] P. A. Butler,[3] T. Davinson,[8] U. Datta Pramanik,[9] J. Eberth,[10] S. Franchoo,[11] G. Georgiev,[1] M. Górska,[6] D. Habs,[12] M. Huyse,[13] O. Ivanov,[13] J. Iwanicki,[14] O. Kester,[6] U. Köster,[1] B. A. Marsh,[15,16] O. Niedermaier,[17] T. Nilsson,[18] P. Reiter,[10] H. Scheit,[17] D. Schwalm,[17] T. Sieber,[17] G. Sletten,[19] I. Stefanescu,[13] J. Van de Walle,[13] P. Van Duppen,[13] N. Warr,[10] D. Weisshaar,[10] and F. Wenander[16]

[1]*PH Department, CERN 1211, Geneva 23, Switzerland*
[2]*Physics Department, University of Lund, Sweden*
[3]*Oliver Lodge Laboratory, University of Liverpool, United Kingdom*
[4]*Physics Department and Center of Mathematics for Applications, University of Oslo, Norway*
[5]*TRIUMF, Vancouver, Canada*
[6]*Gesellschaft für Schwerionenforschung (GSI), Darmstadt, Germany*
[7]*Institute for Nuclear Physics, University of Mainz, Germany*
[8]*Department of Physics and Astronomy, University of Edingburgh, United Kingdom*
[9]*Saha Institute of Nuclear Physics, Kolkata 700064, India*
[10]*Institute of Nuclear Physics, University of Cologne, Germany*
[11]*IPN Orsay, Orsay, France*
[12]*Physics Department, Ludwig-Maximilian University, Munich, Germany*
[13]*Instituut voor Kern- en Stralingsfysica, K.U. Leuven, Belgium*
[14]*Heavy Ion Laboratory, Warsaw University, Poland*
[15]*Department of Physics, University of Manchester, United Kingdom*
[16]*AB Department, CERN 1211, Geneva 23, Switzerland*
[17]*Max-Planck Institute of Nuclear Physics, Heidelberg, Germany*
[18]*Fundamental Physics, Chalmers University of Technology, Gothenburg, Sweden*
[19]*Physics Department, University of Copenhagen, Denmark*

(Received 23 January 2007; published 27 April 2007)

The first excited $2^+$ state of the unstable isotope $^{110}$Sn has been studied in safe Coulomb excitation at 2.82 MeV/$u$ using the MINIBALL array at the REX-ISOLDE post accelerator at CERN. This is the first measurement of the reduced transition probability of this state using this method for a neutron deficient Sn isotope. The strength of the approach lies in the excellent peak-to-background ratio that is achieved. The extracted reduced transition probability, $B(E2: 0^+ \rightarrow 2^+) = 0.220 \pm 0.022 e^2b^2$, strengthens the observation of the evolution of the $B(E2)$ values of neutron deficient Sn isotopes that was observed recently in intermediate-energy Coulomb excitation of $^{108}$Sn. It implies that the trend of these reduced transition probabilities in the even-even Sn isotopes is not symmetric with respect to the midshell mass number $A = 116$ as $^{100}$Sn is approached.

DOI: 10.1103/PhysRevLett.98.172501 PACS numbers: 23.20.Js, 21.60.Cs, 25.70.De, 27.60.+j

Substantial interest has recently arisen in the shell structure of atomic nuclei with only a few nucleons outside the double shell closure at $^{100}$Sn. As an example, a series of experiments aiming at isotopes in this region has been carried out using fusion-evaporation reactions in the recent past [1]. With the advent of radioactive ion beams these studies are now taken further using sub-barrier and intermediate-energy Coulomb excitation [2,3]. In this Letter we present the only sub-barrier or ''safe'' Coulomb excitation experiment in this region to date. The study of the reduced transition probability—the $B(E2)$—of the first excited $2^+$ state in an even-even nucleus gives a direct handle on the collectivity of that state. It can thus be used to measure systematic changes in the strengths of shell gaps. The general motivation for this kind of study goes back to our incomplete knowledge of the mechanisms that govern shell formation and their implications for the structure of nuclei far from stability. It is well known that a strong spin-orbit force was introduced into the nuclear shell-model on Fermi's suggestion by Goeppert Mayer [4] and independently by Haxel, Jensen, and Suess [4] to explain the observed shell gaps. However, these papers were substantially predated by the consideration of a nuclear spin-orbit force by Inglis [5] who noted that the relativistic Thomas term which arises as a consequence of the noncommutation of Lorentz transformations should act also in atomic nuclei. This term, given by the vector product of the velocity and acceleration of the bound nucleon, gives rise to nuclear $LS$ coupling, a result which can be derived from the Dirac equation [6]. In this picture, the acceleration is proportional to the derivative of the potential experienced by the bound particle, a notion still used in mean-field approaches today. As a consequence, the splitting of the shell gaps becomes density dependent and may change with the

 

distribution of nucleons in the nucleus. Thus, already on a more fundamental level, changes in shell-gap structure could occur for exotic neutron-proton combinations. It should be added that the size of the Thomas term appeared too small to account for the splitting suggested by Goeppert Mayer and in a later paper Inglis conjectured an addition to spin-orbit partner splitting from meson exchange [7]. In a microscopic description of residual forces in the shell model, other considerations also become important. In particular, close to a self-conjugate shell closure correlations will arise between neutrons and protons that occupy orbits with the same quantum numbers. An example of this is so-called neutron-proton pairing [8]. Furthermore, as has been discussed by Otsuka *et al.* [9] one expects a particularly strong interaction between neutrons and protons occupying spin-orbit partner orbits. In this context, the so-called monopole drift of single-particle energies with respect to mass number becomes important [10]. A main motivation for a study of shell evolution is thus to see if the shell closures that are strong at stability remain so far from stability as the distribution of nucleons changes. This question is particularly interesting in the self-conjugate case. Coulomb excitation of radioactive beams at safe energies is a new and unique tool to address this topic.

The radioactive $^{110}$Sn beam used in the experiment was produced by bombarding a 27 g/cm$^2$ $LaC_x$ target at ISOLDE, CERN, with a 1.4 GeV proton beam from the PS booster. The Sn atoms, after having diffused through the heated target material and effused into an ionization cavity, were ionized by a three-step laser ionization scheme whereafter the beam was extracted and separated in the general purpose separator of the facility. This method provides a high degree of mass and element selectivity. Samples were collected with the laser beams switched on and off to identify the components of the beam. Collection of $^{110}$Sn is possible as its half-life is 4.1 h. The $\gamma$ rays emitted following $\beta$ decay in the sample were measured offline using $\gamma$-spectroscopic methods. It was concluded that Sn ions were implanted only when the laser beams were switched on. Furthermore, surface ionized $^{110}$In was identified as the main beam contaminant. A yield of $2.5 \times 10^8$ atoms/$\mu$C of $^{110}$Sn was established from this measurement. The yield of ionized contaminant $^{110}$In was 1 order of magnitude smaller. The intensity of the post-accelerated beam was set to $\sim 10^6$ p/s on the secondary target. Because of the high production yield the beam current could be measured using pico-am meters with the lasers switched on and off, respectively. This was done at ten different occasions during the experiment in order to determine possible variations in beam composition. The measurements rendered a beam purity, consistent with the offline measurements, of $90.0 \pm 1.4\%$. Decay $\gamma$ rays as well as Coulomb excitation $\gamma$ rays from other contaminants than $^{110}$In were searched for in the final data set but were not observed. As has been discussed previously [11] the REX-ISOLDE post accelerator relies on charge breeding in an electron beam ion source (EBIS) as a first step. The charge breeder and the preceding beam cooling, accomplished by catching the ion bunch from the separator in a gas-filled Penning trap, set the repetition frequency of the beam. In this case the beam was charge bred to the $27^+$ charge state over an EBIS confinement time of 98 ms. The extracted beam pulse had a duration of approximately 100 $\mu$s with a decaying exponential time profile. The beam was accelerated to 2.82 MeV/$u$ in the REX-ISOLDE linac before hitting a 2 mg/cm$^2$ and 99.9% pure $^{58}$Ni target. Because of the characteristic inverse kinematics of the experiment, beam and target particles emerge in a significantly forward-focused cone after scattering.

Coulomb excitation experiments at REX-ISOLDE use a setup that measures the energies and angles of emitted $\gamma$ rays and scattered charged particles. The secondary target position is surrounded by a set of Ge detectors, in a close geometry, called the MINIBALL array [12]. The Ge detectors run independently using sampling ADCs with a common clock. The setup comprises 24 high-purity Ge crystals with a total of 144 segments. The typical photopeak efficiency is $\sim$10% at 1.3 MeV. A circular double sided silicon strip detector (DSSSD) is located 30.6 mm downstream of the target. It registers the energy and angle of a scattered beam and/or target particle (see Fig. 1). To remedy possible dead-time effects the trigger for the particle detector included a raw particle trigger downscaled a factor of $2^6$, and a $\gamma$ ray and charged particle coincidence trigger. The DSSSD comprises 16 annular (front face) and 24 radial (back face) strips. It is subdivided into four separate quadrants. The combined segmentation of the Ge detectors and the DSSSD makes it possible to reconstruct the kinematics of individual Coulomb excitation events for Doppler correction. At 2.82 MeV/$u$ the incoming beam travels at $\beta \sim 8\%$ which results in a complete broadening of the raw $\gamma$-ray spectrum. The effect can be seen in Fig. 2.

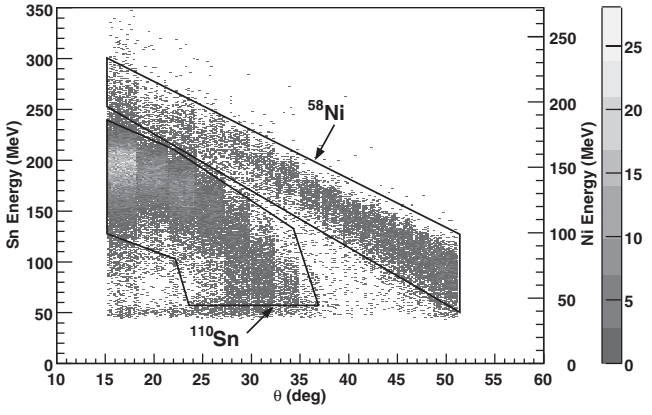


FIG. 1. Scattered beam and target particles as detected in the DSSSD. The upper branch corresponds to scattered $^{58}$Ni and the lower branch to $^{110}$Sn particles, respectively. The kinematical cuts used for the identification of beam and target particles are also indicated in the figure.

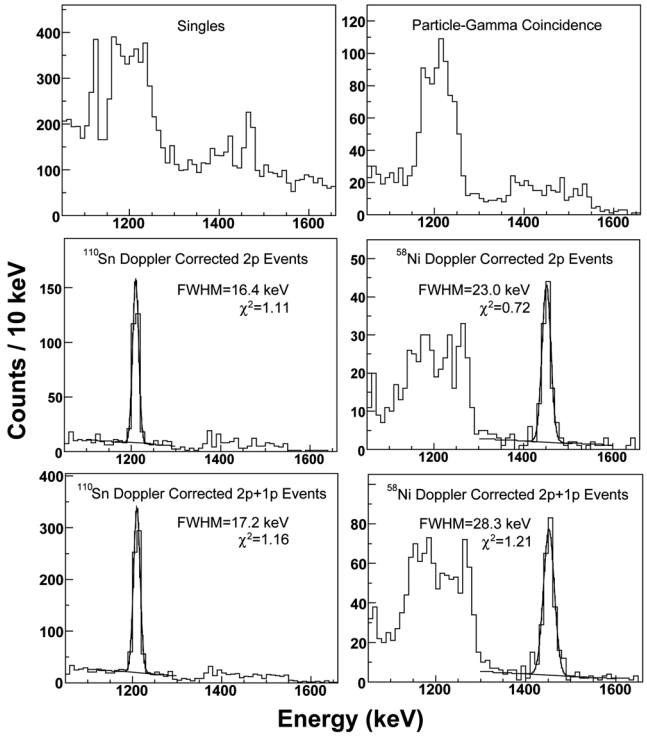


FIG. 2. Single and particle-$\gamma$ coincindence $\gamma$-ray spectra before Doppler correction (top panels). Doppler-corrected $\gamma$-ray spectra for 2-particle $\gamma$-ray coincident events (central panel) and the corresponding Doppler-corrected $\gamma$-ray spectra for the sum of 2-particle and 1-particle reconstructed events for $^{110}$Sn and $^{58}$Ni (bottom panel). See text for detailed discussion.

In this experiment we selected the beam and target such that the kinematical difference in angle and energy of the two can be used for particle identification (Fig. 1). The scattered beam reaches its maximum scattering angle at $\sim$31.8° and scattered target particles at $\sim$84.1°. All angles in this experiment correspond to safe collisions; i.e., there is no internuclear overlap. One can also note that the multiple-step excitation probability, or the probability to excite any other state than the first $2^+$, is negligible with this choice of kinematics. Two features of Fig. 1 can be commented on. First, the energy used for Doppler correction was calibrated using energy loss simulations and the known maximum scattering angle for $^{110}$Sn. The main effect of this improved calibration is to reduce the half-width of the Doppler-corrected $\gamma$-ray peaks. Second, the broadening of the Sn and Ni branches in Fig. 1 is almost entirely caused by differences in emission angle due to the finite size of the beam spot. The two-body kinematics of the experiment was such that every Ni ion scattered within the angular range of the DSSSD is coincident with a beam particle scattered between 24° and 31.8°. Thus a substantial part of the data set contains 2-particle + $\gamma$-ray ($2p + \gamma$) coincidences. This is advantageous as it gives a direct correlation between the number of scattered $^{110}$Sn ions, $^{58}$Ni ions, and emitted $\gamma$ rays. It also provides for Doppler correction for both particles using the energy detected in the DSSSD. The Doppler-corrected spectra for these events are shown in the central panel of Fig. 2. A subset of events contains only 1-particle + $\gamma$-coincidences ($1p + \gamma$). These correspond either to the range for scattered beam below 24° or to events where only one hit could be uniquely reconstructed from the DSSSD. This is, e.g., due to noise or double hits. Note that in a true $2p$ event the particles come back to back in the c.m. system and are thus detected in opposite quadrants in the DSSSD and cannot cause double hits. Furthermore, two-body kinematics can be completely reconstructed by detecting one of the particles. As seen in Fig. 2 reconstruction leads to a slightly larger half-width. The intensities obtained in this fashion were used to extract the $B(E2)$ for the first $2^+$ state in $^{110}$Sn. The method relies on the fact that the $B(E2)$ for the first $2^+$ state in $^{58}$Ni is known. The cross section for exciting target and beam particles is proportional to the corresponding $B(E2)$. The angular distribution of the cross section was calculated for the relevant angular ranges using the code CLX [13]. Taking into account the beam purity, a small angular correction and the $\gamma$-ray detection efficiency, the $B(E2)$ for the first $2^+$ state in $^{110}$Sn was determined to be $B(E2) = 0.220 \pm 0.022 e^2b^2$ (see Table I). The method and the proof-of-principle have been described in Refs. [14,15]. The new result (see Fig. 3) corroborates the published result from intermediate-energy Coulomb excitation of $^{108}$Sn [2]. The two results imply that the first $2^+$ states in the even-even neutron deficient Sn isotopes retain a relatively large part of collectivity compared to the neutron rich isotopes. These states have a constant energy of $\sim$1200 keV which has been explained from the seniority scheme. We note that a recent safe Coulomb excitation measurement for $^{114}$Sn at GSI has reduced the error bar of the $B(E2)$ for that $2^+$ state to same range as for $^{116}$Sn but that a shift towards a higher $B(E2)$ remains [16]. In the following, we compare the measured $B(E2)$ value in $^{110}$Sn to the results of two large-scale shell-model calculations (see Ref. [2]). As a starting point, note that the $1d_{5/2}$ and $0g_{7/2}$ orbits are neutron valence orbits from $^{114}$Sn towards $^{100}$Sn. The main proton valence orbit is $0g_{9/2}$. The calculations, carried out by the Oslo and Strasbourg groups, used effective interactions defined for two different cores, namely $^{100}$Sn and $^{90}$Zr, but using the same nucleon-nucleon interaction. Details on how to derive the effective

TABLE I. The second and third rows give the intensities for the Doppler-corrected Coulomb excitation peaks of $^{58}$Ni and $^{110}$Sn from the sum of hits per bin with corresponding background subtraction and from fitting a Gaussian with linear background. The last row gives the $B(E2; 0+ \rightarrow 2+)$ in $e^2b^2$ for $^{110}$Sn using these numbers, respectively.

| | Energy (keV) | Bin area | Fitted area |
|---|---|---|---|
| $^{58}$Ni | 1454.4 | 237 ± 15 | 222 ± 15 |
| $^{110}$Sn | 1211.9 | 579 ± 24 | 588 ± 24 |
| $B(E2)e^2b^2$ | | 0.220 ± 0.022 | 0.238 ± 0.024 |

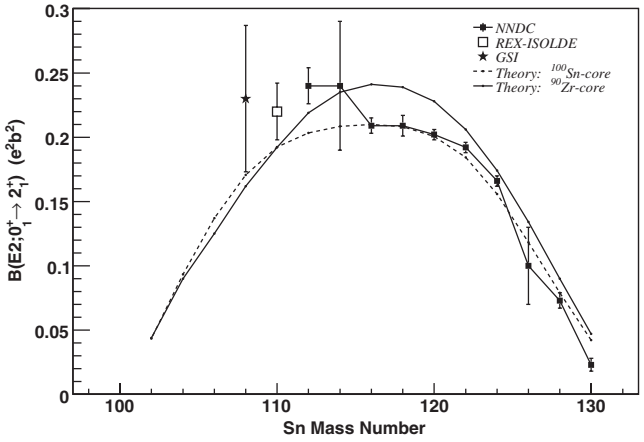


FIG. 3. Current status of measured $B(E2)$ values for the first $2^+$ state in even-even Sn isotopes. Note the shift in $B(E2)$ in $^{114}$Sn as the $g_{7/2}$ and $d_{5/2}$ orbits start to dominate the configuration. The $\chi^2$, taken per degree of freedom, for the deviation between the experimental values and the theoretical predications for the mass number sequences $A_1 = \{114, 112, 110, 108\}$, $A_2 = \{114, 112, 108\}$, and $A_3 = \{114, 112, 110\}$ is $\chi_1^2 = 1.6$, $\chi_2^2 = 1.7$, and $\chi_3^2 = 1.9$ for the $^{90}$Zr core. The corresponding values for the $^{100}$Sn core is $\chi_1^2 = 3.3$, $\chi_2^2 = 4.2$, and $\chi_3^2 = 4.4$, respectively. Consequently, due to the rather small error the current measurement is statistically a more significant test of the deviation from theory than the previous measurement of $^{108}$Sn.

interactions are given in [17]. The $^{90}$Zr case includes protons in the $1d_{5/2}$, $0g_{7/2}$, $0g_{9/2}$, $1d_{3/2}$, and $2s_{1/2}$ and neutrons in the $1d_{5/2}$, $0g_{7/2}$, $1d_{3/2}$, $2s_{1/2}$, and $0h_{11/2}$ single-particle orbits. For a $^{100}$Sn core, neutrons confined to the $1d_{5/2}$, $0g_{7/2}$, $1d_{3/2}$, $2s_{1/2}$, and $0h_{11/2}$ single-particle orbits define the shell-model space. In the calculation of the $B(E2)$ systematics, an effective neutron charge of $0.5e$ and proton charge $1.5e$ were used for the $^{90}$Zr core while an effective neutron charge of $1.0e$ was used for the $^{100}$Sn case. The results are displayed in Fig. 3. In the case of a $^{100}$Sn core, the experimental $B(E2)$ values are reproduced for all isotopes down to $^{116}$Sn. Starting with $^{114}$Sn, the theoretical results display the expected parabolic behavior but are at askance with the experimental result for $^{110}$Sn and the result for $^{108}$Sn [2]. Similar results have emerged for $^{110,108,106}$Sn [3] from intermediate-energy experiments during the preparation of this Letter. To reproduce the experimental values one needs a larger effective charge. Furthermore, the experimental values seem to deviate from a good seniority picture for the lighter Sn isotopes. The transition rates are almost independent of the mass number $A$. Thus the effective charges for the lighter Sn isotopes show stronger renormalization effects. This implies larger core polarization due to particle-hole excitations and a different character of core excitations in the $N = Z$ and $N \gg Z$ regions of the Sn isotopic chain. To further investigate the variation and intrinsic $ph$ structure of the polarization charge in the pure neutron space, Ref. [2] included a calculation with $^{90}$Zr as core with up to four-particle-four-hole proton excitations (current computational limit). In this way, one can reproduce the same trend as for the $^{100}$Sn core but with an effective charge for neutrons of $0.5e$ and protons of $1.5e$. These nonrenormalized charges are discussed by, e.g., Bohr and Mottelson [18]. However, still the enlarged calculations deviate from the new experimental data for lighter Sn isotopes. We note that the current result indicates that further core-polarization effects may be needed and/or a better effective interaction introduced. Here the proton-neutron interaction plays an essential role. In particular, the $\pi(0g_{9/2}) - \nu(0g_{7/2}1d_{5/2}1d_{3/2}2s_{1/2})$ monopoles, responsible for the evolution of the spectroscopy between $^{91}$Zr and $^{101}$Sn, govern the evolution of the proton $Z = 50$ gap with the neutron filling. These monopoles were fitted to reproduce the experimental spectra of nuclei around $A \sim 100$. Here the $\pi(0g_{9/2}) - \nu(1h_{11/2})$ monopole, in particular, suffer from experimental uncertainties. In conclusion, we note the present experimental result, using safe energy Coulomb excitation deviates from current theoretical descriptions of the $Z = 50$ shell gap. Further experiments investigating the reduced transition probability of the corresponding states in lighter even-even Sn isotopes are clearly of importance to further illuminate this question.

This work was supported by the European Union through RII3-EURONS (Contract No. 506065).

[1] M. Gorska *et al.*, Phys. Rev. Lett. **79**, 2415 (1997); M. Lipoglavsek *et al.* Phys. Lett. B **440**, 246 (1998).
[2] A. Banu *et al.*, Phys. Rev. C **72**, 061305(R) (2005).
[3] C. Vaman *et al.*, nucl-ex/0612011.
[4] M. Goeppert Mayer, Phys. Rev. **75**, 1969 (1949); O. Haxel, J. H. D. Jensen, and H. E. Suess, Phys. Rev. **75**, 1766 (1949).
[5] D. R. Inglis, Phys. Rev. **50**, 783 (1936); S. Dancoff and D. R. Inglis, Phys. Rev. **50**, 784 (1936).
[6] W. H. Furry, Phys. Rev. **50**, 784 (1936).
[7] D. R. Inglis, Phys. Rev. **75**, 1767 (1949).
[8] A. L. Goodman, Adv. Nucl. Phys. **11**, 263 (1979).
[9] T. Otsuka *et al.*, Phys. Rev. Lett. **87**, 082502 (2001).
[10] P. Federman and S. Pittel, Phys. Rev. C**20**, 820 (1979).
[11] D. Habs *et al.*, Nucl. Instrum. Methods Phys. Res., Sect. B **139**, 128 (1998).
[12] P. Reiter *et al.*, Nucl. Phys. **A701**, 209 (2002).
[13] H. Ower, computer program CLX.
[14] O. Niedermaier *et al.*, Phys. Rev. Lett. **94**, 172501 (2005), and references therein.
[15] A. M. Hurst *et al.*, Phys. Rev. Lett. **98**, 072501 (2007).
[16] P. Doornenbal *et al.* (to be published).
[17] M. Hjorth-Jensen, T. T. S. Kuo, and E. Osnes, Phys. Rep. **261**, 125 (1995).
[18] Aa. Bohr and B. Mottelson, *Nuclear Structure* (Benjamin, New York, 1969), Vol. 1.

# Paper II

# Sub-Barrier Coulomb Excitation of $^{106,108,110}$Sn

A. Ekström[*], J. Cederkäll[†,*], C. Fahlander[*], M. Hjorth-Jensen[**], F. Ames[‡], P. A. Butler[§], T. Davinson[¶], J .Eberth[‖], G. Georgiev[†], A. Gorgen[††], M. Górska[‡‡], D. Habs[§§], M. Huyse[¶¶], O. Ivanov[¶¶], J. Iwanicki[***], O. Kester[‡‡], U. Köster[†], B. A. Marsh[†††,‡‡‡], P. Reiter[‖], H. Scheit[§§§], D. Schwalm[§§§], S. Siem[¶¶¶], I. Stefanescu[¶¶], G. M. Tveten[¶¶¶], J. Van de Walle[¶¶], P. Van Duppen[¶¶], D. Voulot[‡‡‡], N. Warr[‖], D. Weisshaar[‖], F. Wenander[‡‡‡] and M. Zielinska[***]

[*]*Physics Department, University of Lund, Box 118, SE-221 00 Lund, Sweden*
[†]*PH Department, CERN 1211, Geneva 23, Switzerland*
[**]*Physics Department and Center of Mathematics for Applications, University of Oslo, Norway*
[‡]*TRIUMF, Vancouver, Canada*
[§]*Oliver Lodge Laboratory, University of Liverpool, United Kingdom*
[¶]*Department of Physics and Astronomy, University of Edingburg, United Kingdom*
[‖]*Institute of Nuclear Physics, University of Cologne, Germany*
[††]*CEA Saclay, DAPNIA/SPhN, gif-sur-Yvette, France*
[‡‡]*Gesellschaft für Schwerionenforschung, Darmstadt, Germany*
[§§]*Physics Department, Ludwig-Maximilian University, Munich, Germany*
[¶¶]*Instituut voor Kern- en Stralingsfysica, K.U. Leuven, Belgium*
[***]*Heavy Ion Laboratory, Warsaw University, Poland*
[†††]*Department of Physics, University of Manchester, United Kingdom*
[‡‡‡]*AB Department, CERN 1211, Geneva 23, Switzerland*
[§§§]*Max-Planck Institute of Nuclear Physics, Heidelberg, Germany*
[¶¶¶]*Department of Physics, University of Oslo, Norway*

**Abstract.** The reduced transition probabilities between the first excited $2^+$ state and the $0^+$ ground state, $B(E2;0^+ \rightarrow 2^+)$, have been measured in $^{106,108,110}$Sn using sub-barrier Coulomb excitation in inverse kinematics at REX-ISOLDE. The results are, $B(E2;0^+ \rightarrow 2^+) = 0.220(22)$, 0.226(17), and 0.228(32) $e^2b^2$, for $^{110}$Sn, $^{108}$Sn, and $^{106}$Sn, respectively. The results for $^{106,108}$Sn are preliminary. De-excitation $\gamma$-rays were detected by the MINIBALL Ge-array. The $B(E2)$ reveals detailed information about the nuclear wave function. A shell model prediction based on an effective CD-Bonn interaction in the $\nu(0g_{7/2}, 2s, 1d, 0h_{11/2})$ model space using $e^{\nu}_{eff}$ =1.0 e follows the experimental values for the neutron rich Sn isotopes, but fails to reproduce the results presented here.

**Keywords:** multipole matrix elements, shell model, Coulomb excitation, nuclei with mass number 90 to 149
**PACS:** 23.20.Js, 21.60.Cs, 25.70.De, 27.60.+j

## INTRODUCTION

The experimental knowledge about the shell structure evolution towards the doubly-magic self-conjugate $^{100}$Sn nucleus is now becoming available through radioactive ion beam (RIB) techniques. The investigation of exotic isotopes can reveal novel effects of the underlying effective nucleon-nucleon interaction. Furthermore, the Sn isotopes span a region between the $N = Z = 50$ and $N = 82, Z = 50$ shell closures making it the

longest isotopic chain available for experiment. This enables a unique study of the shell structure variations as a function of the number of neutrons outside the closed $^{100}$Sn core. The constancy of the energy separation between the first excited $2^+$ state and the $0^+$ ground state in the even-mass Sn isotopes is well explained within the generalized seniority model [1]. Furthermore, according to this theory, non-diagonal matrix elements of the even one-body E2 tensor operator will exhibit a parabolic behaviour as a function of mass number across the Sn isotope chain. Large scale shell-model calculations [2] based on an effective CD-Bonn nucleon-nucleon interaction agree with the generalized seniority model. The adopted experimental $B(E2)$ values on the neutron-rich side of the Sn chain follow the theoretical predictions. The experimental RIB results on $^{106,108,110}$Sn presented here and in [2, 3, 4] are consistent with each other and display a clear discrepancy with theoretical models.

## EXPERIMENTAL TECHNIQUES

Radioactive $^{110}$Sn, $^{108}$Sn, and $^{106}$Sn beams were produced at ISOLDE by bombarding a thick Lanthanum Carbide primary target by 1 GeV protons. Atomic Sn was ionized through a resonant three-step laser scheme and the isotope of interest was separated using the General Purpose Separator of the facility. The selected isotope was subsequently cooled in a Penning-type trap after which the beam was charge bred in the Electron Beam Ion Source. Post-acceleration was performed by the REX linac. The final beam energy was 2.8 MeV/u, well below the Coulomb barrier in order to exclude any excitation caused by direct nuclear-nuclear overlap. The first $2^+$ state was populated through sub-barrier Coulomb excitation against a 2 mg/cm$^2$ thick $^{58}$Ni target. De-excitation $\gamma$ rays were detected by the highly segmented MINIBALL Ge-array. The recoils and ejectiles were detected by a Double Sided Silicon Strip (DSSSD) detector placed 3 cm from the $^{58}$Ni target covering an angular range of about 16°-54°. High segmentation in both $\gamma$-ray and particle detectors allowed for a Doppler correction. This is needed since scattered particled had velocities of $\sim 0.05c$. A side effect of using RIBs is the significant $\gamma$-ray background caused by unstable nuclei deposited in the target chamber. By gating on prompt particle-$\gamma$ coincidences the background was reduced. A further gate in the analysis was to select only those events in which both the ejectile and the recoil was detected in the DSSSD, a so called 2p event. Due to the type of inverse kinematics this implied selecting events where both the ejectile and the recoil was scattered with an angle larger than 24°. In the case when only one particle, a so called 1p event, was detected over 24°, due to e.g. noise or double hits, the missing particle could be reconstructed. The integrated Coulomb excitation peaks presented in this paper come from the total set of $1p+2p$ events. The $\gamma$-ray statistics was increased by $\sim$10% due to add-back between neighbouring Ge-crystals. It should also be mentioned that the beam did not consist of only the selected Sn isotope, but also of surface ionized In. The contamination originate in the cavity immediately after the primary target. It is of primary importance to map out the isobaric contamination over time. In the case of $^{110}$Sn, the beam contamination was not that severe. Due to the high beam intensity of $\sim 10^6$ p/s at the secondary target, the In component could be measured by switching off the laser and register the beam current just before the $^{58}$Ni target. The contamination gradually increase as the proton drip line

**TABLE 1.** Experimental $B(E2)$ values from this work. Note that the values on $^{108,106}$Sn are preliminary. The value on $^{110}$Sn has previously been published in [3]

| Isotope | $^{110}$Sn | $^{108}$Sn | $^{106}$Sn |
|---|---|---|---|
| $B(E2;\uparrow)$ [e$^2$b$^2$] | 0.220(22) | 0.226(17) | 0.228(32) |

is approached. In the $^{106,108}$Sn experiments the laser power was recorded continously in the data stream as well as the laser status. The laser was run in on/off mode for one hour every three hours throughout the experiments. In summary, this yielded Sn fractions of 90.0(14)%, 58(1)%, and 25(1)% for $^{110}$Sn, $^{108}$Sn, and $^{106}$Sn, respectively. It should be pointed out that the intensity of the $^{108}$Sn beam was comparable to the $^{110}$Sn beam, while for $^{106}$Sn it was one order of magnitude lower. This is the primary reason for the larger uncertainty in the $B(E2)$ value for $^{106}$Sn. The transition probabilities were extracted by measuring the $\gamma$-ray yield coming from the $2^+ \rightarrow 0^+$ transition in $^{110,108,106}$Sn and normalizing against the corresponding $\gamma$-ray yield of the equivalent transition in $^{58}$Ni which has a known $B(E2;0^+ \rightarrow 2^+)$ value. Angular integration as well as energy loss in the $^{58}$Ni target was performed by the coupled-channels code GOSIA2.

## RESULTS AND DISCUSSION

The results from this work are presented in Tab. 1 and displayed in Fig. 1. The $B(E2)$

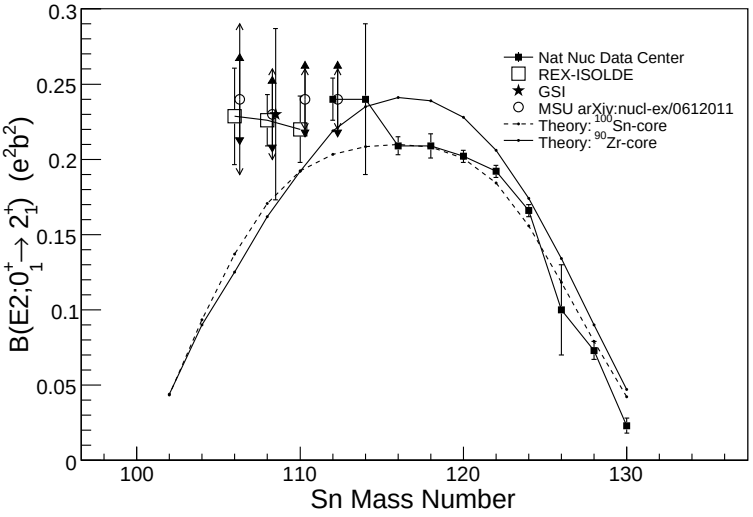


**FIGURE 1.** The known experimental $B(E2\uparrow)$ values expressed in e$^2$b$^2$ across the Sn isotope chain. The results from REX-ISOLDE presented in this paper are marked with empty squares. The value on $^{110}$Sn has been published in [3]. The value on $^{108}$Sn indicated with a star comes from a measurement at GSI [2] using intermediate Coulomb excitation. The empty circles mark the $B(E2)$ values for $^{106,108,110,112}$Sn measured at MSU [4] using intermediate Coulomb excitation. The dotted and solid lines extending over the entire isotope chain indicate the result of shell-model calculations [2] using $^{100}$Sn (dotted) or $^{90}$Zr (solid) as closed shell cores.

values are in disagrement with theoretical predictions based on shell-model calculations using an effective CD-Bonn interaction renormalized with G-matrix theory. The details regarding the calculations presented in Fig. 1 can be found in [2]. It is however worth mentioning that the model space included only $\nu(0g_{7/2}, 2s, 1d, 0h_{11/2})$ with an effective neutron charge $e^{\nu}_{eff} = 1.0$ e. Including proton-neutron excitations from $0g_{9/2}$ was computationally not possible due to the size of the model space. The effect of core-polarization was considered using a seniority truncated model space $\pi(0g1d2s)$ and $\nu(0g_{7/2}1d2s0h_{11/2})$ using $e^{\nu}_{eff} = 0.5$ e and $e^{\pi}_{eff} = 1.5$ e with $^{90}$Zr as a closed core. A Relativistic Quasiparticle Random Phase Approximation done in Ref. [5] is consistent with the results presented in this paper but fails to reproduce the adopted $B(E2)$ values in the mid-shell and neutron-rich region. Inclusion of proton-neutron excitations across the $N = Z = 50$ shell gap will of course increase the collectivity of the $2^+$ state. This is immediately seen in the $^{90}$Zr core calculation in Fig. 1. The observed transition rates reported on here is independent of $A$ indicating that seniority is violated towards $^{100}$Sn and implying stronger renormalization effects on the effective charges. The picture is reversed on the neutron rich side of the isotopic chain, where a good shell closure is reached at $N = 82, Z = 50$ as seen in Fig. 1. Furthermore, this region has been studied experimentally to a greater extent. The number of neutrons in the $(0g_{7/2}1d_{5/2})$ plays an important role for the size of the $\pi(0g_{9/2}) - \nu(0g_{7/2}1d_{5/2})$ energy separation. The same effect is responsible for the shell structure evolution between Zr-Sn as the $\pi(0g_{9/2})$ is filled [6, 7]. We are presently preparing a parallel shell-model calculation in an extended model space which includes proton-neutron excitations from the $0g_{9/2}$ orbit.

## REFERENCES


1. I. Talmi, Nucl. Phys. **A172**,1 (1971).
2. A. Banu *et* al., Phys. Rev. C **72**, 061305(R) (2005).
3. J. Cederkäll *et* al., Phys. Rev. Lett. **98**, 172501 (2007).
4. C. Vaman *et* al., arXiv:nucl-ex/0612011v1. To be published in Phys. Rev. Lett.
5. A. Ansari, Phys. Lett **B623**, 37 (2005).
6. B. L. Cohen, Phys. Rev. **127**, 597 (1962).
7. T. Otsuka *et* al., Phys. Rev. Lett. **95**, 232502 (2005).